DEVELOPMENT OF NOVEL TECHNIQUES FOR PASSIVE RADAR WITH WAVEFORM DESIGN, TRACKING AND SEQUENTIAL FUSION

Thesis

Submitted in partial fulfillment of the requirements for the degree of

DOCTOR OF PHILOSOPHY

by

PURUSHOTTAMA T L

DEPARTMENT OF ELECTRONICS AND COMMUNICATION ENGINEERING

NATIONAL INSTITUTE OF TECHNOLOGY KARNATAKA,

SURATHKAL, MANGALORE - 575025

APRIL 2023

DECLARATION

by the Ph.D. Research Scholar

I hereby declare that the Research Thesis entitled **DEVELOPMENT OF NOVEL TECHNIQUES FOR PASSIVE RADAR WITH WAVEFORM DESIGN, TRACKING AND SEQUENTIAL FUSION** which is being submitted to the **National Institute of Technology Karnataka, Surathkal** in partial fulfilment of the requirements for the award of the Degree of **Doctor of Philosophy** in **Electronics and Communication Engineering** is a *bonafide report of the research work carried out by me*. The material contained in this Research Thesis has not been submitted to any University or Institution for the award of any degree.

(187084/187EC011, PURUSHOTTAMA T L)

Department of Electronics and Communication Engineering
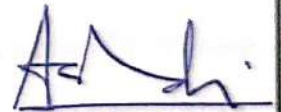
Place: NITK, Surathkal.

Date: 03/04/2023

CERTIFICATE

This is to *certify* that the Research Thesis entitled **DEVELOPMENT OF NOVEL TECHNIQUES FOR PASSIVE RADAR WITH WAVEFORM DESIGN, TRACKING AND SEQUENTIAL FUSION** submitted by **Mr. PURUSHOTTAMA T L**, (Register Number: 187084/187EC011) as the record of the research work carried out by him, is *accepted as the Research Thesis submission* in partial fulfilment of the requirements for the award of degree of **Doctor of Philosophy**.

Dr. Pathipati Srihari

Research Guide

4-4-2023

Prof. Ashvini Chaturvedi

Chairman - DRPC

Acknowledgment

Place: Surathkal   Purushottama T L
Date: 03/04/2023

To all my Favourite Teachers:

Sri. Bhadraiah (My primary School teacher)

Sri. A Suresh (My high school English teacher)

Sri. H S Mahadevaiah (My Pre-University Mathematics teacher)

Dr. H M Chandrashekar (My Engineering Circuit Analysis teacher)

Dr. N Srinivasa Rao (My M.Tech VLSI design teacher)

Sri. Karthik Rajagopal (My mentor at Honeywell Technologies)

Dr. Pathipati Srihari (My Ph.D research supervisor)

Abstract

In modern warfare, electronic countermeasure (ECM) approaches have gained much importance as electronic technology and military intelligence has improved significantly. The common forms of ECM are noise jamming and deception jamming. Noise jamming is an ECM technique, in which the target radar sends a stronger noise signal at the operational frequency of the radar, blending the target's signature entirely with the interference. Deception jamming techniques, on the other hand, such as range gate pull-off (RGPO) and velocity gate pull-off (VGPO), are the most effective of all ECM techniques for creating false targets to misguide the target tracking systems. RGPO ECM intercepts the radar signals and retransmits a deception signal with a progressive time delay, pulling the range gate of the radar target tracker further away from the actual target over time. The main focus of this research work is to combat the range deception ECM using the effective electronic counter countermeasure (ECCM) technique. Further, the research is focused on passive radars, which have the advantage of covertness and cost-effectiveness and are useful in military and civilian applications. Furthermore, the secondary objective of this research work is to comprehensively analyze the performance of existing illuminators of opportunity (IOO) and propose a good IOO for passive radars.

Primarily, the first objective proposes a sequential fusion-based approach for detecting the range deception ECM and estimating the RGPO deception parameter of the deceived local track in a networked radar system (NRS). In NRS, each radar has a local tracker that provides local estimates (updated state and covariance), which are subsequently forwarded to the fusion node. Following that, a track-to-track association (T2TA) at the fusion node is formed to detect the deceived tracks utilizing all accessible local tracks. For the deceived track, the pseudo-measurements are created using the inverse Kalman filter-based tracklets. Further, the reference measurements are created by sequentially fusing all the undeceived local tracks. Next, the recursive least squares estimator (RLSE) is used to estimate the range deception parameter of the deceived track using the pseudo-measurements and the reference measurements. Furthermore, the proposed deception parameter estimation algorithm is also analyzed

for single and multiple RGPO ECM scenarios. Moreover, the Cramer Rao Lower Bound (CRLB) is derived for the proposed estimation algorithm. Also, Position Root Mean Square Error (PRMSE), CRLB, innovation test, normalized estimation error squared (NEES) test, and confidence interval are used to quantify the results. The simulation results highlight that the proposed estimation algorithm provides improved performance in the presence of RGPO ECM. Besides, it is evident from the results that estimator efficiency is falling below the 5% tail probability of the chi-square distribution.

Another contribution of the thesis is to carry out the feasibility study of the 5G New Radio (5G NR) waveform as an IOO for passive radar. The investigation results show the possibility of utilizing the 5G NR waveform as a suitable IOO for target detection in passive radar applications. For the 5G NR waveform, parameters like range resolution and velocity resolution are determined, and a comparison is made with the LTE waveform. The simulation results reveal that the 5G NR waveform provides better range resolution and velocity resolution than the LTE and other IOOs. Further, Significant recent radar research has been focused on knowledge-aided signal processing, waveform design, detection, and target-tracking applications. The knowledge related to the illuminator of opportunity (IOO) selection, spectrum sensing, and diversity technique can predominantly improve the received signal strength (RSS) at the passive radar receiver. In addition, this work proposes a conceptual framework to build knowledge-aided passive radar systems (KA-PRS) based on spectrum sensing, IOO selection, and spatial diversity.

Finally, this research investigation proposes a comprehensive analysis of losses incurred by the IOOs during their propagation in the surveillance environment. The different IOOs considered in this investigation are Frequency Modulated (FM) waveform, Digital Video Broadcasting (DVB) waveform, Long Term Evolution (LTE) Waveform, and 5G NR waveform, etc. The atmospheric losses (such as path loss, rain loss, gas loss, fog loss, and foliage loss) are analyzed for various IOOs. Further, signal-to-noise ratio analysis for 5G NR waveform at FR1 and FR2 frequencies is carried out in the presence of atmospheric losses. The simulation results show that the high frequency 5G NR FR2 waveform (26 GHz to 50 GHz) suffers significantly higher losses than other IOOs, even though it provides improved range and velocity resolution. Specif-

ically, the 5G New Radio waveform for FR1 and FR2 frequencies has 10% and 20% more losses than the LTE waveform. On the other hand, the FM waveform suffers insignificant losses compared to other IOOs despite the poor range and velocity resolution. Additionally, the penetration loss for common building materials such as clear glass, plywood, and tile for the 5G NR FR1 frequency, LTE signal frequency, and Wi-Fi is measured using the Texas Instruments AFE7950 radar sensor. Further, the results obtained in this contribution can be a valuable reference for passive bistatic radar as the comprehensive analysis includes all IOOs along with the newly proposed 5G NR waveform.

Overall, this thesis proposes a potential ECCM technique to overcome the effect of range deception ECM in the target tracking framework. Further, the feasibility of utilizing 5G NR for passive radar is carried out along with the comprehensive study of losses for various IOOs.

Contents

List of Figures

List of Tables

Abbreviations and Nomenclature

Abbreviations

2-D	Two-Dimensional
3-D	Three-Dimensional
$5G$	Fifth Generation
S-D	S-Dimensional
CRLB	Cramer-Rao Lower Bound
CT	Coordinated Turn
CV	Constant Velocity
DAB	Digital Audio Broadcasting
DVB	Digital Video Broadcasting
ECCM	electronic counter countermeasure
ECM	electronic countermeasure
EKF	Extended Kalman Filter
EW	Electronic Warfare
FM	Frequency Modulated
FR1	Frequency Range-1
FR2	Frequency Range-2
GNN	Global Nearest Neighbor

GNSS   Global navigation satellite system

GPS   Global Positioning System

GPS   Global System for Mobiles

IMM   Interactive Multiple Model

INS   inertial navigation system

IOO   Illuminator of Opportunity

JSR   Jamming signal ratio

KF   Kalman Filter

LOS   line of sight

LS   least-squares

LTE   Long Term Evolution

MATLAB   MAtrix LABoratory

MC   Monte Carlo

NEES   Normalized estimation error test

NN   Nearest Neighbor

NR   NeW Radio

PDA   probabilistic data association

PRF   pulse repetition frequency

PRMSE   Position Root Mean Square Error

RF   Radio Frequency

RGPO   Range gate pull-off

RSS   received signal strength

SOJ	Stand-Off Jammer
SSJ	Self-Screening Jammer
T2TA	Track-to-track association
VHF	Very high frequency
Wi-Fi	Wireless Fidelity
WiMAX	Worldwide Interoperability for Microwave Access

Nomenclature

r	deception parameter
$\Delta\rho$	Range Resolution
Δf_d	Doppler Resolution
Δv	Velocity Resolution
$\Gamma(\cdot)$	Noise gain matrix
$\Lambda(\cdot)$	Likelihood function
λ_x	Wavelength
$\mathbf{F}$	state transition matrix
$\mathbf{H}$	measurement transition matrix
$\mathbf{P}$	State covariance matrix
$\mathbf{P}_f$	fused covariance
$\mathbf{R}_z$	Measurement noise covariance matrix
$\mathbf{U}$	Pseudo-measurement covariance
$\mathbf{u}$	Pseudo-measurement
$\mathbf{v}$	process noise

$\mathbf{W}$	Kalman gain
$\mathbf{x}_f$	fused state
$\mathbf{y}$	recreated measurement
$\mathbf{z}$	measurement vector
ν_z	Innovation
ϕ_a	Azimuth measurement
σ	Standard deviation
$\mathbf{S}(\cdot)$	Measurement residual covariance
H	Hypothesis
i	Radar index
K	Total number of pseudo-range measurements
k	Discrete time index
m_x	Dimension of the state vector
m_z	Dimension of the measurement vector
P_D	Detection probability of a target
Q_x	Process noise covariance matrix
r	Range measurement
t	Time
v	Velocity

Chapter 1

Introduction

1.1   ECM Background

1.1.1   ECM

Electronic countermeasures inject signals into an enemy's electronic defense system, degrading its functionality. ECM signals include jamming and deception. Jamming is the intentional emission or reflection of electromagnetic energy with the intent of interfering with an enemy's protection system. Deception is the intentional broadcast or re-transmission of electromagnetic energy signals to deceive an enemy system's interpretation or use of information received. While simple noise ECM techniques are still utilized, most current tracking radars require more complex deception approaches to be defeated. As a result, noise ECM should not always be seen as a realistic or preferable alternative for modeling jamming situations in a tracking investigation. ECM strategies are usually adapted to the flaws of the particular radar under attack.

ECM approaches were traditionally built for end-game, one-on-one battles to protect against a dedicated radar. Multi-target (multi-function) electronic scan tracking radars controlled by advanced tracking algorithms are used in modern air defense missile systems. The tracking algorithm designers must understand ECM phenomenology to construct and incorporate ECCMs into the target tracking framework. Much research has been done to design robust algorithms to manage target motions and clutter. The tracking algorithm developers must implement effective ECM-handling algorithms to tackle deception jamming and propose efficient ECCM approaches to neutralize these counter measures.

1.1.2   Noise Jamming

Noise ECM is generated by modulating, filtering, and amplifying an RF noise source in open-loop and transponder ECM systems. The bandwidth of wideband or "barrage" noise is around 100-500 MHz, whereas the bandwidth of narrow band or "spot" noise is approximately 10 MHz. When several victim radars must be jammed at the same time, or when the specific victim radar RF is unknown, barrage noise is utilized. When the RF is precisely known or easily traced, spot noise is utilized to assault a single radar. Narrow band noise is preferable in terms of efficacy since a more significant proportion of the noise energy is directed toward the radar's reception band. Set-on spot noise is when a transponder's analysis receiver finds the victim's radar and instructs the spot noise jammer to "set on" the radar's operational frequency. Further, many contemporary radars use pulse compression waveforms and ultra-low side lobe antennas to mitigate the impacts of noise ECM techniques. As a result, the jammer finds it difficult to inject enough noise energy to damage radar performance.

1.1.3   Range Gate Pull Off (RGPO)

RGPO ECM is a type of countermeasure that attempts to deceive or trick the tracking radar in range. RGPO techniques are different from other range false-target techniques in that they presume the target is first tracked and that the tracker's range gate must be "pulled" off the target return. When the tracker has moved away from the actual target, it is "dropped," causing the radar to reacquire the target. By requiring the radar to reacquire the target periodically, the radar can be stopped from obtaining the track quality required to launch a missile. A transponder or a repeater ECM system can be used to generate the RGPO ECM. The RGPO approach is used by first creating a fake target that coincides with the true target return. To further alter the real range position, the ECM system may utilize a cover pulse (a broad pulse that overlaps the true target). To make the fake target more appealing, the amplitude of the false target might be modified to be greater than that of the true target. The false target is then walked away from the true target in range. A delayed version of each radar pulse is used to generate this walk-off target (the delay corresponds to the range translation).

1.1.4 Electronic Counter Counter Measures (ECCM)

While ECM has been used to destroy radar-guided missile systems for years, radar designers have built counter-ECM measures inside the radar. These counter-measures, known as ECCMs, will "automatically" reduce the jamming signals, potentially limiting the conditions in which the tracking algorithm must work. Tracking algorithm developers should be aware of various ECCM approaches and understand that some ECM strategies will not cause issues due to ECCM characteristics already included on the radar. On the other hand, developers should be aware that some automated ECCM approaches may mistakenly suppress readings that might indicate actual targets.

1.1.5 Networked Radar System (NRS)

Networked radar has been very prominent in recent years for the abundant resources it can use, specifically in target tracking applications. A networked radar system (NRS) connects several heterogeneous radar systems geographically located at different locations to a fusion center to jointly detect and monitor targets in a large surveillance region (Geng 2020). Since an NRS can significantly boost the precision of detection and monitoring targets, it finds various applications, such as air traffic control, military intelligence, autonomous vehicles, etc. Further, radar networks are widely adopted in civilian and military infrastructures, and ECM attacks may pose a significant challenge to national security and the economy (Yang et al. 2018).

1.2 Basic Target Tracking

1.2.1 Estimation and Tracking

The process of inferring the value of a quantity of interest from noisy data or observations is known as an estimation. That is, estimating may be thought of as the process of selecting a point from a continuous space. The quantity of interest may be the state of dynamic systems, which is often a vector including kinematic and feature-related data. Tracking is the assessment of the state of a moving object. Tracking is processing data or observations collected from targets of interest to keep them in their present state. This state typically consists of the followings:

- Position, velocity, acceleration, turn rate, and other kinematic components.

- Radiated signal intensity, radar cross-section, target categorization, and so on are some of feature components.

- Constant or slowly varying parameters such as aerodynamic parameters etc.

Data or measurements are observations about a target's state corrupted by noise. These observations could be: bearing from the radar sensor; range, azimuth, and elevation; time difference of arrival, the direction of arrival, and range rate (Doppler), etc.

1.2.2 Basic terminology

- **Target**: A moving or stationary object (ex. car or airplane).

- **Sensor**: Device that observes the environment by reception of some signals (ex. radar or sonar or lidar).

- **Time stamp**: The time to which a detection pertains.

- **Observation**: refers to acquired measurements at sensor (ex. range, azimuth are measurements of 2D radar sensor).

- **State**: refers to stacked parameters of interest pertaining to target (ex. position, velocity, and acceleration)

- **Gating** The purpose of gating is to exclude the measurements that are highly unlikely to have originated from a particular target.

- **Association** The process of associating measurements to existing tracks or existing tracks to measurements is known as association.

- **Hypothesis** A hypothesis is a partitioning the measurements based on their origin, individual existing targets, false detections, and new targets.

- **Sensor Fusion** Sensor fusion is the process of combining the data from multiple sensors so as to reduce the amount of uncertainty.

- **Bistatic Radar** Radar in which the receiver is physically separated from the transmitter, so that the echo signal does not follow the same path as the transmitted signal.

- **Multi-static Radar** A radar system consisting of multiple spatially separated radars with a common coverage area.

- **Networked Radar System** Radar system connecting several heterogeneous radar systems geographically located at different locations to a fusion center for target detection and tracking.

1.3   Passive Radar Background

1.3.1   Passive Radar Systems

Most modern radars are active, meaning they explicitly transmit radio signals to carry out their sensing objective. In contrast, the passive radars do not transmit radio-frequency signals; instead, they utilize ambient radio-frequency illumination provided by transmitters such as television, radio, cellular telephone towers, and active radars. Further, passive radar offers some advantages over the active radar, particularly in a covert operation, and does not clutter the scarce radio spectrum resources with added transmissions (electromagnetically green) (Millet and Klein 2011). As quoted prior, passive radars utilize the electromagnetic signals transmitted by other sources, referred to as "illuminators of opportunity" (IOO). Examples include signals from other radars, communication systems, and broadcast systems. Further, the principle of operation of passive radar is based on preprocessing the signal received directly (IOO) from a transmitter of Opportunity with its reflections from a target and cross-correlating both the signals. Then, appropriate signal processing and filtering techniques are utilized to detect and track the targets (Kuschel et al. 2019a).

Fig. 1.1 depicts a simple representative diagram of the passive bistatic radar system. From Fig. 1.1, it can be inferred that in most cases, the reflected echo signal from the target will be masked by the direct signal unless Doppler separates it. There is no further attenuation of the direct signal since it travels a shorter distance than the target reflected echo. Thus, for the proper detection of the targets, additional
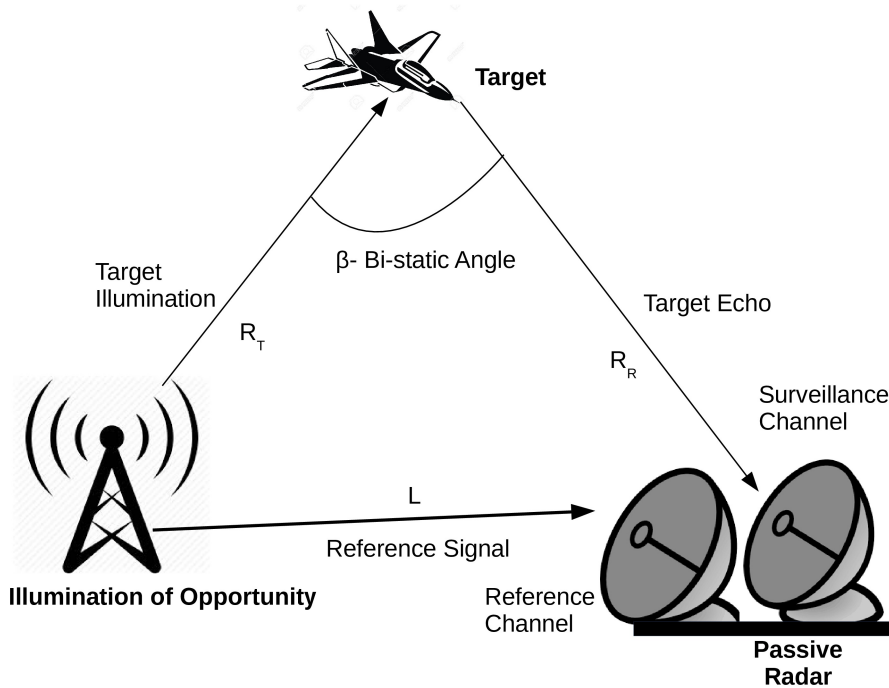
Figure 1.1: Passive radar in its simplest form

processing is necessary at the passive radar for processing direct signals since it may suppress the echo. Generally, two separate channels are required at passive radar site, one dedicated to the collection of the direct signal and referred to as reference channel (e.g., this receiving channel connected to an antenna in line of sight towards the illuminator of opportunity), and other channel which collects target echo signals referred as surveillance channel. Eventually, the surveillance channel can be multi-channel, thus increasing the overall capabilities of the passive radar system (Griffiths and Baker 2017a).

The reference receiver channel usually is a single dedicated channel for receiving the reference signal as clean as possible because the transmitted signal is not known as a priory. It is generally positioned in line-of-sight to the transmitter and requires a highly directional antenna to avoid multipath. This is an essential requirement when analog (broadcast) IOO signals are adopted, which do not offer a reconstruction of the transmitted signal from signal synchronization features. The most important signal processing step at the passive radar is the suppression of the direct signal since its

correlation with side lobes might mask weak target echoes (Kuschel et al. 2019a). Direct signal suppression can be achieved by filtering the received signal spatially or in the time domain. Further, the received signal strength at the passive radar receiver is mainly affected by external factors like noise, interference, atmospheric factors, and other sources. Hence, there is a need to improve the signal quality at the passive radar receiver. Also, the overall target detection and tracking performance are entirely dependent on the availability of the IOO signal and the features of the IOO signal being adopted. Therefore, the comprehensive study of the available IOOs is of prime importance prior to adopting them for specific applications.

1.3.2 Advantages and Disadvantages of passive radars

Advantages

- Passive radars provide broader coverage since most of the broadcast and communication system transmitters are sited in high locations.

- The cost of a passive radar is comparatively lesser than conventional radar, and it does not have licensing issues since it adopts existing transmitters.

- The passive radar receiver is undetectable until the receive antenna is inconspicuous, and it is covert since the receiver does not transmit any signal.

- Countermeasures against passive radar are challenging to implement. Any jamming will have to be distributed in a wide range of directions and frequencies, weakening its impact.

- Passive radar can be considered 'green radar' because it does not require any additional spectrum (Kuschel et al. 2019a).

- A vast range of transmissions can be adopted by passive radar, and almost any transmission can be used as the IOO for passive radar.

Disadvantages

- The IOO waveforms utilized by passive radar are not optimized for radar purposes, so the suitable waveforms are to be selected and processed optimally.

- In most cases, the transmitting source is not under the control of the passive radar.

- At the passive radar receiver, significant signal processing must be used to suppress the direct signal and multi-path to detect weak target echoes.

- The range resolution, velocity resolution, and Doppler resolution are poor if the targets are very close to the line connecting the IOO transmitter and passive receiver.

1.4   Contributions of the Thesis

In this thesis, an effective electronic counter countermeasure technique has been proposed to combat RGPO and further estimate the range deception parameter using an efficient target tracking framework. Further, a comprehensive study of illuminators of opportunity for passive radar has been carried out. The main contributions of the thesis are as follows:

1. Proposed a framework for estimating the deception parameter at the fusion center in a Networked radar system to provide an efficient ECCM to the RGPO ECM technique.

2. Proposed the upcoming 5G New Radio waveform (5G NR) as an IOO for passive bistatic radar, analyzed and compared the radar parameters with the existing IOOs.

3. Presented a conceptual framework of Knowledge Aided Passive Radar System (KA-PRS) to improve the received signal strength at the passive radar receiver.

4. Presented the comprehensive simulation study of external losses affecting the propagation of IOOs utilized by the passive radars.

5. An experimental study of penetration losses has been carried out using real radar system in an indoor environment.

1.5 Overview

The following chapters of the thesis are organized as follows: Chapter 2 presents the literature review of ECCM techniques against RGPO, transmitters of opportunity for passive radar, and the losses incurred by the IOOs during their propagation. Chapter 3 deals with the deception parameter estimation algorithm to counter RGPO ECM in a networked radar scenario. Further, Chapter 4 discusses the feasibility study of a 5G NR signal waveform as an IOO for passive radar. Further, Chapter 4 presents a conceptual framework of KA-PRS to improve the received signal strength in a passive radar receiver. Chapter 5 elaborates on the study of various losses incurred by IOOs' in a passive radar system. Additionally, Chapter 5 presents an experimental study of penetration losses for building materials (such as clear glass, plywood and tile) using Texas Instruments radar system in an indoor environment. Finally, the conclusion and future work are presented in Chapter 6.

Chapter 2

Literature review

2.1 Range Gate Pull-Off ECM

Electronic countermeasures are the key techniques in modern warfare, with recent advances in electronic technology and military intelligence. Many ECM techniques have been presented in the literature, such as noise jamming, Stand-Off Jamming (SOJ), Self Screening Jamming (SSJ), RGPO, and VGPO (Kirubarajan et al. 1998]). In noise jamming, the radar transmits a noise signal with higher strength at the opposition radar's operating frequency so that the target detection is entirely affected by interference. Also, in the SOJ technique, the high-power jamming signal is transmitted from the enemy radar at a more considerable distance than the maximum range at which the targeted radar can detect the targets. Further, in SSJ, jamming equipment is carried out for self-protection, and efficient jamming geometry between victim radar and jammer is always maintained. Deception jamming techniques like RGPO and VGPO are the most effective of all the ECM techniques that generate fake targets to deceive target tracking systems (Farina and Skolnik 2008). RGPO ECM is a type of ECM that intercepts radar signals and retransmits a deception signal with a progressive time delay, pulling the range gate of the radar target tracker further away from the actual target over time (Zhou et al. 2021). On the other hand, VGPO is employed by injecting a frequency-shifted replica of the received radar signal; the frequency of the false return is slowly altered to interfere with the true Doppler shift (Deng et al. 2013). Digital radio frequency memory (DRFM) devices are generally used to store and regenerate captured radar signals to confuse hostile radars (Berger 2003a). In addition, because of advances in computing capability and hardware ar-

chitecture, the DRFM can simultaneously process multiple captured signals, allowing a modern repeater to deploy deception jamming on multiple-radar devices (Berger 2003b).

Electronic Counter Countermeasures (ECCM) are broadly classified into signal processing based techniques and target tracking based techniques. In signal processing based approaches, most radar systems are provided with ECCM capabilities to combat deception jamming. The ECCM techniques such as pulse diversity, polarization character, motion function, DRFM quantization error, and target detection system in the presence of interference ensure that no single radar is tricked (Berger 2003b, Liu et al. 2013, Huang et al. 2013, Greco et al. 2005, Rao et al. 2012, 2010). In (Wang et al. 2020), an efficient ECCM approach for countering the very high-power ECM using an orthogonal frequency division multiplexing (OFDM) radar is presented and analyzed. Here, the phase codes of the sub-carriers belonging to the OFDM pulses are tuned to limit the jamming strength to suppress range deception and combined range-velocity deception jamming (Wang et al. 2020).

Most sensors may not know the ECM techniques; however, they are resolved using efficient target tracking. The effect of RGPO on radar target tracking with benchmark targets is studied in (Blair et al. 1998) and (Blair et al. 1995). In particular, controlling the beam pointing of phased array radar for benchmark target tracking problems in the existence of RGPO and false alarms is investigated in (Blair et al. 1998, 1995). The impact of target amplitude variations, beam shape, missed detections, false alarms, finite resolution, target motions, and track loss was included in the test-bed simulation described in (Blair et al. 1998). Further, in (Slocumb et al. 1995), the solution for the second Benchmark problem of tracking a maneuvering target in the existence of RGPO using variable state dimension Kalman filter is presented. Authors in (Slocumb et al. 1995) have deployed adaptive waveform selection and dwell revisit time selection methods and track filter coasting for handling the uncertainties introduced by false alarms, missed detection, maneuvers, and RGPO. Further, for tracking highly maneuvering targets, a comprehensive framework is presented in (Kirubarajan et al. 1998) in the presence of false alarms, SOJ, and RGPO. Mainly, the algorithms for track generation and maintenance, adaptive target revisit interval selection, waveform selection, and detection threshold; and neutralizing ECM

approaches were discussed in depth in (Kirubarajan et al. 1998). The interacting multiple model (IMM) estimator, in combination with the probabilistic data association (PDA) technique, is utilized for tracking the targets in (Kirubarajan et al. 1998). Additionally, authors in (Blackman et al. 1999) have suggested the solution to the benchmark target tracking, which addresses the efficient resource allocation in the presence of ECM. The resource allocation problem is solved using interacting multiple model/multiple hypothesis tracking (IMM/MHT) tracker along with target tracking (Blackman et al. 1999).

In (Lu et al. 2011), to counter RGPO and Range Gate Pull-In (RGPI) jamming, an ECCM approach based on loss of balance in the range tracking loop is presented and analyzed. Further, using adaptively updated bias weight in every range tracking interval according to the error signal, which balances the energy of the early and late gates concerning the target and continues to track the target with insignificant track loss is presented in (Lu et al. 2011). Furthermore, memory tracking and narrow gate monitoring were used to propose and assess a novel ECCM approach against deception jamming in (Xiongjun Fu et al. 2009). In addition, authors in (Xiongjun Fu et al. 2009) have concluded that the proposed method provides significant efficacy while countering all types of RGPO. In (Xiong et al. 2016), the spatial filtering technique using trilinear decomposition to overcome the effect of deception jamming is presented and analyzed. Further, authors in (Zhao and Liu 2017) have proposed a composite approach to estimate the location of the target and deception range for distinguishing between false targets and true targets. The data fusion-based approaches are proposed to distinguish false targets using data correlation algorithms and local radar measurements (range, angle, and Doppler information). On the other hand, signal fusion-based techniques explore the ECCM abilities of multiple-radar systems by utilizing amplitude and phase information of the target echoes to provide efficient countermeasures (Zhao et al. 2016). The most generic and systematic approach for mitigating the effect of RGPO on target tracking is Decomposition and Fusion (DF), where the deception measurements have virtually the same angles as that of true measurements (Li et al. 1999, Slocumb et al. 2000). The fundamental steps involved in the DF technique are decomposition of validated measurements using hypothesis testing, track filtering for range deception measurements, conventional filtering, and

performing a fusion of these estimates.

Considering the above review of the literature, most of the existing contributions have addressed the effect of RGPO ECM in either signal or target tracking perspective. Further, there are insignificant research works that focus on countermeasures to RGPO ECM in a networked radar from a target tracking and fusion perspective. This motivated us to carry out the research work to propose an efficient target tracking framework to combat range deception ECM in a networked radar scenario.

2.2 Transmitters of Opportunity for Passive Radar

The ambient radio-frequency illumination provided by transmitters such as television, radio, cellular telephone towers, and other active radars in the given surveillance area is used by passive radar instead of transmitting radio-frequency signals. Passive radar has some advantages over the active radar, especially in terms of covertness and spectrum utilization. Since it uses the existing waveforms, it is named green radar (Kuschel et al. 2019b). The concept behind passive radar is to cross-correlate the signal received directly from a transmitter with its reflections from a target. The passive radar uses IOOs to locate the target. The correct detection or tracking of the target depends mainly on the availability of good quality IOO.

The passive radar can use signals from broadcast communication systems, mobile signals, and signals from other active radars. The most commonly used earthbound IOOs are Frequency Modulation(FM), Digital Audio Broadcasting (DAB), Digital Video Broadcasting (DVB), and Long Term Evolution (LTE) for long-distance surveillance applications. Whereas, for indoor localization, WiFi signals are adopted by passive radars. Among the space-borne IOOs, the Global Positioning System (GPS), Global Navigational Satellite System (GNSS), and DVB-Satellite (DVB-S) signals are typically utilized for long-range tracking applications by the passive radar. The available transmitters of opportunity are classified as indicated in Fig. 2.1. The FM is an analog signal. The adequate instantaneous bandwidth of an FM signal is highly dependent on the program being broadcasted. Constant signal features, such as constant bandwidth and desired range resolution, Doppler resolution, and side-lobe characteristics are guaranteed by digital broadcast services such as DAB and DVB-T.

On the other hand, Digital modulation systems have a problem due to periodicities in the signal structure which may introduce artifacts in the passive radar processing (Coleman et al. 2008).

GSM cellular phone networks are strong candidates for IOO for passive radar due to their broad coverage area. Global Navigation Satellite System (GNSS) systems provide broad coverage when considering the satellite class of illuminators of opportunity. However, the Equivalent Isotropically Radiated Power (EIRP) of GNSS is typically inadequate for Passive Coherent Locator (PCL) systems (Griffiths et al. 2002). In brief, a good IOO for passive radar should provide a stable continuous transmitted signal over time, with a substantial EIRP. Furthermore, digital transmissions are typically more favorable than analog transmissions such as FM. So, the EIRP of IOO under consideration should be uniform. The choice of physical layer
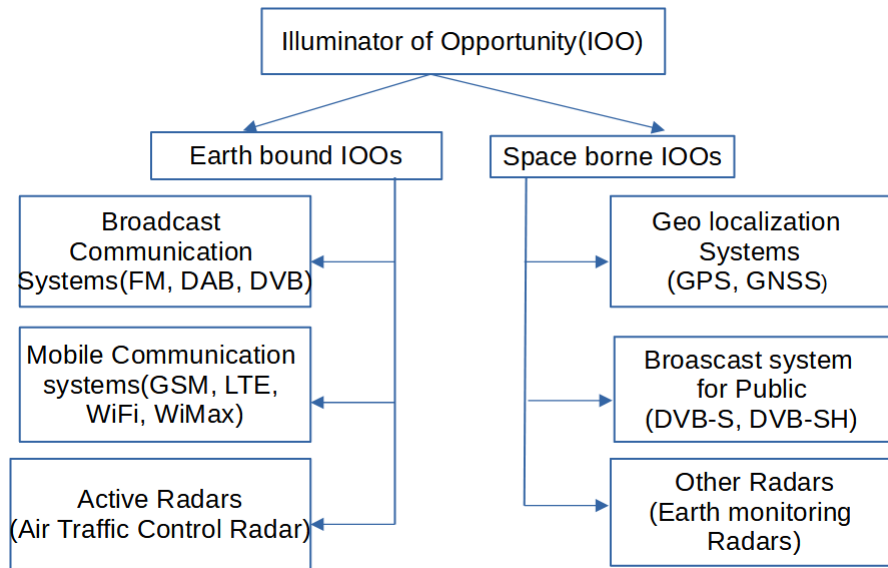
Figure 2.1: Illuminator of Opportunity Classification

waveform for 5G is an essential important thing. Third generation partnership project (3GPP) carrying out the standardization activity for the 5G system in 5G New Radio (NR). Based on the release of 3GPP 38.211, the most significant difference between 5G NR and LTE is that 5G NR uses Cyclic Prefix Orthogonal Frequency Division Multiplexing (CP-OFDM) for downlink and CP-OFDM or Discrete Fourier Transform Spread OFDM (DFT-s-OFDM) for up-link depending on the use case (Kongara et al. 2019). CP-OFDM is a multi-carrier modulation technique that maps the sym-

bols into orthogonal subcarriers. The cyclic prefix inserted at the end is appended to the beginning to ensure the circularity of the OFDM symbol. The main advantage of CP-OFDM is that it has lower implementation complexity and lower cost, even for wideband applications (Lin et al. 2019).

In 3GPP, there are approximately two frequency ranges defined in 5G NR. The first is what we call (sub 6 GHz), and the second is millimeter-wave (Henry et al. 2020). The maximum bandwidth and subcarrier spacing differ depending on the ranges. The maximum bandwidth in the sub-6 GHz range is 100 MHz, while the maximum bandwidth in the millimeter-wave range is 400 MHz. Some subcarrier spacing (15, 30 kHz) is only available in the sub-6 GHz range, whereas others (120 kHz) are only available in the millimeter-wave range (ShareTechNote). Some subcarrier spacing (60 kHz) is used both in sub 6 GHz and millimeter wave range (Gerzaguet et al. 2016).

In (Vorobev et al. 2016), the feasibility of adopting digital video broadcasting terrestrial (DVB-T) as a transmitter of opportunity is carried out empirically. The signal-to-noise ratio (SNR), signal-to-interference ratio (SIR), and the ambiguity functions are analyzed for the DVB-T signal. The usefulness of LTE signal for target tracking with passive radar is discussed in (Salah et al. 2013). The range resolution, Doppler resolution, velocity resolution, and ambiguity function analysis are carried out. Passive radars can use the signals from other radars for tracking or detection applications. In (Samczynski et al. 2015), the conceptual analysis of using pulsed radar signals from other active radars for passive radar application is presented. Recently, the pseudo-noise signal analysis for utilizing as an IOO has been discussed in (Fang et al. 2019). The signal processing aspects of Pseudo noise signals, which aid passive radar in tracking applications, are studied empirically. The above-mentioned (Salah et al. 2014, Fang et al. 2019, Liu et al. 2018, Vorobev et al. 2016, Samczynski et al. 2015) works motivated us to explore the features of 5G NR waveform, as a candidate IOO for passive radar in target detection and tracking applications.

2.3   Impact of Losses on IOOs

For air space observation and air traffic control, passive radar systems are used as an alternative solution to active radar systems (Rai et al. 2021). Broadcast networks

and third-party networking systems are available in many parts of the world. They efficiently illuminate the given surveillance space for passive bistatic radar (Kuschel et al. 2019b). Frequency Modulation (FM), Digital Audio Broadcasting (DAB), Digital Video Broadcasting Terrestrial (DVB-T), Long Term Evolution (LTE), Digital Video Broadcasting Satellite (DVB-S), Global System for Mobile (GSM) communication, Global Positioning System (GPS), Global Navigational Satellite System (GNSS), WiFi and signals from other active pulsed radars are the frequently adopted IOOs for bistatic passive radars (O'Hagan et al. 2017). Besides, constant signal features, such as higher signal strength, constant bandwidth, improved range resolution, enhanced Doppler resolution, and lower side-lobe characteristics, are expected from a good quality IOO for passive bistatic radar (Salah et al. 2013, Berger et al. 2010, Howland et al. 2008). In (Salah et al. 2013, Samczynski et al. 2015, Salah et al. 2014, Wang et al. 2010, Oyedokun 2011, Liu et al. 2018,and Fang et al. 2019) authors investigated the feasibility of LTE signal, WiMax signal, DTV signal, OQAM signal and Pseudo Noise (PN) signal as an IOO for the passive bistatic radar by ignoring the atmospheric effects on the signal propagation. Since the IOO signal propagates through the medium, it undergoes various losses due to atmospheric effects. Specifically, the IOO signal gets attenuated due to absorption, reflection, refraction, scattering, and fading as it passes through the ionosphere. Further, IOO signal energy diminishes as a result of absorption, clouds, rain attenuation, and attenuation due to snow, hail, and fog in the troposphere and stratosphere (Mason 2010).

At frequencies above 10 GHz, rain is the most frequent source of attenuation (Barott et al. 2018). The interaction of free electrons, ions, and molecules in the atmosphere with the IOO signal is highly affected by frequency and is termed gas attenuation (Rosenberg et al. 2020). Air gases attenuate at microwave and millimeter wave (mmWave) frequencies due to oxygen and water vapor absorption. Besides, oxygen and water vapor in the lower atmosphere directly induce path attenuation at higher frequencies, precisely at 22 GHz and 60 GHz (Zubair et al. 2011). Moreover, the refraction of the signal lead to changes in propagation velocity and direction of the wave (Amirabadi and Tabataba Vakili 2018). The temperature and moisture changes along the transmission path also induce local signal refraction, resulting in signal degradation and increased noise. Further, in a foggy, atmospheric condition,

where the droplets of water are suspended in the air attenuates the propagation of the IOO signal, which can be considered fog loss (Etinger et al. 2020). Furthermore, the attenuation of the IOO signal due to vegetation obstructing the propagation of the EM wave is termed foliage loss.

The losses in the wireless propagation due to atmospheric gases, clouds, and rain at mmWave and terahertz frequencies have been studied through simulations and experiments in (Siles et al. 2015). The authors claimed that the signal suffers from significant rain attenuation below 90 GHz and becomes constant above 90 GHz. It is further evident from the results of (Siles et al. 2015) that the attenuation due to gas and cloud are accountable at frequencies around 60 GHz. In (Erdoğan and Ilgin 2018), the atmospheric effects (loss, rain loss, and gas losses) on millimeter frequency bands from 24 GHz to 86 GHz has been studied and analyzed at 500 m. Similarly, the effect of atmospheric absorption on mmWave frequencies for 5G networks is simulated and analyzed in (Banday et al. 2019). In (Banday et al. 2019), along with gas and rain losses, the foliage effects have been studied at 28 GHz, 39 GHz, 50 GHz, and 60 GHz and observed that the path loss increases as the frequency increases. In (Golovachev et al. 2020), the analysis of atmospheric effects is performed on orthogonal frequency division multiplexing (OFDM) transmission schemes, and it is noticed that the amplitude and phase changes occur owing to atmospheric effects. Further, the simulation study in (Golovachev et al. 2020) considered the channel model for mmWave frequencies, particularly 5G NR FR1 and FR2 specifications with 200 MHz bandwidth, and observed that the error rate is increased in the presence of atmospheric effects. The authors in (Zhang et al. 2019) proposed the propagation model for 28 GHz millimeter wave in the coniferous forests using high-resolution LiDAR for measurements and compared the three empirical foliage models, namely the attenuation factor (AF) model, International Telecommunication Union Radio communication (ITU-R) woodland model, and Weissberger's model. In addition, in (Kim et al. 2020), diffraction loss models for mmWave propagation at 28 GHz, 32.4 GHz, and 38 GHz have been analyzed. Interestingly, the experimental results showed higher losses than the Knife Edge Diffraction (KED) model with large Fresnel-Kirchhoff diffraction parameters.

Most of the above recent research articles (Siles et al. 2015, Erdoğan and Ilgin

2018, Banday et al. 2019, Golovachev et al. 2020, Zhang et al. 2019, Kim et al. 2020 and Lingadevaru et al. 2021) have presented the mathematical models for the simulation of the various losses owing to propagation of high-frequency signals. Although the majority of these works have highlighted the losses incurred by the mmWave propagation, there is a minimal research study on the effects of atmospheric losses and receiver system losses for various IOOs ranging from VHF to mmWave frequencies from a passive radar perspective. Moreover, most of the IOO signal feasibility studies for passive bistatic radar conducted in (Salah et al. 2013, Berger et al. 2010, Howland et al. 2008, Samczynski et al. 2015, Salah et al. 2014, Wang et al. 2010, Oyedokun 2011, Liu et al. 2018, Fang et al. 2019) have ignored the losses. Therefore, there is a strong need to incorporate various losses into the analytical study of the different IOOs for the passive radar framework to address the problem properly. Further, there is also further necessity to find the effect of atmospheric and signal processing losses on different IOOs. Besides, the effect of diffraction and foliage loss is also significant. Hence this motivated us to comprehensively study the impact of various losses on different IOOs.

2.4 Motivation

The range deception jamming is the most effective of all the ECM techniques that generate fake targets to deceive target tracking systems and is the major threat to the target detection and tracking systems. In RGPO, the target senses the radar pulse and repeats it with a control delay. The amplified, repeated/delayed pulse results in a false range measurement with a signal-to-noise (S/N) ratio larger than the real target range measurement confusing the radar/target detection and tracking process. Accordingly, there is a need for countermeasure against the range deception jamming for efficient target detection and tracking.

Further, one of the biggest problems encountered while detecting targets using passive radars is the difficulty in detecting the weak echo signal reflected from the target due to external noise and environmental factors (rain, fog, gases, foliage, etc.), and intentional jammers. Further, the waveforms utilized by passive radars are not optimized for radar purposes which may affect the target detection and tracking per-

formance. Furthermore, in common with all bistatic radars, the resolution in range and Doppler is poor for targets on or close to the baseline between transmitter and receiver.

In view of the wide range of passive radar applications, it is essential to overcome the major drawbacks associated with them through appropriate IOO signal selection and effective signal processing. This is the key motivation to carry out the feasibility study for adopting the 5G NR waveform as an illuminator of opportunity and further carry out a comprehensive external loss analysis for commonly adopted IOOs.

2.5 Research Objectives

The main focus of this research is to investigate efficient algorithms to combat the range deception jamming in target tracking applications. Further, the research work concentrates on analysing the illuminators of opportunity for passive radar. The objectives of the research are as follows:

1. To present efficient target detection and tracking algorithm for Networked Radar System (NRS) in the presence of RGPO ECM.

2. To investigate and analyze 5G NR waveform as an illuminator of opportunity for target detection using passive radars.

3. To propose a conceptual framework for KA-PRS to improve the received signal strength in a passive radar system.

4. Comprehensive analysis of the impact of various losses on illuminators of opportunity for passive radars.

5. To carry out real time experimentation to measure the penetration losses using practical radar system in the indoor environment.

Chapter 3

Estimation of Range Gate Pull-Off Parameter using Sequential Fusion based approach: An ECCM algorithm

3.1   Preamble

In this research objective, an effective ECCM technique based on a sequential fusion approach has been proposed to combat range deception ECM using a networked radar system that is tracking a single target in the given surveillance area. The primary assumption is that there are inadequate signal processing based ECCM techniques deployed, and measurements are corrupted by RGPO ECM. Further, it is assumed that a simple target tracking algorithm is working, and the tracks being reported by the tracker are falsified due to RGPO ECM. The radars in the NRS contain a local tracker to estimate the updated state and covariance of a target. These local tracks are available at the fusion center and performed a T2TA to detect the RGPO ECM attack. It is important to note that the detection alone is inadequate unless mitigation measures are provided. Hence, this motivated us to carry out this investigation to estimate the deception parameter (Δr) of each local track. To construct equivalent measurements of the deceived track, one requires a Kalman gain, which is unavailable from the local tracker. Hence, a tracklet based framework is adopted to re-create a Kalman gain followed by pseudo-measurements and pseudo-measurement covariance. Similarly, all the available local tracks except the deceived track are compensated with the estimated deception parameter and further generated a reference measurement using a sequential fusion algorithm. The pseudo-measurements and reference measurement are then used in the recursive least squares framework to estimate the

deception parameter (Δr) of the deceived track.

3.2   Problem Formulation
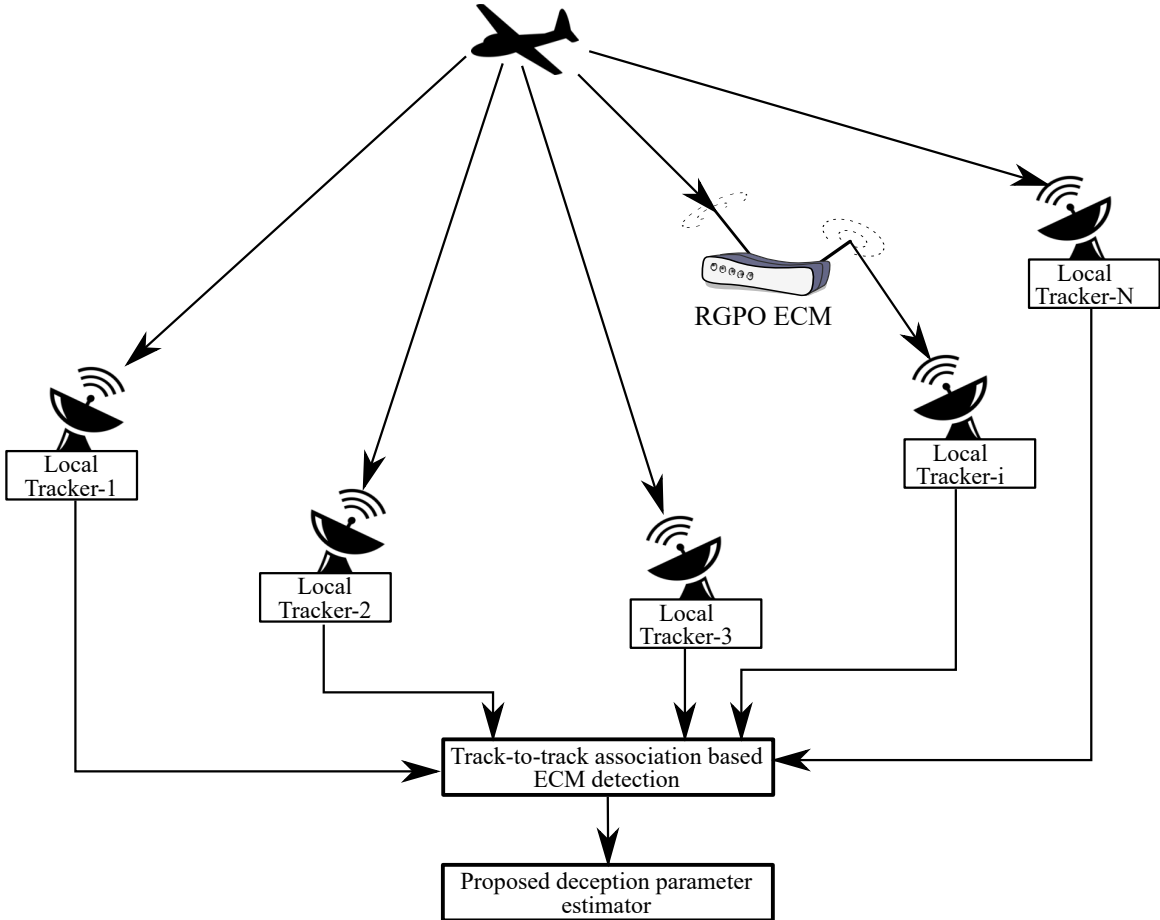
Figure 3.1: Networked radar system tracking a single target and a single local tracker is deceived by RGPO ECM

Consider a surveillance region monitored by NRS consisting of more than two radars. Assume that all the radars are synchronized and provide the measurements related to the targets. The measurement space of the radar is range and azimuth. An RGPO deception jammer is placed in the same surveillance area and sends deceptive signals to mislead either one or more radars of NRS. The RGPO ECM technique corrupts the measurements at one or more radars. The scenario of NRS in which one of the radars is deceived by a single RGPO jammer, as shown in Fig. 3.1. In the first case, a single radar sensor, as shown in Fig. 3.1, is assumed to be affected by the RGPO ECM and results in deceived track, as shown in Fig. 3.2. In the second

case, multiple radar sensors are considered to be affected by RGPO ECM and lead to multiple deceived tracks, as shown in Fig. 3.3.

3.2.1 State Model

The target state model is expressed as,

$$\mathbf{x}(k+1) = \mathbf{F}\mathbf{x}(k) + \Gamma_x \mathbf{v}(k), \tag{3.1}$$

where $\mathbf{x}(k)$ is m_x dimensional state vector consisting of position and velocity of the target at the discrete time instant k. $\mathbf{F}$ is the state transition matrix which follows constant velocity (CV), constant turn (CT), and constant acceleration (CA) depending on the state dynamics. Γ_x is noise gain matrix (Bar-Shalom et al. 2004) and $\mathbf{v}(k)$ is the process noise that follows Gaussian PDF with covariance,

$$\mathbf{Q}_x = E[\mathbf{v}(k)\mathbf{v}(k)^T]. \tag{3.2}$$

Here $E[.]$ and $[.]^T$ indicates the expectation and transposition operator respectively.

The measurement model without the impact of RGPO ECM is given by,

$$\mathbf{z}_i(k) = \begin{bmatrix} r_i(k) + w_{r_i}(k) \\ \theta_i(k) + w_{\theta_i(k)} \end{bmatrix} ; i = 1, \dots . N, \tag{3.3}$$

where $\mathbf{z}_i(k)$ is the measurement vector of m_z dimension (which contains range (r_i) and azimuth (θ_i) corresponding to the target). $w_{r_i}(k)$ and $w_{\theta_i(k)}$ follows Gaussian PDF with zero mean and standard deviation $\sigma_{r_i}^2$ and $\sigma_{\theta_i}^2$ respectively.

The equivalent representation of (3.3) is,

$$\mathbf{z}_i(k) = \mathbf{H}\mathbf{x}_i(k) + \mathbf{w}_i(k); i = 1, \dots . N. \tag{3.4}$$

where $\mathbf{H}$ is the $m_z \times m_x$ measurement transition matrix and $\mathbf{w}_i(k)$ follows Gaussian PDF with zero mean and covariance $\mathbf{R}_z$ that can be expressed as,

$$\mathbf{R}_z = E[\mathbf{w}_i(k)\mathbf{w}_i(k)^T] \tag{3.5}$$

As shown in Fig. 3.1, in the presence of ECM the above measurement model is as given in (Yang et al. 2018),

$$\mathbf{z}_i(k) = \begin{bmatrix} r_i(k) + \Delta r_i(k) + w_{r_i}(k) \\ \theta_i(k) + w_{\theta_i(k)} \end{bmatrix} ; i = 1, \dots . N. \tag{3.6}$$

Here, it is assumed that the target range information deceived by the jammer and as a result i^{th} radar true range is displaced by a value due to RGPO deception $\Delta r_i(k)$.

The measurement in the presence of RGPO ECM can be represented as,

$$\mathbf{z}_i(k) = \begin{bmatrix} r_i(k) \\ \theta_i(k) \end{bmatrix} + \mathbf{c}_i(k)\Delta r_i(k) + \begin{bmatrix} w_{r_i}(k) \\ w_{\theta_i(k)} \end{bmatrix}; i = 1,\ldots.N, \tag{3.7}$$

where, $\mathbf{c}_i(k) \triangleq \begin{bmatrix} 1 & 0 \end{bmatrix}^T$. The polar measurements are converted to Cartesian because most trackers work in Cartesian coordinates. Also, it is further assumed that the conversion will not introduce any bias.

For Unbiasedness, the following condition (3.8) should be satisfied.

$$\frac{r_i \sigma_{\theta_i}^2}{\sigma_{r_i}^2} \ll 0.4. \tag{3.8}$$

Further, i^{th} radar has the measurements

$$\mathbf{z}_i(k) = \mathbf{H}(k)\mathbf{x}_i(k) + \mathbf{B}_i(k)\mathbf{c}_i(k)\Delta r_i(k) + \mathbf{w}_i(k), \tag{3.9}$$

where, the state vector $\mathbf{x}(k) = [x(k) \ \dot{x}(k) \ y(k) \ \dot{y}(k)]^{\mathrm{T}}$ and

$$\mathbf{H}(k) = \begin{bmatrix} 1 & 0 & 0 & 0 \\ 0 & 0 & 1 & 0 \end{bmatrix} \triangleq \mathbf{H}. \tag{3.10}$$

The matrix $\mathbf{B}_i(k)$ is a nonlinear function with the true range and azimuth. Using the the measured azimuth $\theta_i^m(k)$ and range $r_i^m(k)$ from radar i, $\mathbf{B}_i(k)$ can be written as given in (Rao et al. 2010),

$$\mathbf{B}_i(k) = \begin{bmatrix} \cos\theta_i^m(k) & -r_i^m \sin\theta_i^m(k) \\ \sin\theta_i^m(k) & r_i^m \cos\theta_i^m(k) \end{bmatrix}. \tag{3.11}$$

In the above, superscript m indicates measured value. Finally, the new covariance matrix of the measurements in Cartesian coordinates (omitting index k in the measurements for clarity) can be written as,

$$\mathbf{R}_{z_i} = \begin{pmatrix} r_i^2\sigma_{\theta_i}^2 \sin^2\theta_i + \sigma_{r_i}^2\cos^2\theta_i & (\sigma_{r_i}^2 - r_i^2\sigma_{\theta_i}^2)\sin\theta_i\cos\theta_i \\ (\sigma_{r_i}^2 - r_i^2\sigma_{\theta_i}^2)\sin\theta_i\cos\theta_i & r_i^2\sigma_{\theta_i}^2\cos^2\theta_i + \sigma_{r_i}^2\sin^2\theta_i \end{pmatrix}.$$

However, one can use the observed range and azimuth as well.

The above given model in (3.6), is equivalent to the established RGPO measurement model presented in (Slocumb and West 2000) and is represented as,

$$r_d(k) = \begin{cases} r(k), & t_k \le t_0 + T_{ca} \\ r(k) + \Delta r(k), & t_k > t_0 + T_{ca} \end{cases} \tag{3.12}$$

where, $r_d(k)$ is the deceived false range of the target from the radar, $r(k)$ is the actual range, and $\Delta r(k) = \frac{c\Delta t_k}{2}$ is the deviation in the range due to the influence of RGPO ECM. Here, Δt_k is the time delay in the ECM delay line as presented in (Slocumb and West 2000). Further, t_0 is the start time of the range deception, c is the speed of light and, T_{ca} represents the length of time that the false target should evolve.

Further, the jamming to signal ratio can be obtained as derived in (Richards et al. 2010). The received power at the radar can be expressed as,

$$P_{rx} = \frac{P_{tx}G_{tx}G_{rx}\lambda_x^2\sigma_x}{(4\pi)^3 R_x^4 L_s} \tag{3.13}$$

where, P_{tx} is the peak transmitted power in watts, G_{tx} is the gain of the transmit antenna, G_{rx} is the gain of the receive antenna, λ_x is the carrier wavelength in meters, σ_x is the radar cross section of the target in square meters, R_x is the range from the radar to the target in meters, and L_s is the total receiver system losses.

The total power received at the radar from the jammer can be written as,

$$P_{jr} = \frac{P_{jx}G_{jx}G_{jr}\lambda_x^2}{(4\pi)^2 R_j^2 L_{jr}} \tag{3.14}$$

where, P_{jx} is the peak transmitted jammer power in watts, G_{jx} is the gain of the jammer antenna, G_{jr} is the gain of the radar antenna in the direction of the jammer, λ_x is the carrier wavelength in meters, R_j is the range from jammer to the radar in meters, and L_{jr} is the total jammer related losses.

Considering the ratio of jammer power (P_{jr}) to radar received power (P_{rx}), the jamming to signal ratio (JSR) can be expressed as,

$$JSR = 4\pi * \frac{P_{jx}G_{jx}G_{jr}R_x^4 L_s}{P_{tx}G_{tx}G_{rx}\sigma_x R_j^2 L_{jr}} \tag{3.15}$$

Generally, the jamming power will be much higher than the radar signal power, which helps the jammer deceive the radar. Several signal processing based techniques like the waveform diversity method and singular spectrum analysis for countering the RGPO ECM are presented in (Zhang et al. 2009, Lu et al. 2016). On contrast, this work considers the measurement level processing for countering the RGPO ECM.

3.2.2 Preliminary observations
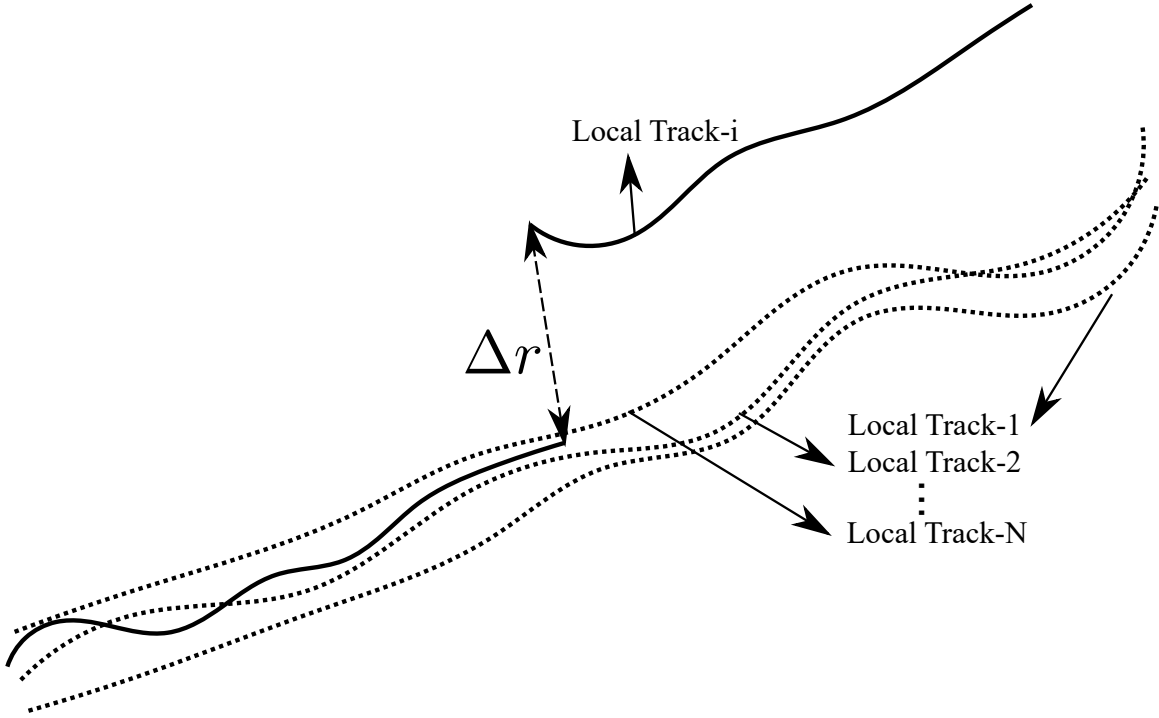
Figure 3.2: i^{th} local track is deceived by the RGPO ECM in single-target using multiple-radar case.

From Fig. 3.2 it can be seen that the range measurement of radar-i is deceived. This deception results in a false track, as shown in Fig. 3.2, after performing the distributed tracking. The primary objectives proposed in this research work are:

1. The local tracker processes the measurements and provides the local estimates (estimated state and covariance). At the fusion center, only local estimates are available, and no other data is available from the radar or tracker. Hence, the measurements are to be recreated at the fusion center by using the local tracks. This recreation of measurements is possible by evaluating the tracklets (He et al. 2020).

2. One needs to formulate a method to associate the local tracks corresponding to the same target so that those tracks can be utilized as a reference to estimate the deception occurrence in other tracks. This association can be formulated as a track-to-track association and solved using S-Dimensional (S-D) assignment (Popp et al. 1998).

3. The deception parameter of the RGPO ECM track is to be estimated by using undeceived local tracks. These undeceived local tracks can be fused to generate a reference measurement.
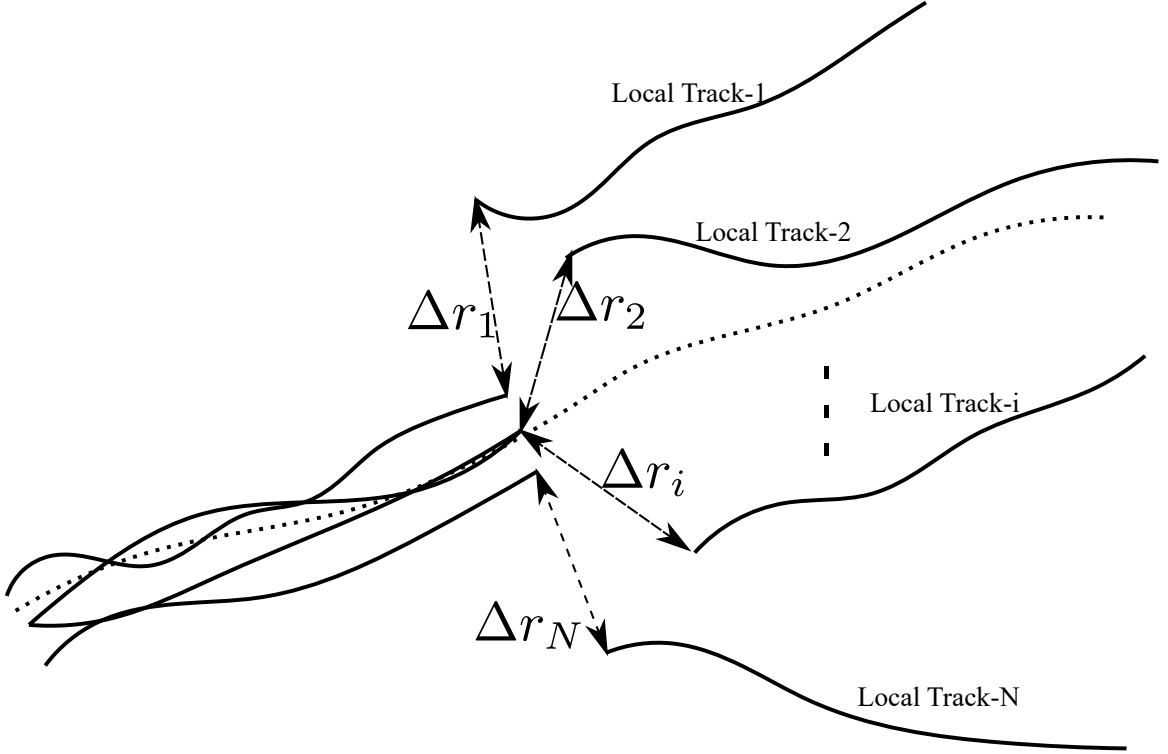
Figure 3.3: All local tracks deceived by the RGPO ECM in single-target multiple-radar case.

3.3 Distributed Tracking and Track-to-track Association

3.3.1 Distributed Tracking

All radars are deployed with local trackers as shown in Fig. 3.1. The radar is ignorant about the measurements corresponding to the target, whether it is a true measurement or false measurement due to RGPO ECM. The tracker works with the converted measurements. For the acquired measurement, the local tracker provides the local estimates (estimated state and covariance). Given the previous state estimate $\hat{\mathbf{x}}^i(k|k)$, the KF state prediction for $i = 1, \ldots .N$ radars is written as,

$$\hat{\mathbf{x}}^i(k+1|k) = \mathbf{F}\hat{\mathbf{x}}^i(k|k), \tag{3.16}$$

27

where k is the discrete time instant and $\mathbf{F}$ is a state transition matrix. Similar to the state prediction, for the given covariance $\mathbf{P}(k|k)$ at the kth instant, the predicted covariance at the $k + 1^{th}$ instant is represented as,

$$\mathbf{P}^i(k+1|k) = \mathbf{F}\mathbf{P}^i(k|k)\mathbf{F}^T + \Gamma_x\mathbf{Q}_x\Gamma_x^T, \tag{3.17}$$

where $\mathbf{Q}_x$ is the process noise covariance and Γ is the noise gain matrix as given in (Zhang et al. 2020).

The measurement prediction is,

$$\hat{\mathbf{z}}^i(k+1) = \mathbf{H}(k+1)\hat{\mathbf{x}}^i(k+1|k) \tag{3.18}$$

The innovation of the filter is,

$$\nu_z^i(k+1) = \mathbf{z}^i(k+1) - \mathbf{H}(k+1)\hat{\mathbf{x}}^i(k+1|k) \tag{3.19}$$

The updated state is designated as,

$$\hat{\mathbf{x}}^i(k+1|k+1) = \hat{\mathbf{x}}^i(k+1|k) + \mathbf{W}^i(k+1)\nu_z^i(k+1), \tag{3.20}$$

where, $\mathbf{W}^i(k+1)$ is the Kalman gain and is computed as,

$$\mathbf{W}^i(k+1) = \mathbf{P}^i(k+1|k)\mathbf{H}(k+1)^T\mathbf{S}^i(k+1)^{-1}, \tag{3.21}$$

where, $\mathbf{S}^i$ is the innovation covariance and is represented as,

$$\mathbf{S}^i(k+1) = \mathbf{H}(k+1)\mathbf{P}^i(k+1|k)\mathbf{H}(k+1)^T + \mathbf{R}_z^i. \tag{3.22}$$

Here $\mathbf{R}_z$ is the measurement covariance matrix. Finally, the updated covariance matrix is given by,

$$\mathbf{P}^i(k+1|k+1) = \mathbf{P}^i(k+1|k) - \mathbf{W}^i(k+1)\mathbf{S}^i(k+1)\mathbf{W}^i(k+1)^T. \tag{3.23}$$

In a single RGPO ECM case, out of all the local tracks, only one track (local track-i) is falsified by the RGPO ECM, as illustrated in Fig. 3.2. Here, we can see that the local track corresponding to local track-i is deviated by Δr_i from its true position as comprehensively derived in (Yang et al. 2016). One has to perform track-to-track association to all local tracks, and it should report that all local tracks correspond to same-origin except i^{th} track. In another case, if N jammers are employed to deceive all the local tracks, the local tracks appear as Fig. 3.3. In this case, one should report that all the tracks are from a different origin. The track-to-track association is presented in the subsequent section to address this issue.

3.3.2 Track-to-track Association (T2TA)

The fusion of target tracks from multiple sensors is an essential block in the sensor fusion field. The information from multiple sensors has the potential to significantly improve tracking accuracy and target acquisition rates. Out of all the variants of track-to-track associations (La Scala and Farina 2002), the hypothesis-based track-to-track association is popular. It can improve tracking accuracy even with less target detection probability and high false alarm rates. The N radars will have their own number of tracks in the form of target estimate $\hat{\mathbf{x}}_{n_i}^i$ with their errors distributed as zero-mean Gaussian with covariance $\mathbf{P}_{n_i}^i$. The $i = 1, 2, \ldots, N$, represents radar number and $n_i = 1, 2, \ldots, T$ represents number of tracks that the each radar generates. To find out the tracks that represents the same target, it is required to perform the likelihood ratio test, given by

$$\chi(H_{n_1,n_2,\ldots,n_N}^1 : H_{n_1,n_2,\ldots,n_N}^0) = \frac{\Lambda(H_{n_1,n_2,\ldots,n_N}^1)}{\Lambda(H_{n_1,n_2,\ldots,n_N}^0)}, \tag{3.24}$$

where, $\Lambda(H_{n_1,n_2,\ldots,n_N}^1)$ represents the likelihood hypothesis of tracks having the common origin, $\Lambda(H_{n_1,n_2,\ldots,n_N}^0)$ represents the likelihood hypothesis of tracks coming from the different origin.

Calculating the likelihood hypothesis of tracks having a common origin is as follows:

$$\Lambda(H_{n_1,n_2,\ldots,n_N}^1) = p(\hat{\mathbf{x}}_{n_N}^N, \ldots, \hat{\mathbf{x}}_{n_1}^1 | H_{n_1,n_2,\ldots,n_N}^1). \tag{3.25}$$

The (3.25) can also be written conditioned on the track estimate of the first radar, given by,

$$\Lambda(H_{n_1,n_2,\ldots,n_N}^1) = p(\hat{\mathbf{x}}_{n_N}^N, \ldots, \hat{\mathbf{x}}_{n_2}^2 | H^1, \hat{\mathbf{x}}_{n_1}^1) p(\hat{\mathbf{x}}_{n_1}^1 | H^1). \tag{3.26}$$

The $p(\hat{\mathbf{x}}_{n_1}^1 | H^1)$ is independent of $H_{n_1,n_2,\ldots,n_N}^1$, hence it can be relaxed. Also, it is assumed to follow uniform distribution, which is a valid assumption in the presence of lack of information. i.e.,

$$p(\hat{\mathbf{x}}_{n_1}^1 | H_{n_1,n_2,\ldots,n_N}^1) = p(\hat{\mathbf{x}}_{n_1}^1) = \frac{1}{C}. \tag{3.27}$$

Substituting, (3.27) into (3.26) results in

$$\Lambda(H_{n_1,n_2,\ldots,n_N}^1) = \frac{1}{C} p(\hat{\mathbf{x}}_{n_N}^N, \ldots, \hat{\mathbf{x}}_{n_2}^2 | H^1, \hat{\mathbf{x}}_{n_1}^1). \tag{3.28}$$

Consider the two radar (i, j) case having two tracks (n_i, n_j) as common target origin. Under the Gaussian assumption, if the tracks $\hat{\mathbf{x}}^i_{n_i}$ and $\hat{\mathbf{x}}^j_{n_j}$ at radar i and radar j results from the same target, the likelihood function of the two tracks is given by,

$$\Lambda(H_{n_1,n_2}) = \frac{1}{C} N(\hat{\mathbf{x}}^i_{n_i} - \hat{\mathbf{x}}^j_{n_j}; 0, P^i_{n_i} + P^j_{n_j} - P^{i,j}_{n_i,n_j} - (P^{i,j}_{n_i,n_j})^T), \qquad (3.29)$$

where, $N(\mathbf{x}; \bar{\mathbf{x}}, P)$ represents Gaussian distribution of variable $\mathbf{x}$ has mean and covariance as $\bar{\mathbf{x}}$, P, respectively.

Similar to (3.29), the generalized likelihood function of all the common tracks (zero error tracks) $n_1, n_2, \ldots, n_N$ for all N radars is given by

$$\Lambda(H^1_{n_1,n_2,\ldots,n_N}) = \frac{1}{C} N(\hat{\mathbf{x}}, 0, P). \qquad (3.30)$$

Here,

$$\hat{\mathbf{x}} = \begin{bmatrix} \tilde{\mathbf{x}}^{21}, & \tilde{\mathbf{x}}^{31}, & \ldots, & \tilde{\mathbf{x}}^{N1} \end{bmatrix}^T, \qquad (3.31)$$

where, $\tilde{\mathbf{x}}^{ij}$ represents the difference of the estimates resulted from the same target at i^{th} and j^{th} radar, given by

$$\tilde{\mathbf{x}}^{ij} = \hat{\mathbf{x}}^i_{n_i} - \hat{\mathbf{x}}^j_{n_j}. \qquad (3.32)$$

The diagonal elements of $\mathbf{P}$ is given by,

$$\mathbf{P}^{i-1,i-1} = \mathbb{E}[\tilde{\mathbf{x}}^{i1}\tilde{\mathbf{x}}^{i1\prime}|H^1_{n_1,n_2,\ldots,n_N}],$$
$$= \mathbf{P}^1_{n_1} + \mathbf{P}^i_{n_i} - \mathbf{P}^{1,i}_{n_1,n_i} - (\mathbf{P}^{1,i}_{n_1,n_i})^\prime \quad i = 2,\ldots,N \qquad (3.33)$$

where $\tilde{\mathbf{x}}^{ij}$ is defined in (3.32).

The diagonal elements of $\mathbf{P}$ is given by,

$$\mathbf{P}^{i-1,j-1} = \mathbb{E}[\tilde{\mathbf{x}}^{i1}\tilde{\mathbf{x}}^{j1\prime}|H^1_{n_1,n_2,\ldots,n_N}],$$
$$= \mathbf{P}^1_{n_1} - \mathbf{P}^{1,j}_{n_1,n_j} - (\mathbf{P}^{1,i}_{n_1,n_i})^\prime + \mathbf{P}^{i,j}_{n_i,n_j}, \quad i,j = 2,\ldots,N \qquad (3.34)$$

Similar to (3.30), the likelihood hypothesis of tracks coming from different origins follows the same procedure as above, given by

$$\Lambda(H^0_{n_1,n_2,\ldots,n_N}) = p(\hat{\mathbf{x}}^N_{n_N}, \ldots, \hat{\mathbf{x}}^2_{n_2}|H^0, \hat{\mathbf{x}}^1_{n_1})p(\hat{\mathbf{x}}^1_{n_1}|H^0)$$
$$= \prod_{i=2}^{N} p(\hat{\mathbf{x}}^i_{n_i}|H^0, \hat{\mathbf{x}}^1_{n_1})p(\hat{\mathbf{x}}^1_{n_1}|H^0) \qquad (3.35)$$

Similar to (3.27), the $p(\hat{\mathbf{x}}_{n_1}^1 | H_{n_1, n_2, \ldots, n_N}^0)$ is assumed as diffuse prior given by,

$$p(\hat{\mathbf{x}}_{n_1}^1 | H_{n_1, n_2, \ldots, n_N}^0) = p(\hat{\mathbf{x}}_{n_1}^1) = \frac{1}{C}, \tag{3.36}$$

whereas, $p(\hat{\mathbf{x}}_{n_N}^N, \ldots, \hat{\mathbf{x}}_{n_2}^2 | H^0, \hat{\mathbf{x}}_{n_1}^1)$ is assumed to follow Poisson distribution in the state space having the spatial density λ. Therefore, substituting (3.36) into (3.35) yields

$$\Lambda(H_{n_1, n_2, \ldots, n_N}^0) = \frac{1}{C} \lambda^{N-1}. \tag{3.37}$$

Finally, from (3.24), (3.30), (3.37), the likelihood ratio test is given by,

$$\chi(H_{n_1, n_2, \ldots, n_N}^1 : H_{n_1, n_2, \ldots, n_N}^0) = \frac{\frac{1}{C} N(\hat{\mathbf{x}}, 0, P)}{\frac{1}{C} \lambda^{N-1}} = \frac{N(\hat{\mathbf{x}}, 0, P)}{\lambda^{N-1}}, \tag{3.38}$$

For T2TA, let us define the track-to-track assignment algorithm of assigning the N_i tracks resulted from N radars representing the same target. For that, define the binary assignment variable

$$\psi_{i_1, i_2, \ldots, i_N} = \begin{cases} 1; & \text{tracks } i_1, i_2, \ldots, i_N \text{ from same target} \\ 0; & \text{from different target} \end{cases}$$

The multidimensional (S-D) track to track assignment algorithm of finding the most likely hypothesis is the result of the constrained optimization problem given below

$$\min_{\psi_{i_1, i_2, \ldots, i_N}} \sum_{i_1=0}^{T_1} \sum_{i_2=0}^{T_2} \cdots \sum_{i_N=0}^{T_N} c_{i_1, i_2, \ldots, i_N} \psi_{i_1, i_2, \ldots, i_N} \tag{3.39}$$

subject to

$$\sum_{i_2=0}^{T_2} \cdots \sum_{i_N=0}^{T_N} \psi_{j, i_2, \ldots, i_N} = 1, \quad j = 1, 2, \ldots, T_1$$

$$\sum_{i_1=0}^{T_1} \sum_{i_3=0}^{T_3} \cdots \sum_{i_N=0}^{T_N} \psi_{i_1, j, i_3, \ldots, i_N} = 1, \quad j = 1, 2, \ldots, T_2$$

$$\vdots$$

$$\sum_{i_1=0}^{T_1} \cdots \sum_{i_{N-1}=0}^{T_{N-1}} \psi_{i_1, \ldots, i_{N-1}} = 1, \quad j = 1, 2, \ldots, T_N$$

and

$$\psi_{i_1, \ldots, i_N} \in \{0, 1\},$$

$$i_1 = 0, 1, \ldots, T_1,$$

$$\vdots$$

$$i_N = 0, 1, \ldots, T_N$$

The cost function $c_{i_1,i_2,...,i_N}$ in (3.39) can be calculated as

$$c_{i_1,i_2,...,i_N} = -\ln\chi(H^1:H^0). \qquad (3.40)$$

where, $\chi(H^1:H^0)$ is the likelihood ratio given in (3.38)

3.3.3 Observations

After performing the Track to Track Association (T2TA), two cases are possible:

1. In the first case, out of all N local tracks, M local tracks are affected by the ECM as shown in Fig. 3.2, where $N - M \geq 2$. That means at least two local tracks are uninfluenced by the ECM. In this case, the unaffected local tracks are fused to form a reference track. This reference track can be further used to estimate the deception parameter of other radars. However, this solution is sub-optimal since there is a constraint on the number of deceiving local tracks, and fusion is limited to $N - M$ local tracks. By considering only $N - M$ local tracks, we are losing the valuable information available in M local tracks.

2. In the second case, all the local tracks are affected by RGPO ECM, as shown in Fig. 3.3. All the reported local tracks are different, and none are associated. In this case, the tracks are first compensated by the previously estimated deception parameter and fused to form a reference track. Thereafter, the deception parameter of other local tracks is calculated. This algorithm provides a generalized solution irrespective of the number of RGPO jammers.

3.4   Deception Parameter Estimation Algorithm

The block diagram for the overall flow of the proposed algorithm is shown in Fig. 3.4. As observed in the previous section, in case of all the local tracks are deceived, there is no availability of local tracks to fuse and form a reference track. In the first step of the algorithm, measurement recreation is carried out for deceived track in the track-lets framework. On the other hand, the tracklets are computed for the rest of the tracks. These tracklets are compensated using previously estimated deception parameters (In Fig. 3.4 the feedback of previous estimates is shown in dotted lines). Next, the sequential update algorithm is applied to the compensated local tracks to obtain

the fused states and covariance. Using the fused states, the fused measurement (reference measurement) is recreated. Further, perform RLSE by utilizing the recreated measurement of deceived track and the reference measurement.
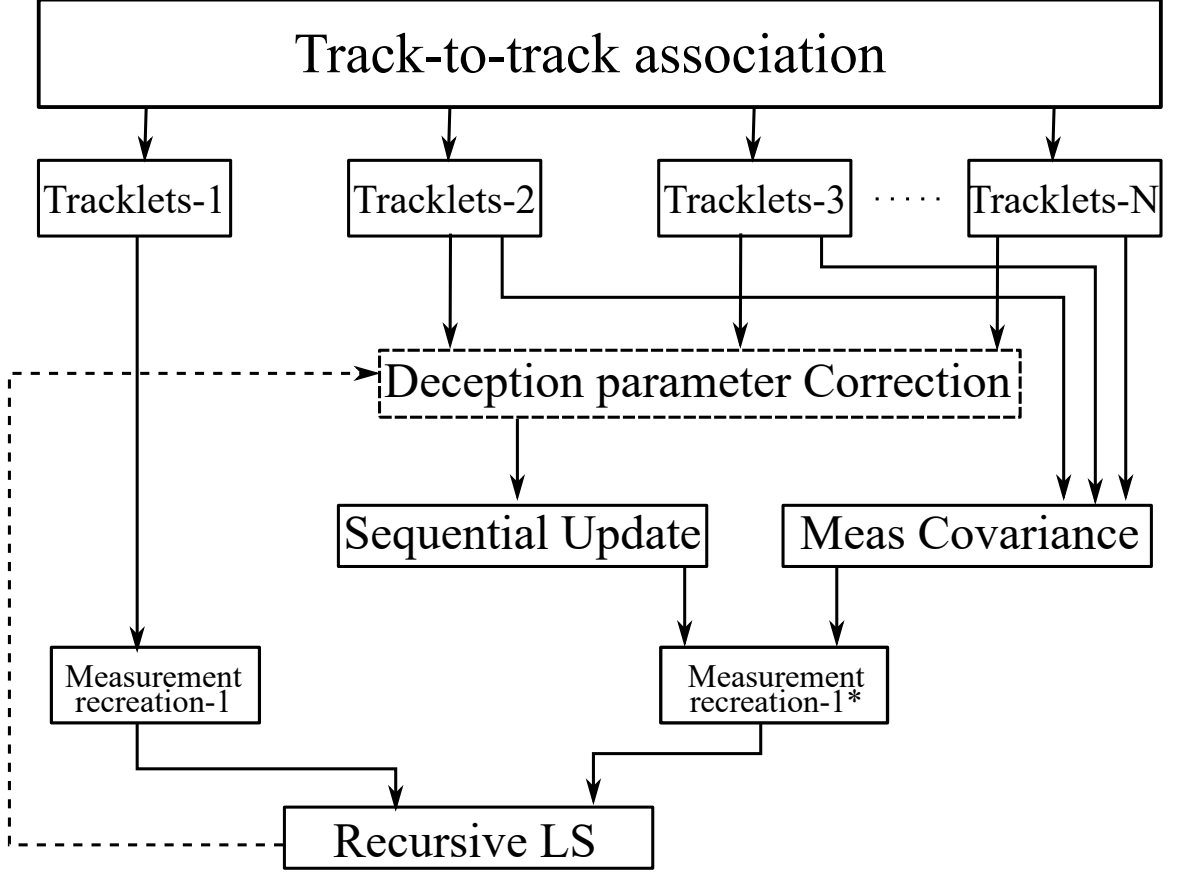
Figure 3.4: The block diagram representation of overall flow of the proposed deception parameter estimation algorithm

3.4.1 Measurement Recreation of Deceiving Track

The local tracker provides the updated states and covariances. However, the measurements are corrupted by the deception parameter. Hence, one needs to recreate the measurements. Once the measurement covariance is known or estimated (i.e. $\hat{\mathbf{R}}_z$), we can rewrite the Kalman gain (3.21) as,

$$\hat{\mathbf{W}}(k+1) = \mathbf{P}(k+1|k)\mathbf{H}(k+1) \tag{3.41}$$
$$\cdot [\hat{\mathbf{R}}_z(k+1) + \mathbf{H}(k+1)\mathbf{P}(k+1|k)\mathbf{H}(k+1)^T]^{-1}.$$

The (3.21) can be rewritten as,

$$\mathbf{x}(k+1|k+1) - \mathbf{F}\mathbf{x}(k|k) = \hat{\mathbf{W}}[\mathbf{y}(k+1) - \mathbf{H}\mathbf{F}\hat{\mathbf{x}}(k|k)], \tag{3.42}$$

where, $\mathbf{y}(k+1)$ is the recreated measurement. Here on the right hand side, gain matrix should be taken to the left side and perform the pseudo inversion as,

$$\hat{\mathbf{W}}(k+1)^{-1} = (\hat{\mathbf{W}}(k+1)^T\hat{\mathbf{W}}(k+1))^{-1}\hat{\mathbf{W}}(k+1)^T, \tag{3.43}$$

Upon rearranging, the recreated measurement can be found as,

$$\mathbf{y}(k+1) = \mathbf{W}(k+1)^{-1}[\hat{\mathbf{x}}(k+1) - (I - \mathbf{W}(k)\mathbf{H}(k))\mathbf{F}(k)^T\hat{\mathbf{x}}(k)] \tag{3.44}$$

At this stage, to successfully recreate the measurements, we need $\hat{\mathbf{R}}_z$. To estimate the $\hat{\mathbf{R}}_z$, we are using Tracklets framework (Zhu et al. 2015). This method constructs the approximately uncorrelated equivalent measurements and the associated covariance matrices from the local tracks. The inverse Kalman filter-based tracklet method from (Drummond 2002) is used. Based on this method, the equivalent measurement vector $\mathbf{u}(k+1,k)$ and measurement covariance $\mathbf{U}(k+1,k)$ can be found using Algorithm-1.

Algorithm 1 Measurement recreation using tracklets

1: inputs:$\mathbf{x}(k|k), \mathbf{P}(k|k), \mathbf{x}(k+1|k+1), \mathbf{P}(k+1|k+1)$
2: At time k
3: **Compute Predictions**
$$\mathbf{x}(k+1|k) = \mathbf{F}\mathbf{x}(k|k)$$
$$\mathbf{P}(k+1|k) = \mathbf{F}\mathbf{P}(k|k)\mathbf{F}^T + \mathbf{Q}_x$$
4: **Compute**
$$\mathbf{A}(k+1,k) = \mathbf{P}(k+1|k)[\mathbf{P}(k+1|k) \\ - \mathbf{P}(k+1|k+1)]^{-1}$$
5: **Compute pseudo-measurement**
$$\mathbf{u}(k+1,k) = \hat{\mathbf{x}}(k+1|k) + \mathbf{A}(k+1|k)[\hat{\mathbf{x}}(k+1|k+1) \\ - \hat{\mathbf{x}}(k+1|k)],$$
6: **Compute pseudo-measurement covariance**
$$\mathbf{U}(k+1,k) = [\mathbf{A}(k+1,k) - I]\mathbf{P}(k+1|k).$$

The detailed derivation of the tracklets is presented in the (Taghavi et al. 2013) and (Sun et al. 2016). We constructed equivalent measurement vector $\mathbf{u}(k+1,k)$ and its error covariance matrix $\mathbf{U}(k+1,k)$. Note that, in order to calculate $\mathbf{u}(k+1,k)$ using $\hat{\mathbf{x}}_f(k+1|k)$ and $\mathbf{P}_f(k+1|k)$, one needs the estimated target state $\hat{\mathbf{x}}(k|k)$ and its covariance matrix $\mathbf{P}(k|k)$.

3.4.2 Correction of Deception Parameter among All Tracks

Consider a case where N RGPO ECM jammers are employed to perform RGPO ECM to all the N local tracks and to result in N deceived local tracks. Here, all tracks get altered due to RGPO ECM, and the deception parameter for each track has to be estimated. In this case, the track-to-track association reports all the tracks are unique and not from a common origin. Therefore, each track is to be first compensated with the estimated range deception parameter (Δr_i) obtained in the previous scans and fuse the compensated tracks to get a fused state and covariance.

The equivalent measurement is $\hat{\mathbf{u}} = [\hat{x}, \hat{y}]$. Since the equivalent measurement is in Cartesian, one can get the measurement in polar by applying the transformation. Therefore, compensate the range in the converted equivalent measurement as

$$r_c(k+1) = \sqrt{(\hat{x}(k+1))^2 + (\hat{y}(k+1))^2} - \Delta r(k) \tag{3.45}$$

Here, $\Delta r(k)$ is the previous estimate and c indicates the corrected measurement.

$$\theta_c(k+1) = \arctan\left(\frac{\hat{y}(k+1)}{\hat{x}(k+1)}\right) \tag{3.46}$$

These corrected polar measurements can be again transformed to Cartesian by standard coordinate conversion without bias as

$$x_m(k+1) = b^{-1} r_c(k+1) \cos(\theta_c(k+1))$$
$$y_m(k+1) = b^{-1} r_c(k+1) \sin(\theta_c(k+1))$$

where, $b \triangleq e^{-\sigma_{\theta_c}^2/2}$. Now these x_m and y_m serve as the local tracker information without being effected by the ECM. Hence in this case, to find the deception of track-i, all the tracks are compensated except i^{th} track. Therefore, the sequential fusion runs for $N-1$ tracks.

35

Algorithm 2 Sequential update algorithm

1: inputs:$\{\hat{\mathbf{x}}^j(k|k), \mathbf{P}^j(k|k)\}_{j=1}^{N-1}$
2: At time k
3: **Compute** $\hat{\mathbf{x}}_f(k+1|k)$ and $\hat{\mathbf{P}}_f(k+1|k)$ using

$$\hat{\mathbf{x}}_f(k+1|k) = \mathbf{F}\hat{\mathbf{x}}_f(k|k)$$

$$\hat{\mathbf{P}}_f(k+1|k) = \mathbf{F}\hat{\mathbf{P}}_f(k|k)\mathbf{F}^T + \mathbf{Q}_x$$

4: **Initialize**

$$\hat{\mathbf{x}}^0(k+1|k+1) \triangleq \hat{\mathbf{x}}_f^j(k+1|k)$$

$$\mathbf{P}^0(k+1|k+1) \triangleq \mathbf{P}_f^j(k+1|k)$$

5: **for** j=1:N-1 **do**
6:     The state update is given by,

$$\hat{\mathbf{x}}^j(k+1|k+1) = \hat{\mathbf{x}}^{j-1}(k+1|k+1) + \mathbf{W}^j(k)\mathbf{x}^j(k+1)$$
$$-\mathbf{H}^j(k+1)\hat{\mathbf{x}}^{j-1}(k+1|k+1)$$

7:     The gain is given by,

$$\mathbf{W}^j(k+1) = \mathbf{P}^{j-1}(k+1|k+1)\mathbf{H}^j(k+1)^T[\mathbf{H}^j(k+1)$$
$$\mathbf{P}^{j-1}(k+1|k+1)\mathbf{H}^j(k+1)^T + \mathbf{R}_z^j(k+1)]^{-1}$$

8:     The covariance is given by,

$$\mathbf{P}^j(k+1|k+1) = \mathbf{P}^{j-1}(k+1|k+1) - \mathbf{W}^j(k+1)$$
$$\mathbf{S}^j(k+1)\mathbf{W}^j(k+1)^T$$

9: **end for**
10: The final updated state estimate and covariance values are

$$\hat{\mathbf{x}}_f(k+1|k+1) = \hat{\mathbf{x}}^{N-1}(k+1|k+1)$$
$$\mathbf{P}_f(k+1|k+1) = \mathbf{P}^{N-1}(k+1|k+1)$$

3.4.3 Constructing the Reference Measurement

The goal is to create reference measurement by fusing $N-1$ tracks, which are compensated by the previously estimated deception parameters. The sequential update algorithm is performed in the fusion step. Although it is not an optimal approach for fusing the local tracks, it is computationally inexpensive than the parallel update method (Bar-Shalom et al. 2011). In addition, it is independent of previous equivalent measurements at time instant k. Therefore, the index for sequential fusion is $j = 1, \ldots . N - 1/i$. This means j runs for all tracks rather than affected track i. After calculating the equivalent measurements for all the $(N-1)$ local tracks, we get $\{\mathbf{u}(k+1)^j, \mathbf{U}(k+1)^j\}_{j=1}^{N-1}$. This tracklet computation uses Algorithm-1. It is assumed that fused state and covariance at k^{th} instant is available as $\hat{\mathbf{x}}_f(k|k)$ and $\hat{\mathbf{P}}_f(k|k)$ respectively. The sequential update algorithm is presented in Algorithm-2. In the algorithm, all $N-1$ local tracks are sequentially updated to provide $\mathbf{x}_f(k+1|k+1)$ and $\mathbf{P}_f(k+1|k+1)$. One of the advantages of this sequential fusion approach is that in each "for loop" (step-5 in Algorithm-2), only a low dimensional Kalman filter that is independent of the size of the stacked RGPO vector and the number of the sensors is needed. Furthermore, the fusion of local tracks can be accomplished by adding one sequential update for the latest corrected measurement of sensor j to the previously fused track. In the sequential fusion algorithm, it is also important to note that there is no constraint on the rate at which local tracks are being received from the individual sensors. Further, the sequential fusion approach avoids measurement augmentation for updating the estimates step by step by using the current sensor measurement data.

3.4.4 Deception Parameter Estimation Algorithm

The algorithm for estimating the deception parameter is presented in Algorithm-3. Also, the block diagram representation of deception parameter estimation is shown in Fig. 3.4.

Algorithm 3 Deception parameter estimation algorithm

1: **for** $i = 1 : N$ **do**
2:     **Recreate measurements:** The tracklets for the deceived track are computed and then recreate the measurements corresponding to local tracks-i using (45),we obtain $\mathbf{y}^i$ as

$$\mathbf{y}^i(k+1) = \mathbf{W}^i(k+1)^{-1}[\hat{\mathbf{x}}^i(k+1|k+1)- $$
$$(I - \mathbf{W}^i(k+1)\mathbf{H}(k+1))\mathbf{F}^T\hat{\mathbf{x}}^i(k|k)]$$

3:     **Fused state and covariance:** Compute the tracklets for $N-1$ tracks using Algorithm-1 and compensate them using Subsection-3.4.2. For the compensated tracks, perform sequential update using Algorithm-2, to get fused state $\hat{\mathbf{x}}_f(k+1|k+1)$ and fused covariance $\hat{\mathbf{P}}_f(k+1|k+1)$.
4:     **Fused measurement covariance:**

$$\mathbf{R}_f(k+1) = \mathbf{H}(k+1)\left[\sum_{j=1}^{N-1}(\mathbf{U}^j(k+1,k))^{-1}\right]^{-1}$$
$$\mathbf{H}(k+1)^T$$

5:     Calculate the fused weight as

$$\mathbf{W}_f(k+1) = \mathbf{P}_f(k+1|k)\mathbf{H}(k+1)^T[\mathbf{H}(k+1)$$
$$\mathbf{P}_f(k+1|k)\mathbf{H}(k+1)^T + \mathbf{R}_f(k+1)]^{-1}.$$

6:     **Reference measurement** Therefore, by providing the fused covariance in (3.44), we get $\mathbf{y}^{i*}$ as

$$\mathbf{y}^{i*}(k+1) = \mathbf{W}_{fk}(k+1)^{-1}[\hat{\mathbf{x}}_f(k+1|k+1)- $$
$$(I - \mathbf{W}_f(k+1)\mathbf{H}(k+1))\mathbf{F}^T\hat{\mathbf{x}}_f(k|k)]$$

7:     **Compute RLSE:** The new measurement using reference measurement and re-created track is

$$\mathbf{y}(k) = \mathbf{y}^i(k) - \mathbf{y}^{i*}(k)$$
$$= \mathbf{H}^i(k)\mathbf{x}^i(k) + \mathbf{B}^i(k)\mathbf{c}^i(k)\Delta r_i(k)+ $$
$$\mathbf{w}^i(k) - \mathbf{H}^{i*}(k)\mathbf{x}^{i*}(k) - \mathbf{w}^{i*}(k)$$
$$= \mathbf{H}(k)\Delta r(k) + \mathbf{w}^i(k) - \mathbf{w}^{i*}(k)$$
$$= \mathbf{H}(k)\Delta r + \tilde{w}(k)$$

    recursively solve using the last updates in recursive least squares estimation (RLSE) framework (Bar-Shalom et al. 2011).
8: **end for**

3.5 Performance evaluation of proposed algorithm

3.5.1 Innovation test

Innovation test is used for testing the efficiency of RLS estimator. The measurement is given by,

$$\mathbf{y}(k) = \mathcal{H}(k)\Delta\mathbf{r}(k) + \tilde{\mathbf{w}}(k) \tag{3.47}$$

where, $\mathcal{H}(k)$ measurement transition matrix and the measurement noise covariance is $\mathbf{R}(k) = \mathbf{R}^i(k) + \mathbf{R}^{i*}(k)$.

The innovation covariance is represented as,

$$\mathbf{S}(k) = \mathcal{H}(K)\Sigma(k)\mathcal{H}(k)^T + \mathbf{R}(k) \tag{3.48}$$

The gain and the residual is calculated as

$$\mathbf{G}(k) = \Sigma(k)\mathcal{H}(k)^T[\mathcal{H}(k)\Sigma(k)\mathcal{H}(k)^T + \mathbf{R}(k)]^{-1} \tag{3.49}$$

$$\Gamma(k) = y(k) - \mathcal{H}(k)\Delta\hat{r}(k) \tag{3.50}$$

The range gate estimate and its covariance are,

$$\Delta\hat{r}^i(k) = \Delta\hat{r}^i(k-1) + \mathbf{G}(k)\Gamma(k) \tag{3.51}$$

$$\Sigma(k) = \Sigma(k-1) - \Sigma(k)\mathbf{H}(k)^T \tag{3.52}$$
$$\cdot [\mathbf{H}(k)\Sigma(k)\mathbf{H}(k)^T + \mathbf{R}(k)]^{-1}$$
$$\cdot \mathbf{H}(k)\Sigma(k)$$

The innovation test (Ivanov et al. 2014) is given as,

$$\Gamma(k)\mathbf{S}(k)^{-1}\Gamma(k) \leq \xi_{n_r}^2(1-q) \tag{3.53}$$

where, $\xi_{n_r}^2(1-q)$ is the chi square value with n_r degree of freedom and tail probability of q.

3.5.2 Cramer Rao Lower Bound

The Cramer Rao Lower Bound (CRLB) on the mean square error of unbiased estimator is a frequently used metric for determining the correctness of parameter estimation based on a set of data (Meir and Routtenberg 2021). The CRLB of the algorithm provides the criterion to know the minimum value of error that the algorithm can achieve.

From the measurement equation of the RLS estimator,

$$\mathbf{y}^i(k) = \mathcal{H}(k)\Delta\mathbf{r}^i(k) + \tilde{\mathbf{w}}_i(k) \tag{3.54}$$

where $\Delta r_i(k)$ is the range gate vector to be estimated and the measurement noise covariance of $\mathbf{w}_i(k)$ is given as $\mathbf{R}_i(k) = \mathbf{R}_i(k) + \mathbf{R}_i^*(k)$ where $\mathbf{R}_i(k)$ is the measurement noise of ith local track and $\mathbf{R}_i^*(k)$ is the measurement noise obtained by fusing rest of the local tracks.

The covariance matrix of an unbiased estimator is bounded as below (Bar-Shalom et al. 2004) and (Van Trees and Bell 2007):

$$\mathbb{E}\left\{(\Delta\hat{\mathbf{r}}_i(k) - \Delta\mathbf{r}_i)(\Delta\hat{\mathbf{r}}_i(k) - \Delta\mathbf{r}_i)'\right\} \geq \mathbf{J}_\mathbf{z}(k)^{-1} \tag{3.55}$$

Here, $\mathbb{E}$ is the estimation operator and $\mathbf{J}_z$ is the Fisher Information Matrix(FIM) and is given as

$$\mathbf{J}_\mathbf{z}(k) = \mathbb{E}\big\{[\nabla \ln p(\mathbf{y}(k) \mid \Delta\mathbf{r}(k))]$$
$$[\nabla \ln p(\bar{y}(k) \mid \Delta\mathbf{r}(k))]'\big\}_{\Delta\mathbf{r}(k)=\Delta\mathbf{r}_t} \tag{3.56}$$

where, Δr_t is the true value of the range gate parameter and ∇ is the gradient operator. Also, $p(\mathbf{y}(k) \mid \Delta r(k))$ is the likelihood function, which is given as below:

$$p(\mathbf{y}(k) \mid \Delta r(k)) = \frac{1}{\sqrt{2\pi|\mathbf{R}(k)|}}\cdot$$
$$\exp\left\{\frac{-1}{2}[\mathbf{y}(k) - \mathcal{H}(k)\Delta r(k)]'\mathbf{R}(k)^{-1}[\mathbf{y}(k) - \mathcal{H}(k)\Delta r(k)]\right\} \tag{3.57}$$

Substituting $\lambda_y = -\ln p(\mathbf{z}(k) \mid \Delta\mathbf{r}(k))$,

$$\lambda_y = \mathrm{C} + \frac{-1}{2}[\mathbf{y}(k) - \mathcal{H}(k)\Delta r(k)]'\mathbf{R}(k)^{-1}[\mathbf{y}(k) - \mathcal{H}(k)\Delta r(k)] \tag{3.58}$$

Upon further simplification,

$$\nabla_{\Delta\mathbf{r}}\lambda_y = \mathcal{H}(k)'\mathbf{R}(k)^{-1}(\mathbf{y}(k) - \mathcal{H}\Delta r(k)) \tag{3.59}$$

which gives,

$$\mathbf{J}_z(k) = \mathcal{H}(k)'\mathbf{R}(k)^{-1}\mathcal{H}(k) \tag{3.60}$$

The FIM at K is also the recursive form of CRLB is represented as,

$$\mathbf{J}_z(K) = \sum_{k=1}^{K} \mathbf{J}_z(k) \tag{3.61}$$

3.5.3 NEES test and Confidence Interval test

In simulation frameworks, the normalised estimation error squared (NEES) test can be used to determine if the estimator is efficient, that is, whether the error matches the covariance provided by the CRLB (Govaers et al. 2013). The error matrix provided by the CRLB is J_z. For an estimated deception parameter $\Delta\hat{r}(k)$, there exist a ground truth $r(k)$. The estimation error is given by,

$$\Delta\tilde{r}(k) = \Delta r(k) - \Delta\hat{r}(k) \tag{3.62}$$

The NEES value for the parameter Δr is written as,

$$\Delta\tilde{r}^T(k)\mathbf{J}_z(k)\Delta\tilde{r}(k) \leq \xi_{n_r}^2(1-q) \tag{3.63}$$

The confidence interval of a deception parameter is evaluated for $\Delta r(k)$. The squared norm of the error should be constrained by the estimate if the estimator is efficient (Chi et al. 2006).

The confidence for the parameter $\Delta r(k)$ is,

$$\Delta\tilde{r}^T(k)\Sigma^{-1}(k)\Delta\tilde{r}(k) \leq \xi_{n_r}^2(1-q) \tag{3.64}$$

which follows chi square distribution with degree of freedom equal to n_r.

3.6 Results

3.6.1 Case-1: Single radar sensor deceived by RGPO ECM

In this scenario, among the three radars in the surveillance area, consider that a single radar sensor is deceived by RGPO ECM. All the radars are static and synchronous in time with $t_s = 1$s. The radars are located at r^s and θ^s with reference to the origin. The range and azimuth measurements are corrupted with the noise with a standard

deviation of σ_r and σ_θ, respectively. In the surveillance region, a single target is considered, and all radars have a local tracker to provide local estimates about the target. In this simulation, a single jammer influences the single radar equipped with local tracker-1. Since the local track-1 generated from the tracker-1 is deceived with the RGPO ECM measurements, this results in a range displacement of Δr_1. The positions, measurement standard deviation, and deception parameters are tabulated in the Table 3.1. Moreover, the scenario is depicted in Fig. 3.5. The target is located at a range of 3000m and the azimuth of 1.5 rad from the origin. The target moves with a speed of 40m/s, and 80deg heading throughout the simulation time of 1000s. The target follows a constant velocity model, and the state transition matrix is represented as,

$$
F = \begin{bmatrix} 1 & t_s & 0 & 0 \\ 0 & 1 & 0 & 0 \\ 0 & 0 & 1 & t_s \\ 0 & 0 & 0 & 1 \end{bmatrix}.
$$
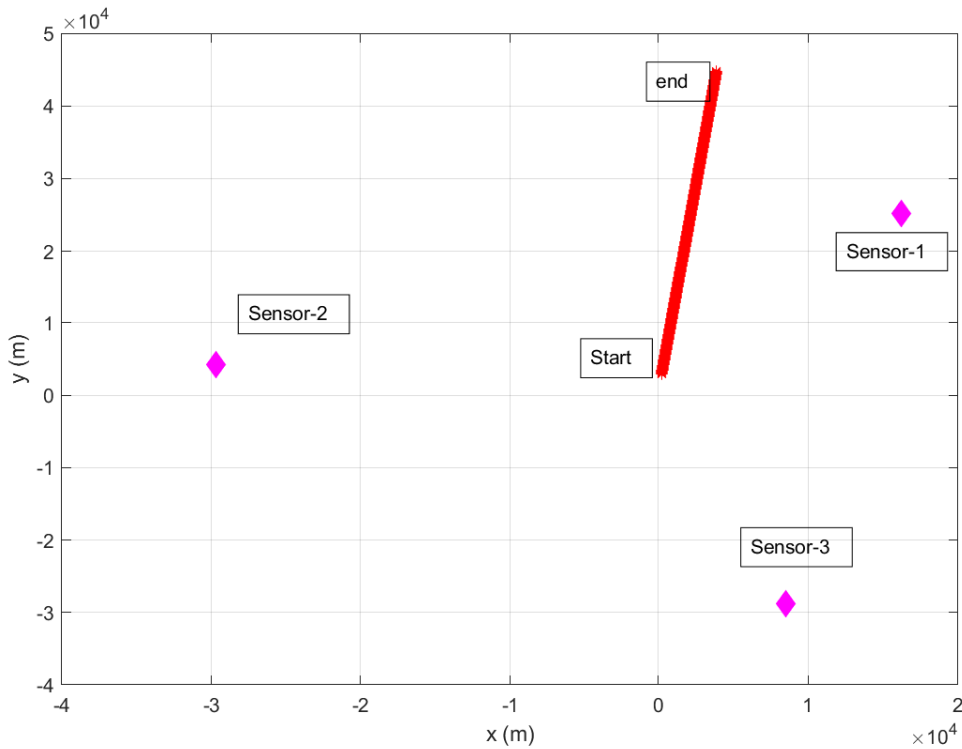
Figure 3.5: Scenario of the static radars and target.

Table 3.1: Radar parameters for single radar jamming case

	Sensor-1	Sensor-2	Sensor-3
Range (r^s in m)	30000	30000	30000
Azimuth (θ^s in rad)	1	3	5
Std of range (σ_r in m)	20	20	20
Std of azimuth (σ_θ in rad)	1m	1m	1m
Sampling time (t_s in s)	1	1	1
Deception (Δr in m)	1000	-	-

A   Tracking Accuracy

A Global Nearest Neighbor (GNN) association based extended Kalman filter (EKF) filter is used for target tracking. Two-point initialization method (Mallick and SCALA 2008) is used to initialize the filter. The range-azimuth measurements $r(0)$ and $\theta(0)$ at zero instant are considered to form the converted measurements as $x(0)$ and $y(0)$. Similarly, the first instant measurements are used to form the converted measurements as $x(1)$ and $y(1)$. Hence, the two-point initialization is given by,

$$\mathbf{x} = \begin{bmatrix} x(1) & \frac{x(1)-x(0)}{t_s} & y(1) & \frac{y(1)-y(0)}{t_s} \end{bmatrix}$$

The measurement conversion follows the unbiased conversion by using,

$$x(1) = \lambda^{-1} r(1) \cos(\theta(1))$$
$$y(1) = \lambda^{-1} r(1) \sin(\theta(1))$$

Here $\lambda = \exp\left(-\frac{\sigma_\theta^2}{2}\right)$. This unbiased conversion is valid for initialization, since it follows the necessary criteria of $\frac{r\sigma_\theta^2}{\sigma_r} \ll 0.4$. The covariance is initialized using,

$$P(1 \mid 1) = \begin{bmatrix} R_{xx}(1) & \frac{R_{xx}(1)}{t_s} & 0 & 0 \\ \frac{R_{xx}(1)}{t_s} & \frac{2R_{xx}(1)}{t_s^2} & 0 & 0 \\ 0 & 0 & R_{yy}(1) & \frac{R_{yy}(1)}{t_s} \\ 0 & 0 & \frac{R_{yy}(1)}{t_s} & \frac{2R_{yy}(1)}{t_s^2} \end{bmatrix}$$

where,

$$R_{xx} = \left(\lambda^{-2} - 2\right) \left(r(1)\right)^2 \cos^2(\theta(1)) + \frac{\left((r(1))^2 + \sigma_r^2\right)}{2} \left(1 + \lambda^4 \cos 2\theta(1)\right)$$

43

$$R_{yy} = \left(\lambda^{-2} - 2\right)\left(r(1)\right)^2 \sin^2(\theta(1))$$
$$+ \frac{\left((r(1))^2 + \sigma_r^2\right)}{2}\left(1 - \lambda^4 \cos 2\theta(1)\right)$$

The tracking is carried out with the aid of an EKF. The tunable parameters such as process noise covariance (Q_x) and measurement noise covariance (R_z) are represented as,

$$Q_x = 0.08 \begin{bmatrix} \frac{1}{3} * (t_s^3) & \frac{1}{2} * (t_s^2) & 0 & 0 \\ \frac{1}{2} * (t_s^2) & t_s & 0 & 0 \\ 0 & 0 & \frac{1}{3} * (t_s^3) & \frac{1}{2} * (t_s^2) \\ 0 & 0 & \frac{1}{2} * (t_s^2) & t_s \end{bmatrix}$$

and

$$R_z = \begin{bmatrix} R_{xx} & R_{xy} \\ R_{yx} & R_{yy} \end{bmatrix}$$

where,

$$R_{xy} = R_{yx} = \left[\frac{\lambda^{-2}(r)^2}{2} + \frac{((r)^2 + \sigma_r^2)\lambda^4}{2} - ((r)^2)\right]\sin 2\theta.$$

The tracking performance is evaluated using the position root mean square error (PRMSE). The tracking performance of all the local trackers is depicted in Figs. 3.6(a)-(c).

It can be observed from Fig. 3.6(a) that the local track-1 PRMSE is approximately around 1000 ± 8m because of the range deception of 1000m affected by the RGPO ECM jamming. Moreover, the PRMSE of the local track-2 and local track-3 are also depicted in the Fig. 3.6(b) and Fig. 3.6(c). The PRMSE of local track-2 and local track-3 is lesser compared to local track-1 since the RGPO jamming is un-influencing local track-2 and local track-3. This tracking performance can be directly reflected in the fusion module.

B Tracking performance after Sequential Fusion

The sequential fusion is performed on the compensated equivalent measurements. The correction is applied at k in the polar coordinates by adopting the estimated deception parameter at $k - 1$ time instant. For the time stamp of $k = 1$, since there are no previously fused estimates are available, the local track's updated state is considered as the fused state estimate i.e., $\mathbf{x}_f(k|k) = \mathbf{x}(k|k)$ and $\mathbf{P}_f(k|k) = \mathbf{P}(k|k)$ at $k = 1$. It is evident from the Figs. 3.6 (d)-(f) that, the PRMSE of local track-1 fused estimate

is equal to the PRMSE of local track-1 for the initial scan. After that, the deception parameter estimation converges over time and improves the PRMSE of the sequential fusion block. Therefore, we observed that, the local track-1 fusion PRMSE decreases over time, and the similar procedure holds true for local track-2 and local track-3 performance. Since the deception parameter is kept at 1000m for local track-1, the sequential fusion PRMSE starts at 1000m and finally diminishes to 10m accuracy. The sequential fusion provides sub-optimal solution, but it is a significant technique importance due to its reduced computational requirement. It is also worth noting that the sequential fusion is only dependent on the compensated equivalent measurements to compute the fused state and covariance estimates at a given scan.

| (a) Sensor-1 | (b) Sensor-2 | (c) Sensor-3 |

| (d) Sensor-1 | (e) Sensor-2 | (f) Sensor-3 |

Figure 3.6: (a-c) Target Tracking performance of the individual radar sensor before the proposed algorithm, (d-f) Target tracking performance after Sequential fusion

C Deception Parameter Evaluation

The deception parameter is calculated in the RLSE framework. In this framework, measurement i corresponds to the deceived local track i. whereas, the reference measurement is generated by the compensation and fusion of all local tracks except i. That is the sequential fusion block runs for $i^* \in 1, \cdots N/i$. The initial state and covariance of the RLSE is $\Delta r(0|0) = 0$ and $\Sigma(0|0) = 1000^2$. There is no prior infor-

mation regarding the deception parameter and its associated covariance at $k = 0$. The deception parameter of the deceived local track-1 is estimated, and its corresponding PRMSE is plotted in Fig. 3.7.
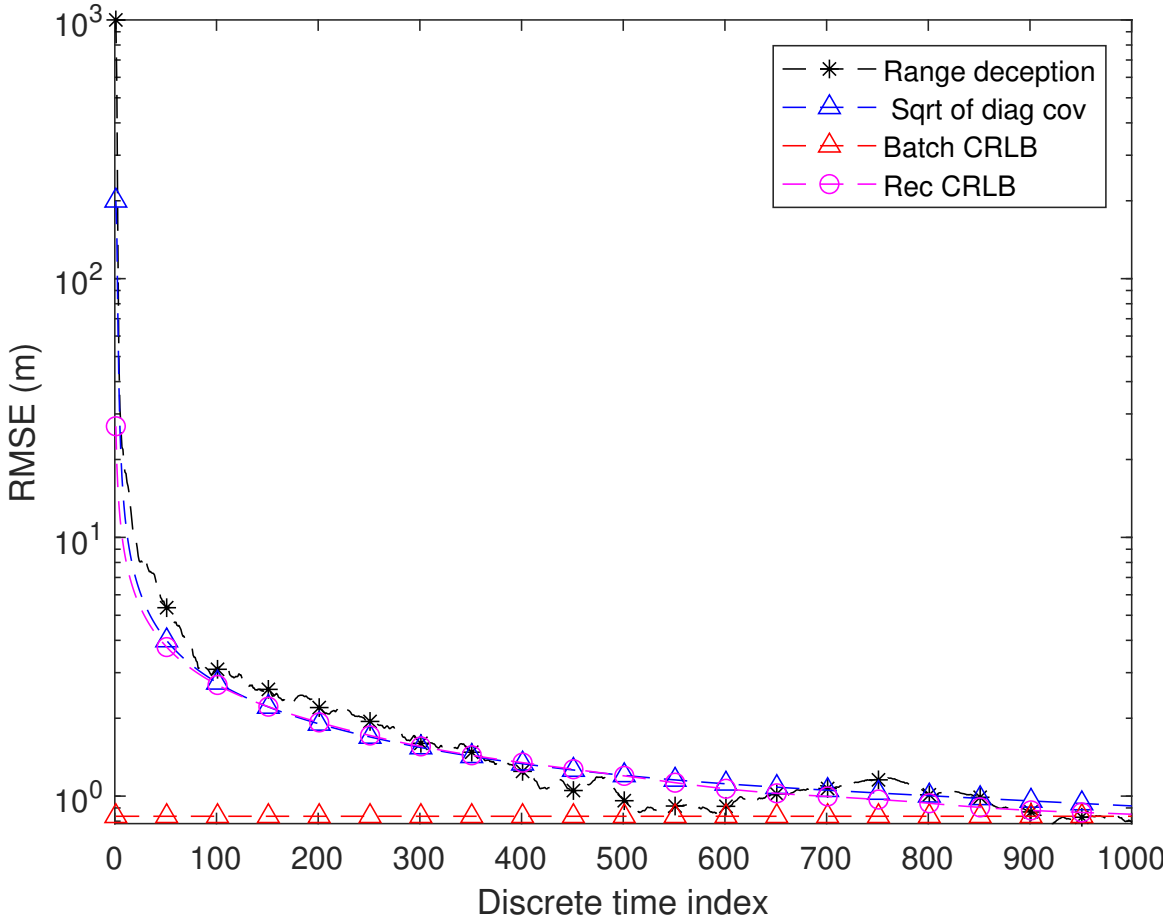
Figure 3.7: Deception parameter of local track-1.

Initially, the deception is considered as zero, and hence PRMSE at initial state is equal to 1000m which is the deception created by the RGPO ECM. Along with the estimated deception parameter, we also plotted the Batch CRLB ($\sqrt{B - CRLB}$), Recursive CRLB ($\sqrt{R - CRLB}$) and the diagonal of the covariance estimate ($\sqrt{\Sigma}$). From Fig. 3.7, it can be observed that the estimator is working effectively, and the estimated deception parameter is coming closer the CRLB value. We have plotted on logy scale for better visualization, keeping the deception parameter changing from 10^3 to unity.

D Performance evaluation of the proposed algorithm

The performance of the proposed algorithm is validated using the NEES test, innovation test, and confidence interval test. In all three tests chi-square distribution as $\chi_b^2(1-q)$ where q is tail probability is considered. The q is taken as 1% and 5% and is plotted in the Fig. 3.8. It is evident from the results that the NEES values are falling within the chi-square distribution with a tail probability of 5% which infers that the proposed estimator is efficient. The NEES for the estimator along with the chi-square distribution is shown in Fig. 3.8(a). Further, it can be observed from Fig. 3.8(b) that the innovation test is inbound with the Raleigh distribution, and it is falling within the 95% confidence interval of the chi-square distribution with a degrees of freedom equal to two. Further, the confidence area of the parameter to associated confidence interval, which intuitively specifies whether the estimated parameter is examined and the estimated parameter covariance are agreeing with each other. From Fig. 3.8(c) it is evident that the confidence region of the estimated parameter is well within the specified range which indicates that the estimated covariance and R-CRLB are almost equal. Hence, one can state that the proposed estimator neither optimistic nor pessimistic.

| (a) NEES Test | (b) Innovation Test | (c) Confidence Interval Test |
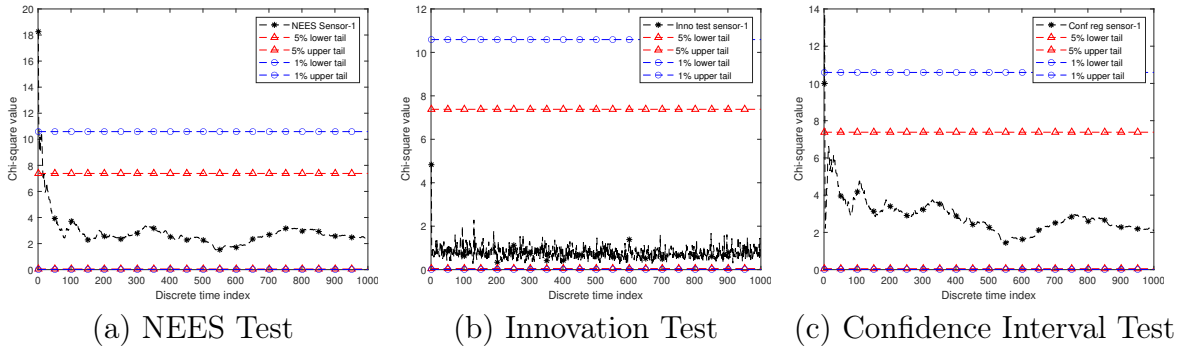
Figure 3.8: Performance evaluation of the proposed deception parameter estimation algorithm for radar sensor-1 deceived by RGPO ECM scenario

3.6.2   Case-2: Multiple radar sensors affected by Jamming

In this scenario, we considered three radars present in the surveillance region and all are affected by RGPO ECM. All the three radars are assumed to be static and synchronous in time. The radars are located at r_i^s and θ^s with respect to origin.

Table 3.2: Sensor parameters for multiple sensor jamming case

	Sensor-1	Sensor-2	Sensor-3
Range (r_i^s in m)	30000	30000	30000
Azimuth (θ_i^s in rad)	1	3	5
Std of range (σ_{r_i} in m)	50	100	150
Std of azimuth (σ_{θ_i} in rad)	1m	2m	3m
Sampling time (t_s in s)	1	1	1
Deception (Δr_i in m)	1000	1500	2000

The range and azimuth measurements are corrupted with white Gaussian noise with zero mean and standard deviations of σ_{r_i} and σ_{θ_i} respectively. A single target is considered, and all local trackers provide updated state and covariance to the fusion center. Unlike the single jammer three jammers are considered, and this yields a range displacement of Δr_i to each local track. The locations, standard deviation of measurements, and deception parameters of each of the local track are tabulated in Table 3.2.

A Tracking Accuracy

A two-point initialization method is utilized to initialize the filter, and the EKF is used to filter the measurements. The tracking PRMSE of all the three local tracks is depicted in Figs. 3.9(a)-(c). Since all the three local tracks are deceived by the RGPO ECM, it can be observed that the local track-1 PRMSE is around 1000m; this is as a result of range deception parameter of 1000m affected the local track. Similarly, the PRMSE of local track-2 and local track-3 are 1500m and 2000m, respectively. Corresponding to the range deception, since all the tracks are deceived, this results in hypothesis $H1$ in T2TA. Meaning that the T2TA model reports that all the tracks are of separate origin, despite all the tracks belonging to the same origin.

B Tracking performance after Sequential Fusion

Each track is compensated with the estimated range deception parameter Δr_i, and then the sequential fusion is performed. Similar to the single jammer case, the initialization of the fused track is performed by using local tracks i.e, $\mathbf{x}_f(k|k) = \mathbf{x}(k|k)$ and

(a) Sensor-1   (b) Sensor-2   (c) Sensor-3
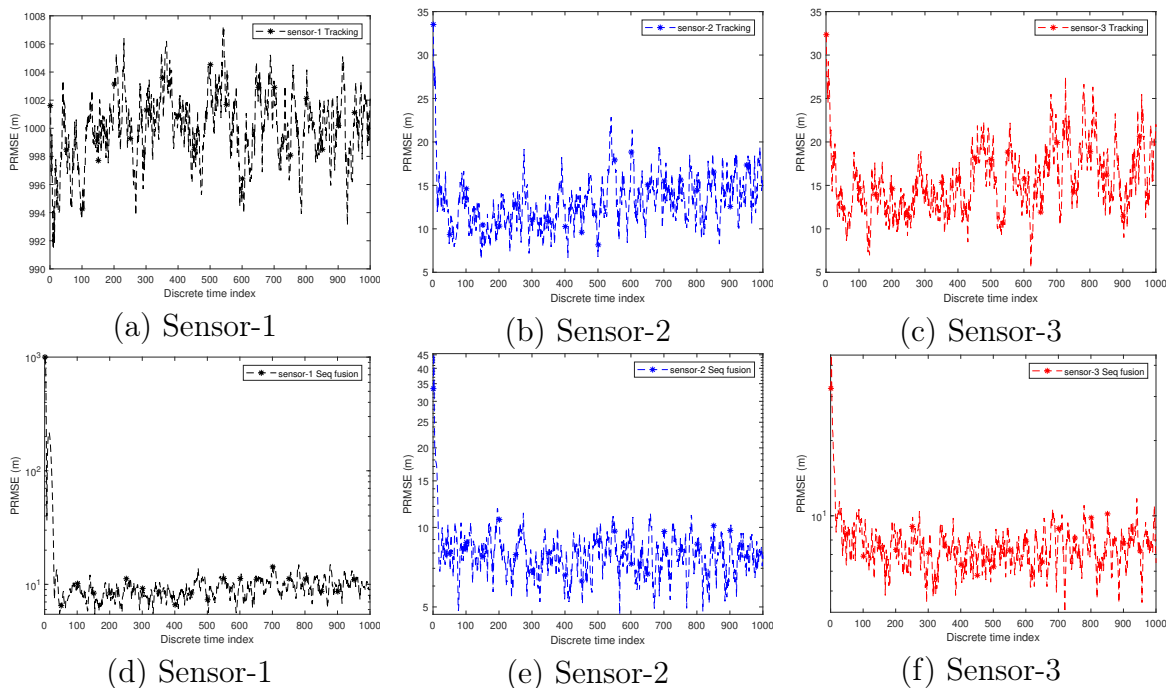
(d) Sensor-1   (e) Sensor-2   (f) Sensor-3
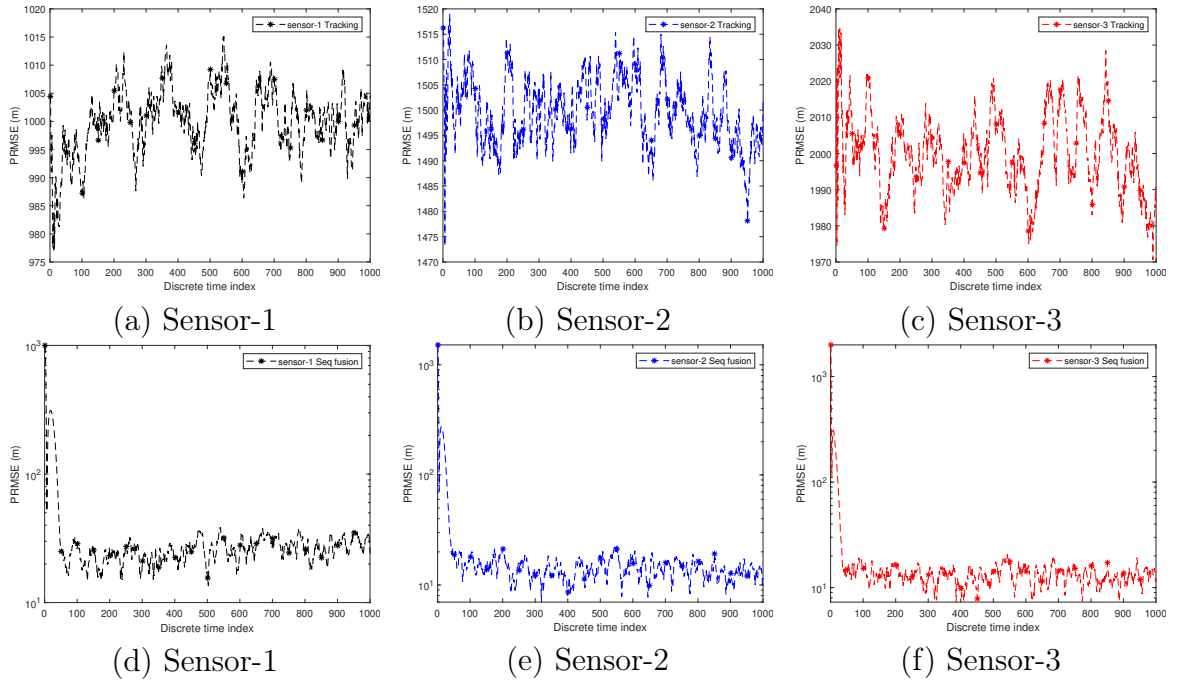
Figure 3.9: (a-c) Target Tracking performance of deceived radar sensors before proposed algorithm, (d-f) Target Tracking Performance after Sequential fusion

$\mathbf{P}_f(k|k) = \mathbf{P}(k|k)$ at $k = 1$. It can be seen from Figs. 3.9(d)-(f) that, for all the local tracks fused estimate is equal to the tracking PRMSE of the initial scan at $k = 1$. Similar to the single jammer case, we observed that all the local track's fusion PRMSE decreases over time. This indicates that, the deception parameter compensation followed by sequential fusion brings all the fused tracks together. Since the deception parameter is 1000m for local track-1, 1500m for local track-2, and 2000m for local track-3, the sequential fusion PRMSE starts around the same value and finally reduces to minimum value. Henceforth, one can visualize that the local tracks converges to a single track over time, after performing the deception parameter compensation.

C Deception Parameter Evaluation

The deception parameter of all the local tracks is estimated, and its corresponding PRMSE is plotted in Fig. 3.10. Initially, the deception parameter is zero, and hence PRMSE at $k = 1$ is higher and equal to the value of the deception parameter. Along with the estimated deception parameter, the $\sqrt{B - CRLB}$, $\sqrt{R - CRLB}$ and $\sqrt{\Sigma}$ are plotted. Here, it can be observed that the estimator is working effectively, and the estimated deception is approaching closer to the CRLB value.

(a) Sensor-1 (b) Sensor-2 (c) Sensor-3
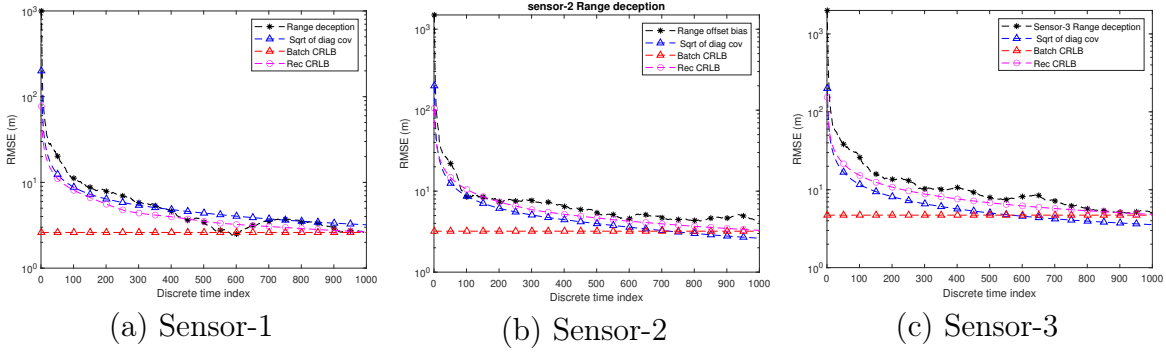
Figure 3.10: Range deception parameters evaluation in multiple jammers scenario

D   Estimator Performance Evaluation

To evaluate the performance of the estimator the similar tests are conducted as that of single sensor RGPO ECM case. Figs. 3.11(a)–(c) provide the plots corresponding to the innovation test, whereas Figs. 3.11(d)–(f) depicts the NEES test, and finally Figs. 3.11(g)–(i) shows the plots corresponding to the confidence interval test. From the plots, it is evident that the value of the estimated parameter falls within chi-square distribution of 5% tail probability which indicates the correctness of the proposed algorithm.

Overall, this work presents a deception parameter estimation algorithm to combat RGPO ECM in a networked radar scenario. The RGPO ECM is detected, and the range gate deception parameter is estimated for the deceived local track. A track-to-track association is formulated at the fusion node to detect the deceived tracks using all the available local tracks. Once the attack is detected, the weight matrix, pseudo-measurement, and pseudo-measurement covariance at the fusion center are recreated by utilizing the tracklet framework. Moreover, all the local tracks except deceived tracks are compensated and sequentially fused to create a reference measurement. The deception parameter of the deceived track is estimated by deploying a recursive least squares framework with the help of the pseudo-measurement and reference measurement. Further, the proposed algorithm was analyzed for single and multiple RGPO ECM scenarios and is validated by using tracker accuracy, fusion accuracy, and estimator accuracy. Besides, the estimated deception parameter is in agreement with the achievable CRLB. Furthermore, the results are quantified with a Position Root Mean Square Error (PRMSE), CRLB, innovation test, NEES test, and confidence interval. In addition, the simulation results demonstrate that the proposed estimator

50

Figure 3.11: (a–c) Innovation test, (d–f) NEES test, and (g–i) Confidence interval test for multiple local trackers deceived by RGPO ECM scenario

efficiency is below the 5% tail probability of the chi-square distribution. Moreover, it is evident from the results that the proposed technique is efficient for both single and multiple RGPO ECM cases.

3.7 Conclusion

Chapter 3 dealt with proposing an efficient ECCM approach to combat RGPO ECM in a networked radar system. This approach can further be extended and can be incorporated in passive radar systems. The next chapter (Chapter 4) focuses on evaluating the feasibility of 5G NR waveform as a suitable IOO for passive radar system. In addition, Chapter 4 also proposes a conceptual framework to improve the strength of the received signal at passive radar receiver.

Chapter 4

Feasibility study of 5G NR waveform as an IOO and RSS improvement

4.1 Preamble

Passive radars utilize the IOO signals available in the surveillance environment for target detection and tracking. The working and accuracy of target detection mainly rely on the availability of good quality IOO. Also, specific IOO signals suites relevant applications based on the signal features. The selected IOO signal must give good range and velocity resolution for detecting multiple and slow-moving targets. Accordingly, in this objective, the feasibility of adopting a 5G NR waveform as an IOO for passive radar is carried out. Further, the propagation environment affects the IOO signals, which lowers the received signal strength at the passive radar. In this context, a simple and effective approach to opt for an appropriate IOO based on application and improving the signal strength at the receiver is proposed.

4.2 5G NR Waveform

The continuous-time OFDM signal is represented as,

$$x_i(t) = \frac{1}{N} \sum_{k=0}^{N-1} a_{k,i} \exp\left(\frac{j2\pi kt}{T}\right),$$

(4.1)

and the discrete baseband OFDM signal as,

$$b_{n,i} = \frac{1}{N} \sum_{k=0}^{N-1} a_{k,i} \exp\left(\frac{j\pi kn}{N}\right), \ 0 \le n \le N-1,$$

(4.2)

where $a_{0,i}, \cdots, a_{N-1,i}$ are a vector of modulated symbols which modulates N subcarriers in i-th symbol period. The time-domain representation and the spectrum of the

Cyclic Prefix – Orthogonal Frequency Division Multiplexing (CP-OFDM) waveform used for the 5G NR waveform as per the FR1 specifications are shown in Fig. 4.1(a) and Fig. 4.1(b) respectively.

(a) Time domain signal

(b) Spectrum of the signal
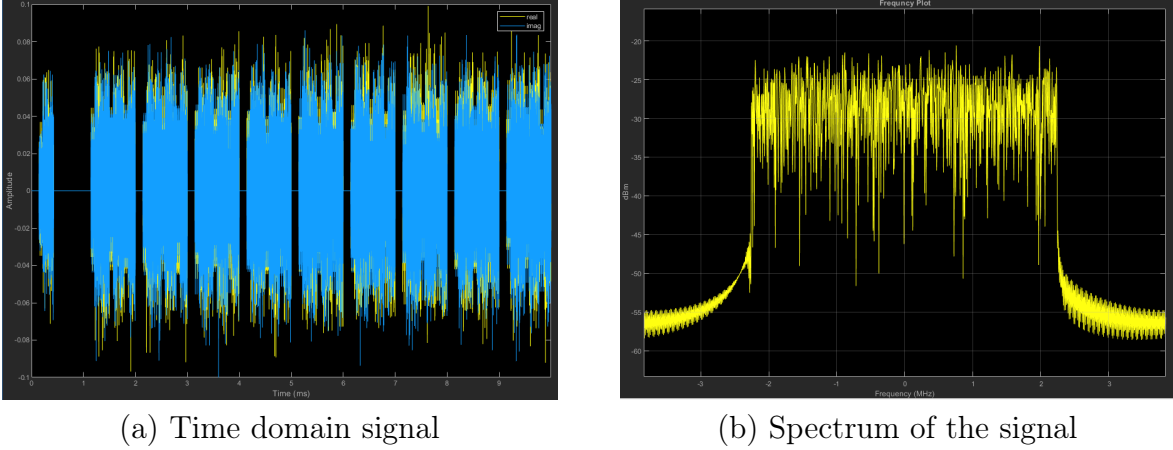
Figure 4.1: The CP-OFDM signal in time domain and its spectrum

The power spectrum of the OFDM signal $S_x(f)$ is,

$$S_x(f) = E\left\{|a|^2\right\} \sum_{k=0}^{N-1} \frac{|X_k(f)^2|}{T},$$

(4.3)

where $\frac{|X_k(f)^2|}{T}$ is the power spectrum of kth subcarrier.

Further, for the 5G NR waveform, the FR1 specifications are the bandwidth per carrier varies from 5MHz to 50MHz with a subcarrier spacing of 15KHz. The maximum number of carriers considered is 3300 with 4096 point Discrete Fourier Transform (DFT). The Quadrature Phase Shift Keying (QPSK) modulation is considered with a radio frame length of 10ms. For these specifications, the bistatic radar parameters like SNR, range resolution, velocity resolution, and other radar basic parameters are calculated and analyzed.

4.3 Bistatic Radar Parameters

4.3.1 Bi-static geometry

The Fig. 4.2 shows the two-dimensional view of the bi-static geometry of passive radar system. The transmitter (Tx) and receiver (Rx) are located at $\mathbf{x}^{Tx}$ and $\mathbf{x}^{Rx}$ respectively. The line between Tx and Rx is denoted by $\rho = |\mathbf{x}^{Tx} - \mathbf{x}^{Rx}|$. The

target is located at $\mathbf{x}^t$ in the same space. The range between transmitter-to-target is $\rho_t = |\mathbf{x}^{Tx} - \mathbf{x}^t|$. Similarly, the range between target-to-receiver is $\rho_r = |\mathbf{x}^t - \mathbf{x}^{Rx}|$.
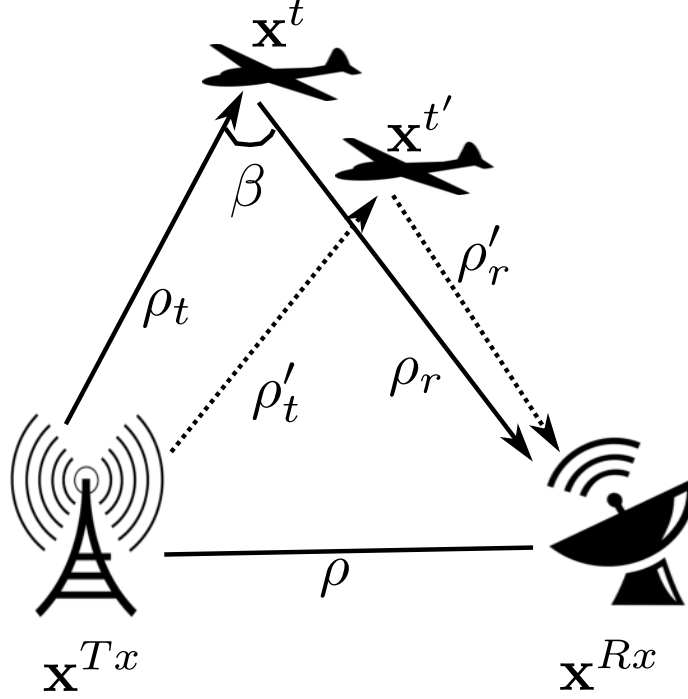
Figure 4.2: Bi-static geometry indicating the IOO waveform transmitter (Tx) located at X^{Tx}, Passive Radar Receiver (Rx) located at X^{Rx} and time-varying dynamic targets present at X^t & $X^{t'}$ in 2D Cartesian coordinate system.

The angle between the Tx and Rx denoted by β

$$\beta = \sin^{-1} \left(\frac{\rho \cos \theta_r}{\rho_t} \right), \tag{4.4}$$

where θ_r is the angle sustained by the receiver, IOO is transmitting the 5G NR waveform with wavelength (λ_x), and bandwidth (B). The illuminated signal is used to get the detections from the target. In Fig. 4.2, another target-2 is considered, and ranges are depicted with dotted lines to distinguish target-1 and target-2. Corresponding to target-2, the ranges are ρ_t' and ρ_r' for transmitter-to-target and target-to-receiver respectively. The motive to consider the second target in the vicinity for the given scenario is to verify the range resolution using 5G NR waveform.

55

4.3.2 Maximum Range

The bi-static maximum range (Kuschel et al. 2019b) is given by,

$$(\rho_t \rho_r)_{\max} = \left[\frac{P_t G_t G_r \lambda_x^2 \sigma F_t^2 F_r^2}{(4\pi)^3 k T_r B_n \left(\frac{S}{N}\right) L_t L_r} \right]^{\frac{1}{2}},$$
(4.5)

where P_t is transmitted power, G_t is transmitting antenna gain, G_r is receiving antenna gain, σ is radar cross section, F_t is transmitter-to-target pattern propagation factor, F_r is target-to-receiver pattern propagation factor, k is Boltzmann's constant, T_r is Rx noise temperature, B_n is Rx noise bandwidth, $\left(\frac{S}{N}\right)$ is minimum SNR, L_t is losses corresponding to Tx, and L_r term corresponds to losses of receiving system. Here, $(\rho_t \rho_r)_{\max}$ is bi-static maximum range product. This term is analogous to R^4 in mono-static systems (Kuschel et al. 2019b).

4.3.3 Bistatic Range resolution

The bistatic radar's range resolution is defined as the minimal distance necessary between two independent targets in order to detect them as two targets. The radar can identify them apart by analyzing the corresponding returns. The range resolution is measured in meters. The range resolution $\Delta\rho$ is given by (Kuschel et al. 2019b),

$$\Delta\rho = \frac{c}{2B \cos\left(\frac{\beta}{2}\right)},$$
(4.6)

where c is a speed of light, B is the processed transmitted signal bandwidth and, β is the bistatic angle formed at the target due to transmitter and receiver.

4.3.4 Bistatic Doppler

The Bistatic Doppler is defined as the bistatic range rate over time normalized by the carrier wavelength λ_x (Teo). That is

$$
\begin{aligned}
f_b &= \frac{1}{\lambda_x} \left[\frac{\partial \rho_b}{\partial t} \right] \\
&= \frac{1}{\lambda_x} \left[\frac{\partial \rho_t(t)}{\partial t} + \frac{\partial \rho_t(t)}{\partial t} \right].
\end{aligned}
$$
(4.7)

In the above equation, the bistatic Doppler comprises two contributions. The first one is the relative radial motion between transmitter-to-target, and the other is the relative motion between target-to-receiver. However, in the majority of the cases in

passive radar, both Tx and Rx are stationary, and Doppler depends on the target motion. The final Doppler frequency (Kuschel et al. 2019b) is represented as,

$$f_b = \frac{2V}{\lambda_x} \cos \alpha \cos \left(\frac{\beta}{2} \right),$$

<div align="right">(4.8)</div>

where V is the modulus of the target velocity vector, α is the orientation of V concerning bistatic angle and, β is the bistatic angle.

4.3.5 Doppler Resolution

The Doppler Resolution indicates the ability of the radar to distinguish between two closely moving targets and associated Dopplers, it depends on coherence integration time (NT) as given by,

$$\Delta f_d = \frac{1}{NT}.$$

<div align="right">(4.9)</div>

where N is the number of pulses integrated and T is the pulse repetition interval of the waveform.

4.3.6 Velocity Resolution

The velocity resolution indicates the ability of the radar to distinguish between two targets moving with different velocities, it depends on coherence integration time (NT) (Richards 2014), wavelength and, bistatic angle as given by,

$$\Delta v = \frac{\lambda}{2NT \cos \left(\frac{\beta}{2} \right)}.$$

<div align="right">(4.10)</div>

4.3.7 Maximum unambiguous PRF

The maximum unambiguous PRF is given by,

$$(PRF)_u = \frac{c}{\sqrt{\rho^2 + 2\zeta(1 + \cos \beta)}}.$$

<div align="right">(4.11)</div>

4.3.8 Ovals of cassini

Oval of cassini is defined as the locus of points whose product of distance from fixed point is constant. In Eqn. 4.5, substituting $\zeta = (\rho_t \rho_r)_{\max}$ and keeping $K =$

$\left[\frac{P_t G_t G_r \lambda_x^2 \sigma F_t^2 F_r^2}{(4\pi)^3 k T_r B_n L_t L_r} \right]$ as a constant yields to

$$K = \zeta^2 \left(\frac{S}{N} \right). \tag{4.12}$$
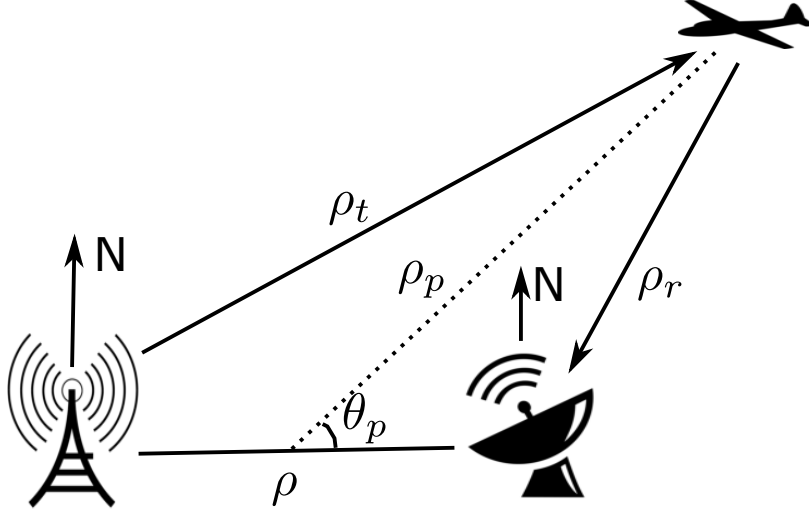
Figure 4.3: Passive bistatic radar geometry in polar coordinates (N indicates the earths north).

On solving the above equations by transforming the geometry into polar coordinates as given in Fig. 4.3, the final signal to noise ratio derived as given in (Kuschel et al. 2019b) results to

$$\frac{S}{N} = \frac{K}{\left(\rho_p^2 + \frac{\rho^2}{4} \right) - \rho_p^2 \rho^2 \cos^2 \theta_p}. \tag{4.13}$$

Here ρ_p and θ_p are range and bearing in polar coordinates. Here, to analyze the ovals of Cassini, the distance between Tx and Rx (ρ) and product of ranges (ζ) provides the plot assuming the signal to noise ratio as a constant. If $\rho > 2\sqrt{\zeta}$, then two separate ellipses enclosing Tx and Rx arises, and the mathematical model of ellipse area (A) is given by,

$$A = \pi \zeta \left[1 - \left(\frac{1}{64} \right) \left(\frac{L^4}{\zeta^2} \right) - \left(\frac{3}{16384} \right) \left(\frac{L^8}{\zeta^4} \right) \right]. \tag{4.14}$$

In the scenario of $\rho < 2\sqrt{\zeta}$, a singe continuous ellipse occurs and the ellipse area is given by,

$$A = \frac{2\pi \zeta^2}{L^2} \left[1 + \left(\frac{2\zeta^2}{L^4} \right) + \left(\frac{12\zeta^4}{L^8} \right) + \left(\frac{100\zeta^6}{L^{12}} \right) \right]. \tag{4.15}$$

on the other hand, for $\rho = 2\sqrt{\zeta}$, a lemniscate cup arise at origin and the ellipse area is given as,

$$A = 2\zeta. \tag{4.16}$$

The ovals of cassini analysis is particularly useful for determining the maximum coverage area that given sensors can cover in a passive bistatic scenario.

4.4 Results for the feasibility study

The 5G NR waveform (CP-OFDM) for down-link under consideration has: The center frequency is 6 GHz, the bandwidth per carrier is 5 MHz to 100 MHz, the modulation technique is QPSK, and the FFT size 4096. The transmitted power is 15dBW, the transmitter Gain is 30, the center frequency is 6GHz, receiver Gain is 30 dB, receiver noise temperature is 300K, receiver Noise Bandwidth is 60MHz, and bistatic RCS is 10dBsm. The $F_t = F_r = -3.5$dB and $L_t = L_r = 1$dB. In the passive bistatic radar geometry considered, the distance of transmitter to target is 210Km, and the distance of the target to receiver is 140Km. For the above mentioned geometry as shown in Fig. 4.2, the bistatic angle is computed as 24.43^o.

For these values the bistatic range product$(\rho_t\rho_r)$ is $14.206km^2$, the bistatic radar constant (k) is 202x10^{12}, and the maximum unambiguous PRF is calculated to be 3.996 kHz. The minimum SNR versus bistatic range product for various waveforms is plotted in Fig. 4.4

From Fig. 4.4, we can observe that the rightmost curve corresponds to FM, which is very much pruning to variation in SNR. This shows that usage of FM signals degrades the performance of the radar. In contrast, the leftmost curve in Fig. 4.4 is a 5G NR waveform, which claims that even with the variation in SNR, the corresponding variation in maximum range product is very low, which signifies that the waveform is suitable to get detection. The lower value of the maximum range product signifies the accuracy of detection. The LTE stands next to the 5G waveform in the SNR analysis. Moreover, the relationship between minimum SNR and range product is directly related to range and velocity resolutions. We can infer that the 5G NR waveform outperforms all the existing waveforms for a decent change in minimum SNR from the comparison plot.
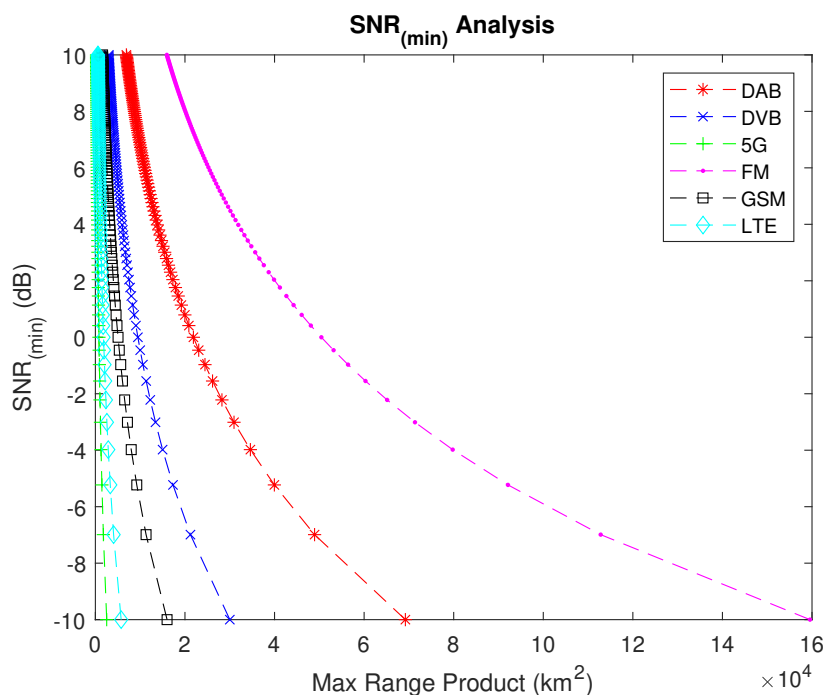
Figure 4.4: Signal to noise ratio versus Maximum Range Product for various IOO
waveforms

For the bistatic angle 24.43^o, the range resolution versus bandwidth is plotted as
shown in Fig. 4.5. The range resolution for the 5G NR waveform is compared with
the LTE waveform in the given frequency ranges. The operating frequency bandwidth
for LTE is swept from 1.4MHz to 20 MHz, and for 5G NR, it is swept from 5MHz
to 100MHz. From Fig. 4.5, the maximum achievable range resolution for LTE is
7.5m at 20 MHz bandwidth. As per the specifications of 5G, it can be tuned from 5
MHz to 100 MHz which gives us improved range resolution as we move significantly
away from 20 MHz compared to LTE. However, during the interval of BW $\in [5-20]$
MHz, both LTE and 5G NR waveform gives the comparable performance. Hence the
benefit of using 5G NR waveform in bistatic radar application is only to visualize the
performance if bandwidth exceeds 20 MHz. Theoretically, at 100 MHz bandwidth
the 5G NR waveform can achieve a 1.5m range resolution. From these results we can
infer that the 5G NR waveform provides better range resolution than LTE due to a
higher operating frequency and higher bandwidth. Therefore the 5G NR waveform
can be adopted at very high bandwidth values for precisely detecting very closely
spaced targets in the passive bistatic scenario.

The velocity resolution for the given geometry and targets is evaluated by varying
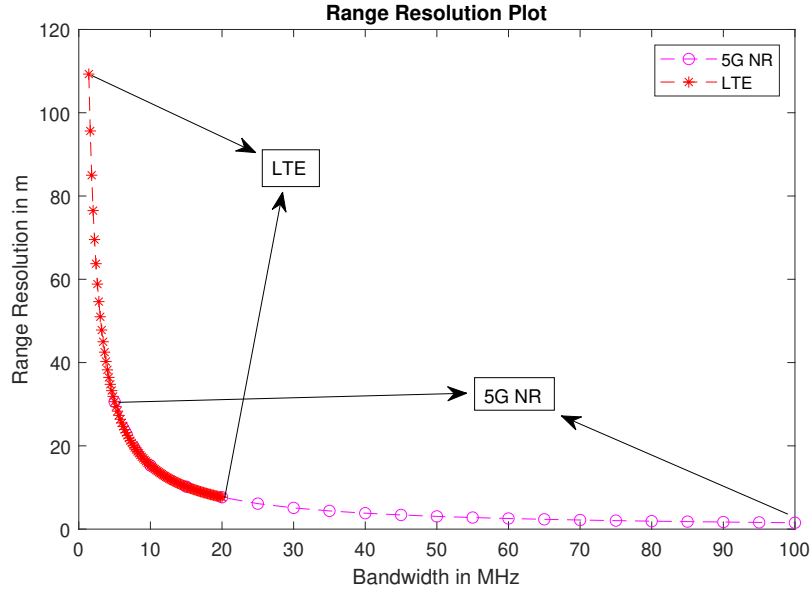
Figure 4.5: Range Resolution in meters for LTE and 5G NR waveforms plotted for wide range of bandwidth

the center frequency and coherence integration time (NT). The LTE is operated in the range of frequencies from 1 GHz to 2.6GHz. In comparison, the 5G NR waveform is proposed to use at 6GHz. Theoretically, we swept the frequency of the 5G NR waveform from 2 to 8GHz to see the velocity resolution performance. For NT = 0.2, the maximum operating frequency of LTE is 2.6 GHz, and it achieves a velocity resolution of 0.13 m/s. Whereas for 5G NR at the operating frequency of 6GHz, the velocity resolution obtained is 0.11 m/sec. Moreover, the coherent integration time is a radar parameter of tunability in the range of 0.2sec to 0.5sec is considered. Therefore we have plotted the velocity resolution for different values of NT {0.2, 0.3, 0.5}. For different coherent Integration Time (CIT) values of 0.2sec, 0.3sec, and 0.5sec, the velocity resolution for LTE and 5G NR waveform, is plotted as depicted in Fig. 4.6. For better Doppler resolution, the CIT should be higher. For the given CIT of 0.5, with a 5G NR waveform, the passive radar can identify a velocity of 0.11m/sec. Hence the 5G waveform may be a very useful candidate for detecting slow-moving targets.

The detection contour plot is as shown in Fig. 4.7 for 5G NR waveform. The Ovals of Cassini illustrate the contour plots for SNR values of 69dB, 72dB, 75dB and 78dB for 5G NR waveform specifications. From the contour plot, it is clear that there is no lemniscate cup at the origin, and it provides a huge coverage area.

The comparative analysis of bistatic radar parameters for LTE and 5G NR wave-

61
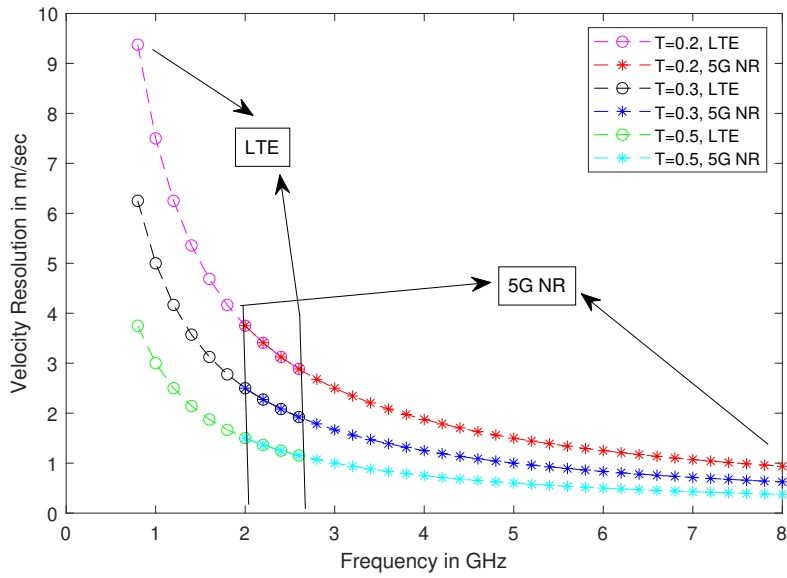
Figure 4.6: Velocity Resolution for coherence integration time values for LTE and 5G NR waveforms
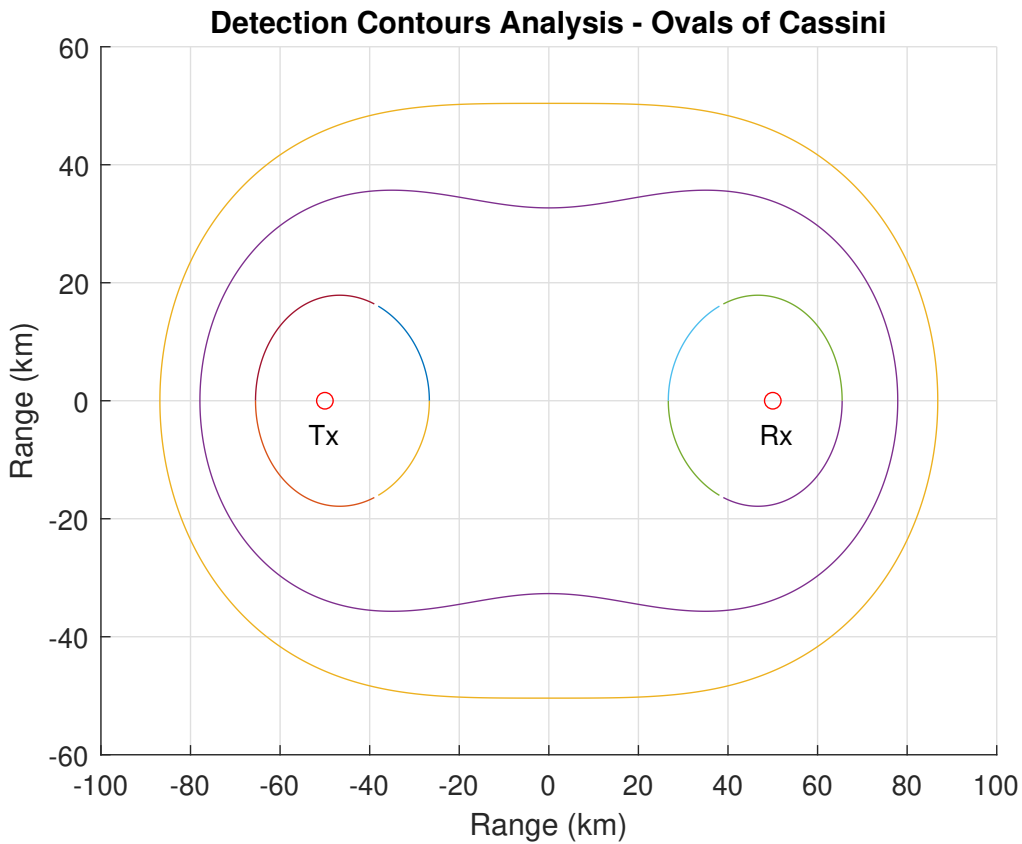
Figure 4.7: Ovals of Cassini for 5G NR waveform

form specifications is as tabulated in the Table 4.1.

Table 4.1: Comparison of passive bistatic radar parameters

Parameter	LTE	5G NR
Frequency(GHz)	2.6	6
Maximum Range Product(km^2)	6.5	14.06
Bistatic Radar Constant	42.7×10^{12}	202×10^{12}
Maximum Unambiguous PRF(kHz)	58.86	40
Range Resolution(m)	7.5	3
Velocity Resolution(m/sec)	0.13	0.11

The 5G NR waveform gives approximately two-fold performance for range resolution and better performance for velocity resolution compared to the LTE waveform. Ovals Of Cassini provide higher area visibility without any lemniscate cup than that of LTE and other waveforms. Overall this simulation study highlighted the feasibility of adopting the 5G NR waveform as the potential transmitter of opportunity for target detection for passive bistatic radar applications. The radar-specific parameters (range resolution, Doppler resolution, velocity resolution etc) are calculated for standard 5G NR waveform specifications, and comparative analysis is carried out with the LTE waveform.

4.5 Conceptual framework to improve the performance of passive radar system

Consider the passive radar system scenario as shown in Fig. 4.8, it contains N IOOs, O_1 and O_2 obstacles, and T_1 and T_2 targets in the environment. The passive radar system has two main blocks, one for the reception of the signals and the other for processing the received signals with aided knowledge to improve the radar's performance. The path A indicates the direct signal path from IOO to the passive radar's reference channel. B represents the IOO signal reflected from the target and received at the surveillance receiver. The IOO signals reflected due to obstacles are C and D. Out of the N IOOs, some IOOs transmit different distinct frequencies based on the intended purpose they are being deployed for, and others transmit the same frequencies. Hence, there is a need to choose the proper IOO for the given application.
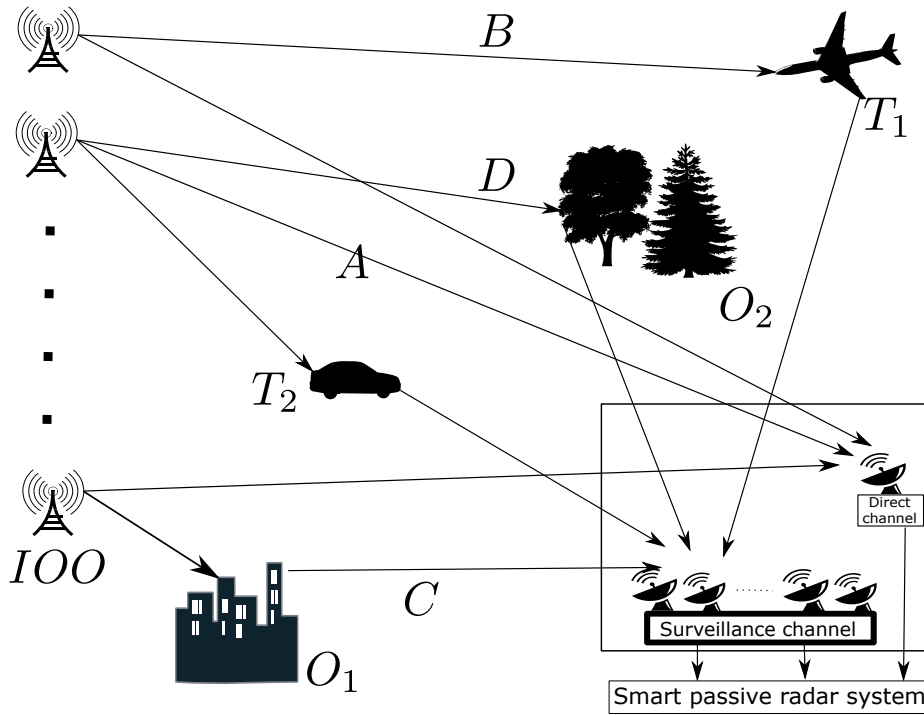
Figure 4.8: Multi static Passive radar scenario having N IOOs

In this multi illuminator passive radar scenario, the proposed smart knowledge aided passive radar system (KA-PRS) aims to follow the below steps:

1. Select the appropriate IOO based on the application and frequency bands.

2. Sense the propagation environment through appropriate spectrum sensing technique.

3. Adopt suitable diversity technique and combining technique to maximize the SNR and provide the countermeasure to jamming.

4.6 Proposed Knowledge Aided Passive Radar System

The cognitive radar defined in (Haykin et al. 2012) briefs that the cognitive radar must possess sequential sensing ability, quick scanning ability, and intelligent and robust signal processing capability. Likewise, the proposed KA-PRS has the above-listed three steps (step-1, step-2, and step-3). In step 1, we continuously sense the radio propagation environment. The appropriate IOO selection for the given range of the target and frequency is chosen in step 2. Finally, in the maximization step (step-3),

spatial diversity is achieved with a maximum ratio combiner technique. Here, the sense and select steps can be interchangeable depending on the context. Fig. 4.9 shows the hierarchy of the overall processing in the KA-PRS. The passive radar receiver system assumes that it possesses information about IOOs (waveform-specific parameters and radar-specific parameters) and the environment (examples like clutter and noise interferences). The parameters like operating frequency, bandwidth, range of the IOO, and the range resolution play a key role in choosing the appropriate IOO for the particular application. Apart from knowing the IOO features and the environment, the receiver has to possess sufficient signal processing hardware, including software-defined radio to scan and sense the frequency band of interest and process the received signal in time.

In brief, the passive radar receiver system with knowledge about the various IOOs in the environment uses the software-defined radio to sense, scan, and choose the IOO that suits the detection application. Further, boost the received signal strength using diversity techniques to combat various interferences.
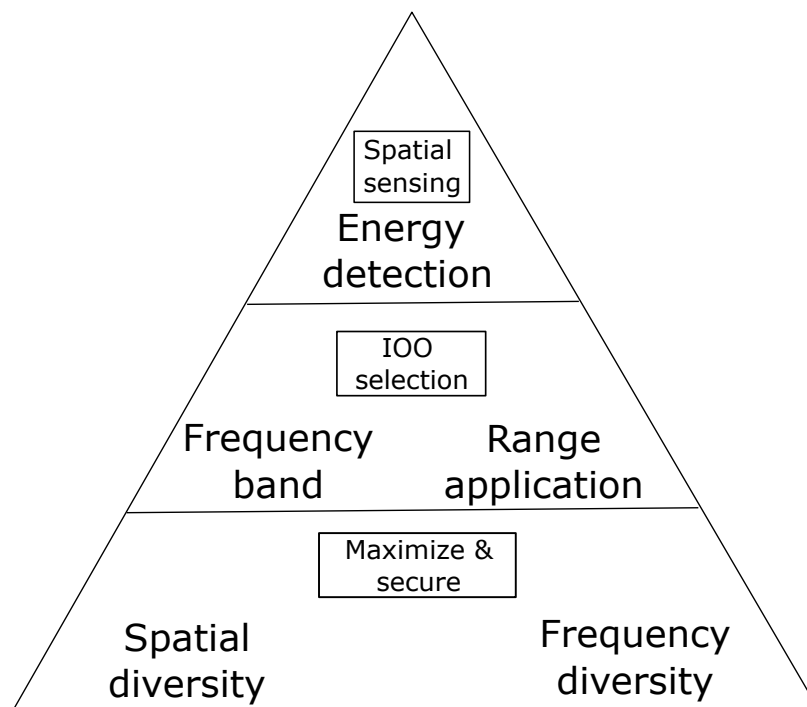
Figure 4.9: The basic processing steps for the smart passive radar system (SPRS).

4.6.1 Spectrum Sensing using Energy detection

Spectrum sensing assists the radar receiver decide whether the signal strength of the IOO of interest is above the functional level. Assume that $\mathbb{H}_0$ indicates only noise, and $\mathbb{H}_1$ indicates the IOO signal's presence. Hence, the received signal can be expressed as

$$\mathbb{H}_0 : z(k) = w_z(k) \tag{4.17}$$

$$\mathbb{H}_1 : z(k) = S_x(k) + w_z(k), \tag{4.18}$$

where $z(k)$ represents the received signal and $w_z(k)$ represents Gaussian noise with zero mean and covariance σ^2. Whereas $S_x(k)$ is the transmitted signal and k denotes the sensing time index. Spectrum sensing techniques like energy detection matched filtering and cyclo-stationary sensing can detect the IOO in the radio environment. Among many spectrum sensing techniques, energy detection requires less-computation time, is lower cost, has minimum power, and does not require any prior information about the IOO signal. These metrics have driven KA-PRS to select the energy detection sensing technique. Let P_{fa} be the probability of false alarm, and P_d is the probability of detection, then

$$P_{fa} = p\left(\mathbb{H}_0 \mid \mathbb{H}_1\right) \tag{4.19}$$

$$P_d = p\left(\mathbb{H}_1 \mid \mathbb{H}_1\right) \tag{4.20}$$
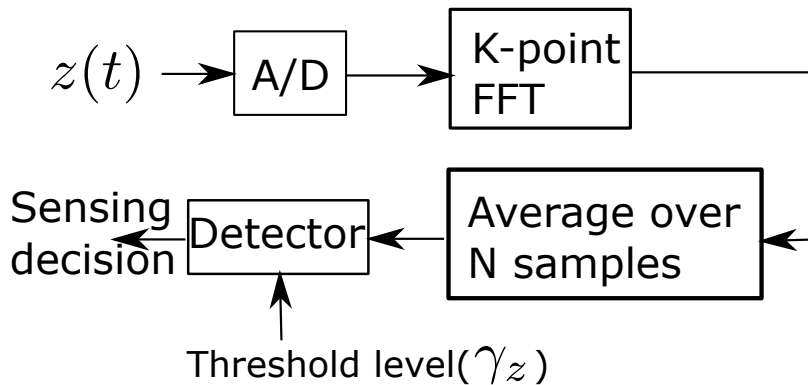
Figure 4.10: Steps for energy detection based Spectrum Sensing

The necessary steps in energy detection are shown in Fig. 4.10. In the Energy detection technique, the received samples' energy calculates and compared with a

Table 4.2: Parameters of Illuminators of opportunity

IOO	F_c	B	$\Delta\rho$
FM	94.4 MHz	50 KHz	3 Km
DAB	219.4 MHz	220 KHz	0.682 Km
DVB-T	505 MHz	6 MHz	25 m
GSM-900	947.5 MHz	81.3 KHz	1.845 Km
WiFi	2.437 GHz	20 MHz	7.5 m
WiMax	2.118 GHz	20 MHz	7.5 m
LTE	2.635 GHz	20 MHz	7.5 m
5G NR(FR1)	6 GHz	50 MHz	1.5 m

predefined threshold level (γ_z). If the received signal's energy is more significant than the threshold, the signal received is considered sufficient signal strength; otherwise, the only noise is present (Arjoune and Kaabouch 2019).

The energy of the received signal is given as,

$$E_{S_x} = \frac{1}{K} \sum_{k=1}^{K} \mid z(k) \mid^2 \tag{4.21}$$

where K denotes the total number of received samples, $z(k)$ is the kth received sample. Mathematically,

$$\begin{cases} E_{S_x} \geq \gamma_z; \text{IOO signal strength is good} \\ E_{S_x} < \gamma_z; \text{Only noise is present} \end{cases} \tag{4.22}$$

Here, γ_z is the dynamic threshold, and it depends on the frequency band to be scanned and the radio propagation environment.

4.6.2 Selection of IOO for Passive Radar System

The available IOOs for the passive radars target different applications based on their coverage area, frequency of operation F_c, bandwidth B, range(R), and range resolution $\Delta\rho$. Table- 4.2 summarizes the different parameters for various IOOs. The approximate range is considered based on the coverage area of the specific IOO, and the range resolution can be calculated by (4.6). The bi-static radar range resolution is the minimum distance required between two targets to resolve them as two separate targets.

4.6.3 Spatial diversity to improve the SNR

Spatial diversity uses multiple antennas to improve the quality of the signal received. Signal Combining techniques for integrating the received signals are selection combining, equal gain combining, and maximum ratio combining. Here, the maximum ratio combining technique is adopted to improve the SNR at the passive radar receiver. The structural representation of maximum ratio combining is shown in Fig. 4.11.

Consider the received signal model as $r_x = h(S_x) + n$, where h is channel impulse response, S_x is the transmitted signal. Whereas n is the additive white Gaussian noise. All K signals are scaled according to the weights (w_i) and combined to maximize the output SNR. Here, we assume that the channel impulse responses (h_k) are known to the receiver (Sankar).
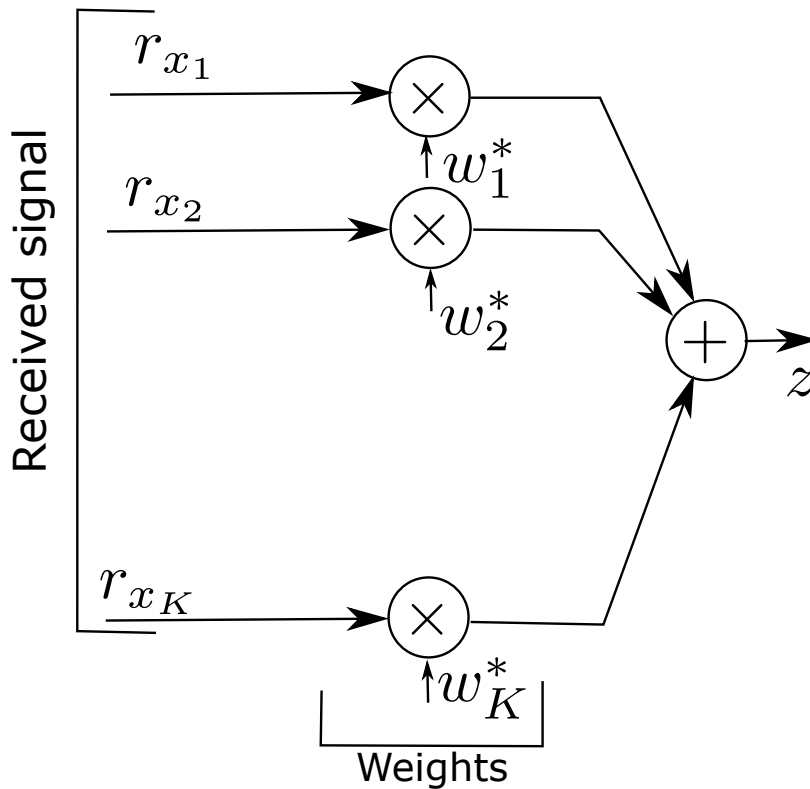
Figure 4.11: Maximum ratio combining for spatial diversity based receiver system

Let $w_k = h_k$ and $k = 1, \ldots, K$, the output of the combiner is

$$Z = \sum_{k=1}^{K} w_k^* r_{x_k} = W^H h S_x + w^H n \tag{4.23}$$

$$= \left(|h_1|^2 + |h_2|^2 + \cdots |h_K|^2 \right) S_x + n \tag{4.24}$$

$$= \sum_{k=1}^{K} |h_k|^2 + n \tag{4.25}$$

The output SNR after combining is

$$SNR_{out} = \sum_{k=1}^{K} \frac{\mathbb{E}\left\{ |S_x|^2 \right\} |h_k|^2}{\sigma_x^2} \tag{4.26}$$

where σ_x^2 is the variance of the noise. Finally

$$SNR_{out} = \sum_{k=1}^{K} SNR_k \tag{4.27}$$

Maximum ratio combining results in weighted average of received signals. The SNR_{out} is sum of the individual SNRs of received signals.

4.7 Discussion on improving received signal strength

KA-PRS adopts the energy detection method for the spectrum sensing step because of its inherent advantages like bandwidth, prior information about the IOO, computational load, the time required for sensing, the cost for implementation, and the power consumption.

The power spectral density plot for the energy detection-based spectrum sensing is shown in Fig. 4.12. For the simulation purpose, we have generated five IOOs with frequencies of 100 MHz, 200 MHz, 300 MHz, 400 MHz, and 500 MHz with user-defined amplitudes. The IOOs are made to pass through the Additive White Gaussian Noise (AWGN) channel. The power spectral density is calculated by choosing the Nyquist sampling frequency for each signal. The plot highlights the presence of the IOO signal at 100 MHz.

For the simulation, we have considered binary phase-shift keying modulated waveform for an AWGN channel. The SNR varies from -16 dB to -4 dB, and the signal passes through the AWGN channel. The threshold for detection (γ_z) is adaptive considering the number of samples, noise variance, and the probability of false alarm
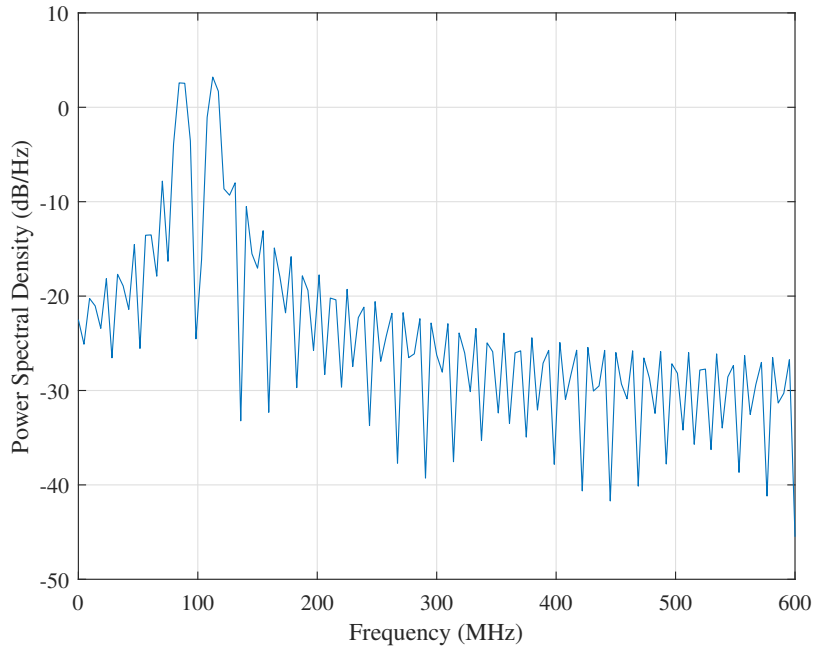
Figure 4.12: Power spectral density in dB/Hz vs frequency in MHz

(P_{fa}). The simulations are quantified for a hundred Monte Carlo runs. The probability of detection (P_d) versus SNR ratio is depicted in Fig. 4.13. It is evident from the results that, for a given P_{fa}, the probability of detection increases with an SNR increase. Hence, it can be inferred that by choosing an appropriate IOO which gives good signal strength, one can attain better detection. The selection step chooses the appropriate IOO based on the application.

In Fig. 4.14, the importance of high SNR for the given propagation environment is presented. From the plot, we can infer that with the increase in SNR, the probability of false alarm decreases, considering all other parameters as constant. So, there is a requirement for improving the SNR at the passive radar receiver. The KA-PRS maximizes the SNR using the appropriate signal combining technique.

As explained in the previous section, the receiver knows all the IOOs in the surveillance area. It has features about the radio environment like clutter, noise, and jamming. The range and the range resolution are the vital parameters for selecting a particular IOO. Further, if the surveillance environment has clutter and jammer, then the digital waveforms like DAB and DVB-T is chosen by considering the range as the secondary criteria.

The IOO selection by the KA-PRS is as follows:

70
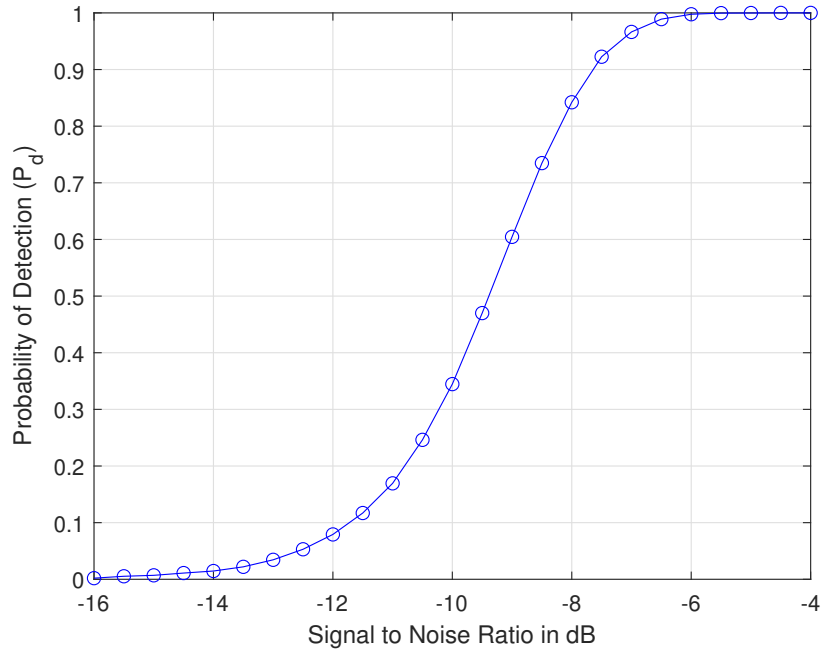
Figure 4.13: Probability of detection vs signal to noise ratio in energy detection

- Depending on the approximate range of the target, the system selects the IOO signal. For example, to detect a huge target (aircraft, ship) at a distance up to 100 Km, the system selects FM waveform. Whereas, for small targets (car, truck, drone) at a lesser distance, the system selects a DVB-T waveform.

- For multi-target cases, the passive receiver chooses a waveform with good range resolution. From Table- 4.2, we can infer that higher bandwidth signals produce improved range resolution. Depending on the range at which the targets are present, the receiver chooses a waveform that gives better range resolution for long-range targets.

- If the target range is vast, then the IOO with global coverage will be used (GNSS). For maritime and other imaging, short-range applications DVB-T waveform gives better detection performance. Whereas for indoor applications, WiFi signals are of choice.

- If the propagation environment is noisy or barrage jammer is present, the passive receiver will choose digital waveforms like DAB and DVB-T instead of FM signal.
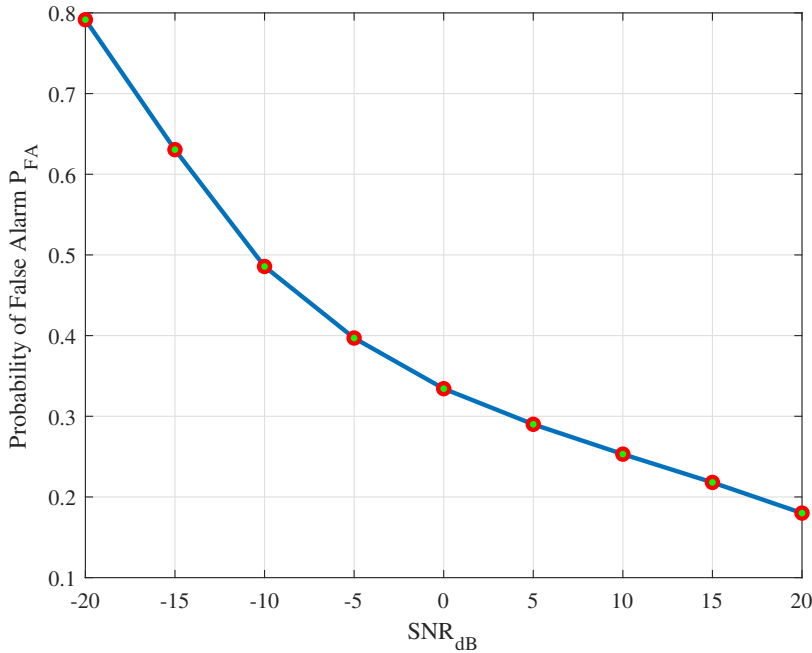
Figure 4.14: Probability of false alarm vs signal to noise ratio in energy detection

- In Table- 4.2, the frequency, bandwidth, and range resolution for the upcoming 5G NR waveform are also provided. For a very high range resolution application, the receiver system can opt for a 5G NR waveform.

Concluding, the KA-PRS adopts an IOO based on the type of the application, range of the targets, number of targets to be detected, range resolution, and the propagation environment.

For simulation, K passive receiver antennas and one IOO (transmit antenna) is considered. The channel is assumed to be Rayleigh fading, and each receive antenna has independent channel noise characteristics. The IOO is assumed to be transmitting binary phase-shift keying modulated waveform. The Gaussian noise is added and assumed to have zero mean and variance zero dB in a particular channel. For simplicity, the weights in the maximum ratio combiner are equal to unity. The output SNR versus antenna elements number are plotted as shown in Fig. 4.13. The number of antenna elements is varied from 1 to 15. From Fig. 4.15, we can infer that the overall SNR_{out} increases as the number of antenna elements in the maximum ratio combiner increases.

The simulation study carried out for KA-PRS in this work highlights the advantage of choosing the favorable IOO based on the range and range resolution for the passive

72
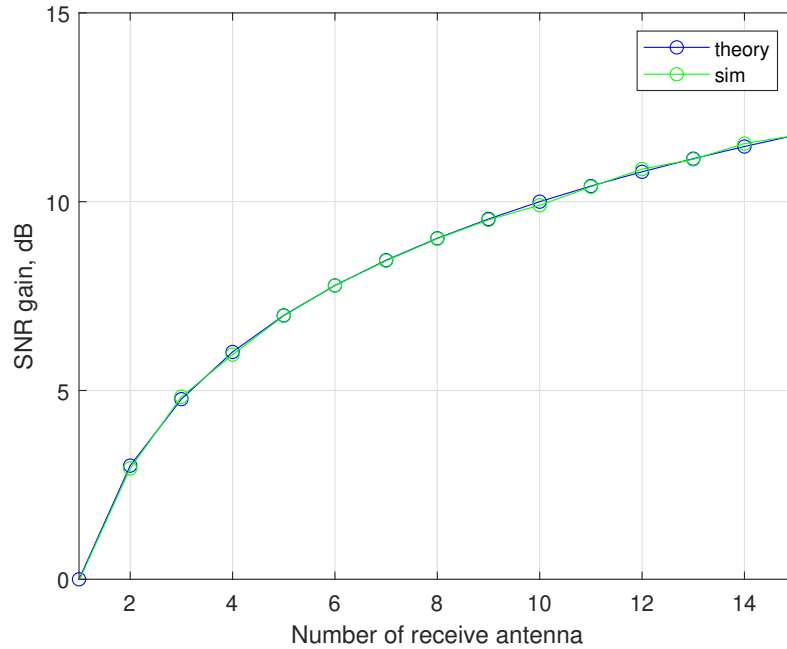
Figure 4.15: Signal to noise ratio improvement using maximum ratio Combining

radar receiver system. The sense (step-1) and select (step-2) steps help the receiver choose the appropriate IOO based on the application. Further, in the maximize step (step-3), the received signal's output SNR can be improved by applying the maximum ratio combining technique, which is illustrated by the simulation. Overall, by combining the sense (step-1), select (step-2), and maximize (step-3) steps in a structured manner, improved detection performance can be accomplished in KA-PRS. As a future work incorporating frequency diversity at the receiver helps to combat deception jamming.

4.8   Conclusion

This chapter proposed a feasibility study of the 5G NR waveform as an IOO for passive radar. Further, this chapter also proposed a conceptual framework using KA-PRS to improve the received signal strength at the passive radar. In addition, there is a need to understand the losses incurred by several IOOs, when they pass through various atmospheric conditions. Therefore, a comprehensive study of atmospheric losses has been carried out in Chapter 5. Further, it is necessary to measure penetration losses in an indoor environment. Hence, experimental analysis has been performed to measure the penetration losses using a real radar system and is presented in Chapter 5.

Chapter 5

Impact of various losses on Illuminators of Opportunity

5.1 Preamble

Passive radar offers significant advantages in detecting stealthy targets, as well as other advantages such as covertness and efficient spectrum utilization. Significant advantages of the passive radar in the detection and tracking of targets have been demonstrated in recent literature. However, the received signal power depends on various losses (atmospheric losses and receiver signal processing losses) incurred during the transmission and reception of the RF waveform. This work proposes a comprehensive analytical study of various losses for the IOOs commonly adopted by the passive bistatic radar. The different IOOs considered in this investigation are FM waveform, DVB waveform, Long Term Evolution Waveform and 5G NR waveform, etc. The atmospheric losses considered in this work are path loss, rain loss, gas loss, fog loss, foliage loss, etc. From the simulation results, it is evident that the high frequency 5G NR FR2 waveform (26GHz to 50GHz) suffers significantly higher losses compared to other IOOs even though it provides improved range and velocity resolution. On the other hand, the FM waveform suffers from insignificant losses compared to other IOOs in spite of having poor range and velocity resolution. Furthermore, the results obtained in this contribution can be a useful reference for passive bistatic radar as the analysis is comprehensive that includes all IOOs along with the newly proposed 5G NR waveform. Additionally, an experimental study has been carried out using the Texas Instrument AFE7950 radar sensor for the measurement of penetration losses for common building materials.

5.2 Passive Radar Scenario and Propagation Environment
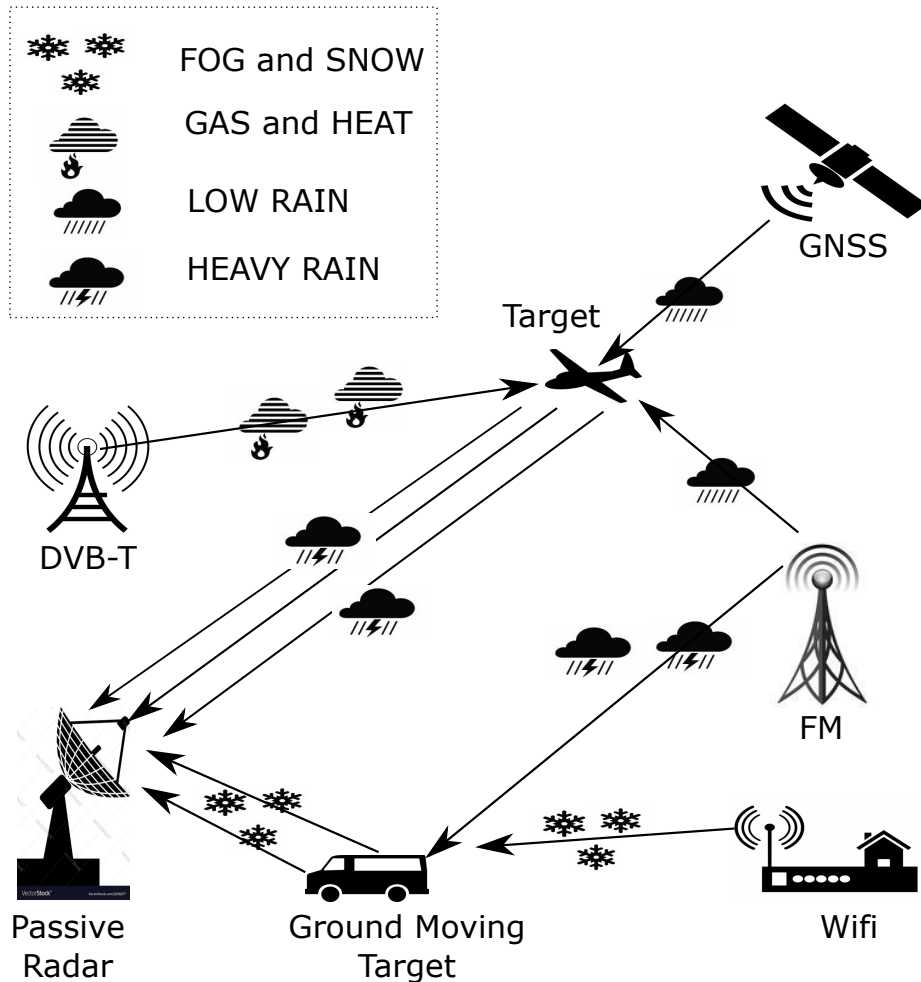
Figure 5.1: Passive multistatic radar scenario

Fig. 5.1 shows a passive radar scenario, where different IOOs are considered for detecting the targets in the surveillance area. Here a single multi-band passive radar is shown for the reception of the waveforms and detection of targets. There may be more than one passive radar site in real-time. The waveform from an IOO transmitter hits the target, and a copy of the signal scattered from the target will be received at the passive radar. The signal is further processed based on the frequency of operation for target detection. Different impairments like rain, fog, gas, and foliage may affect the wave propagation at specific frequencies is shown.

For the scenario shown in Fig. 5.1, we are considering the transmitter-target-passive radar receiver as a passive bistatic radar system. Also, for analysis, we presume

that the electromagnetic signal from IOO travels from the transmitter of opportunity to the target and the target to the receiver. Along the path of traversal, it follows Frii's free space wave propagation model (Haslett 2008).

This work aims to investigate the effect of path loss on different IOOs, considering the frequency and power density of the corresponding IOO. The rain loss suffered by individual IOOs shall be computed by taking rain rate as the key parameter. Further, the effect of fog and gases in the atmosphere on the propagation and reception of different IOOs will be analyzed. Moreover, the diffraction loss using an appropriate mathematical model for different IOOs will be analyzed. In addition, considering the atmospheric losses along with the signal processing losses, the total losses can be computed, which helps the passive radar to have an estimate of the total losses that will be incurred during its transit from the transmitter to the receiver. Finally, the signal-to-noise ratio for individual IOOs are calculated and plotted using the bistatic passive radar equation.

5.3 Assumptions and Mathematical Modelling for Passive Bistatic Radar and Losses

5.3.1 Passive Bistatic Radar Geometry

Fig. 5.2 shows the basic structure of the bistatic arrangement of passive receiver system. The transmitter (Tx), which is an IOO and receiver (Rx), which is a passive radar receiver system are situated at $\mathbf{x}^{Tx}$ and $\mathbf{x}^{Rx}$ correspondingly. The distance of separation between the IOO and receiver is given by $\rho_x = \mid \mathbf{x}^{Tx} - \mathbf{x}^{Rx} \mid$. The object to be detected (target) is located at $\mathbf{x}^t$. The distance of separation between transmitter and target is considered as $\rho_{tx} = \mid \mathbf{x}^{Tx} - \mathbf{x}^t \mid$. Furthermore, the distance between target and passive receiver is $\rho_{rx} = \mid \mathbf{x}^t - \mathbf{x}^{Rx} \mid$. The angle formed at the target by lines joining the transmitter and receiver denoted by β_x is given as,

$$\beta_x = \sin^{-1} \left(\frac{\rho_x \cos \theta_{rx}}{\rho_t} \right) \tag{5.1}$$

where θ_{rx} is the angle subtended at the receiver with respect to the base line. The transmitter (IOO) is assumed to transmit the physical waveform at center frequency (f_c), and bandwidth (B_x) with transmitted power and gain product $(P_{tx}G_{tx})$ as indicated in the Table 5.1. The waveform reflected off the target is utilized to find the

detections of the target. While analysing the atmospheric effects, and other losses all
the commonly existing IOO waveforms and the newly proposed 5G NR waveform are
considered. Majority of the losses depends on center frequency and, bandwidth of
operation. Furthermore, the atmospheric losses due to rain, fog, gas, cloud, refraction
from earth, and other causes is studied for passive bistatic radar system (Lingadevaru
et al. 2021, Griffiths and Baker 2017b).
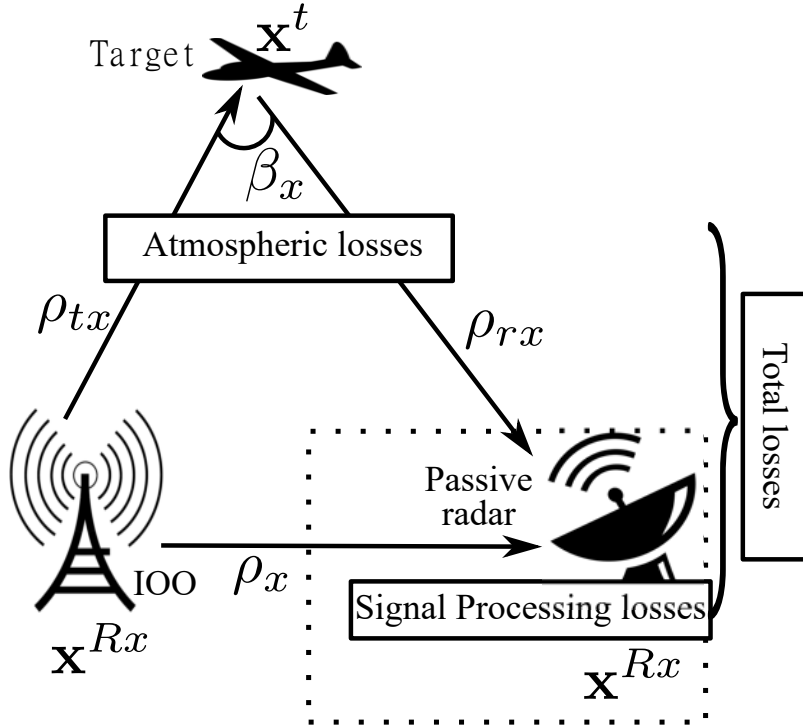
Figure 5.2: Passive bistatic radar consisting of the IOO transmitter (Tx) situated at
X^{Tx}, Passive Radar Receiver (Rx) situated at X^{Rx} and the target located at X^t.

The Signal to Noise Ratio (Griffiths and Baker 2017b) for the bistatic passive
radar is given by

$$\left(\frac{S}{N}\right) = \left[\frac{P_{tx}G_{tx}G_{rx}\lambda_x^2\sigma F_{tx}^2 F_{rx}^2}{(4\pi)^3 kT_r B_n \left(\rho_{tx}^2\rho_{rx}^2\right) L}\right],\tag{5.2}$$

where P_{tx} is the transmitted power, G_{tx} is the gain of the transmitting antenna (IOO),
G_{rx} is gain of the passive radar receiver antenna, λ_x indicates wavelength of the IOO
waveform, σ is radar cross section of the object to be detected, F_{tx} is the propagation
factor from IOO to the target, F_{rx} propagation factor from the target to passive radar
receiver, k is Boltzmann's constant, T_r is the noise temperature of passive receiver,
bandwidth B_n indicates the passive receiver noise bandwidth, $\left(\frac{S}{N}\right)$ is the signal to

noise ratio, L indicates the sum of all the losses incurred by passive receiver system. Here, $(\rho_{tx}\rho_{rx})_{\max}$ is bistatic maximum range product (Kuschel et al. 2019b).

The range resolution, velocity resolution and other bistatic radar parameters can be defined and calculated by the equations given in section 4.3.

5.3.2 Illuminators of Opportunity

The IOOs for analyzing the effect of atmospheric losses on the radar-specific parameters are as shown in Table 5.1 (Salah et al. 2013, 2014, Henry et al. 2020). The center frequency (f_c), bandwidth (B_x) the transmitted power and gain ($P_{tx}G_{tx}$) of the various IOOs under consideration for analysis are as mentioned. While calculating the various losses, we have considered this Equivalent Isotropic Radiated Power (EIRP) ($P_{tx}G_{tx}$) as reference. For calculating the path loss, the paths from the transmitter (IOO) to the target and the target to the passive receiver are considered, and both the paths are assumed to have atmospheric losses and are affected by other external factors. The aim is to compare the losses incurred by the individual IOOs.

The 5G NR waveform is specified in two frequency ranges: the 6 GHz band, which is termed FR1, and the higher millimeter wave band, which is named FR2, which ranges from 24.25GHz (FR2-Lower) to 52.6GHz (FR2-Upper). The operative bandwidth varies from 20MHz to 100MHz for the 5G NR FR1 waveform, and the spacing between the subcarriers is nearly 15KHz to 30KHz. Whereas bandwidth for the 5G NR FR2 waveform ranges from 100MHz to 400MHz, and the spacing between the sub-carriers is 120KHz. In some cases, sub-carrier spacing of 60 kHz is used both in FR1 and FR2 waveforms (ShareTechNote).

5.3.3 Various Losses incurred by an IOO

Fig. 5.1 shows the pictorial representation of propagation scenario for an IOO utilized by the passive bistatic radar under various losses incurred.

A Path Loss (L_p)

The attenuation of the IOO waveform along it's traversal path towards the target and then passive receiver is known as path loss which uses a point-to-point connection. The mathematical model to calculate path loss (in dB) is given by (Grecu et al. 2015),

Table 5.1: Key specifications for the IOOs

Waveform (IOO)	f_c in GHz	B_x in MHz	$P_{tx}G_{tx}$
FM	0.0944	0.050	250 kW
DAB	0.2194	0.220	10 kW
DVB-T	0.505	6.0	8 kW
GSM-900	0.9475	0.0813	100 W
WiFi	2.437	20	100 mW
WiMax	2.118	20	20 W
LTE	2.635	20	69 W
5G NR(FR1)	6.0	50	20 W
5G NR(FR2)	24.25 - 52.6	100	20 W

$$L_p = 20 \log \frac{4\pi d}{\lambda_x} \tag{5.3}$$

where d is the distance of separation from the IOO transmitter and passive radar receiver, and λ_x is the wavelength of the transmitted waveform. The above equation (6) can be rewritten in terms of frequency of the transmitted waveform as,

$$L_p = 32.4 + 20 \log f_c + 20 \log d \tag{5.4}$$

B Rain Loss (L_r)

The wireless propagation is affected by the rain and depends on the rain rate in the given area. The basic rain attenuation η_R (dB/km) can be computed from the rain rate R (mm/h) by utilizing the power law relationship:

$$\eta_R = kR^{\alpha_r} \tag{5.5}$$

The values of k and α_r are functions of frequency in the range of 1 to 1000 GHz and can be calculated by using the following expressions:

$$\log_{10} k = \sum_{j=1}^{4} \left(a_j \exp\left[-\left(\frac{\log_{10}(f_c) - b_j}{c_j} \right)^2 \right] \right) + m_k \log_{10}(f_c) + c_k \tag{5.6}$$

$$\alpha_r = \sum_{j=1}^{5} \left(a_j \exp\left[-\left(\frac{\log_{10}(f_c) - b_j}{c_j} \right)^2 \right] \right) + m_\alpha \log_{10}(f_c) + c_a \tag{5.7}$$

where, the values of k, α_r, m_k, m_α, b_j, and c_j are specified for horizontal and vertical polarizations of the received EM wave and theses values can be obtained from the rain tables of ITU-R specifications (Ononiwu et al. 2015).

C   Gas Loss (L_g)

For the frequencies at gigahertz range the uncondensed water vapour and oxygen act as highly absorptive. Besides, the gas loss attenuation is mainly because of dry air and water vapour in the atmosphere which mainly attenuates the microwave and mmWave frequencies. The specific gaseous attenuation is expressed as,

$$\gamma = \gamma_{ox} + \gamma_{wa} \tag{5.8}$$

$$= 0.1820 f N''(f) \quad \text{dB/km} \tag{5.9}$$

$$= 0.1820 f (N''_{oxygen}(f) + N''_{watervapour}(f)) \quad \text{dB/km} \tag{5.10}$$

where, γ_{ox} and γ_{wa} are attenuations because of dry air (oxygen) and water vapour. Whereas, $N''(f)$ is an imaginary component of frequency dependent complex refractivity for oxygen and water vapour. Further, the values of $N''_{oxygen}(f)$ and $N''_{watervapour}(f)$ are as given below:

$$
\begin{aligned}
N''_{\text{Oxygen}}(f_c) &= \sum_{j(\text{ Oxygen })} S_j F_j + N''_D(f_c) \\
N''_{\text{Water Vapour}}(f_c) &= \sum_{j(\text{ Water Vapour })} S_j F_j
\end{aligned}
\tag{5.11}
$$

where, S_j is the strength of the jth oxygen or water vapour line, F_j is the shape factor of oxygen or water vapour line which are formulated under gas loss of ITU-R specifications (Al-Ansari et al. 2001) and $N''_D(f_c)$ is the dry continuum because of pressure-induced nitrogen absorption. The shape factor value for a given pressure, humidity and temperature in atmosphere is calculated as given in ITU-R specifications (Al-Ansari et al. 2001). The value of the shape factor for oxygen and water vapour can be calculated by,

$$
\begin{aligned}
S_j &= a_1 \times 10^{-7} p \theta^3 \exp\left[a_2(1-\theta)\right] && \text{for oxygen} \\
&= b_1 \times 10^{-1} e \theta^{3.5} \exp\left[b_2(1-\theta)\right] && \text{for water vapour}
\end{aligned}
\tag{5.12}
$$

where, p is the dry air pressure in hectopascal (hPa), e is the partial pressure of the water vapour in hPa, $\theta = 300/T$, and T is the temperature in K.

D Fog Loss (L_f)

Fog is made up of tiny water droplets floating in the air near the earth's surface. These droplets act on the high frequency signals to scatter them and induce losses. The Rayleigh estimate is accurate for frequencies below 200GHz for clouds or fog composed solely of small scale droplets, usually their size is lower than 0.01cm, and the attenuation can be expressed in terms of total water content per unit volume (Nagaraj 2018). As a result, a cloud's or fog's particular attenuation can be written as:

$$\gamma_{f_c} = K_{f_c} M \tag{5.13}$$

where γ_{f_c} is the specific attenuation expressed in dB/Km inside the cloud, K_{f_c} is the specific attenuation coefficient in $(dB/m)(g/m^3)$, and M is the liquid water density in the cloud in g/m^3. Fog attenuation may be important at frequencies on the order of 100GHz and higher. For moderate fog (visibility of the range of 300m), M is generally about 0.05 g/m^3, whereas thick fog (visibility of the range of 50 m) has a value of M = 0.5 g/m^3.

For frequencies up to 1000GHz, a statistical formula grounded on Rayleigh scattering that adopts a double-Debye model for the complex dielectric permitivity $\epsilon(f)$ of water shall be utilized to measure the value of K_{f_c} given by:

$$K_{f_c} = \frac{0.819 f_c}{\varepsilon^n (1 + \eta^2)} \tag{5.14}$$

where f_c is the frequency in GHz and η depends on complex permitivity of the water.

E Foliage Loss (L_{fl})

Attenuation due to trees and other vegetation is one of the most significant obstacles in wireless propagation. Randomly dispersed leaves, tree segments, tree trunks, and twigs make up the various elements of the foliage. Because of multipath propagation, diffraction, and reflection, the waveforms traversing the foliage environments like plantations and forests diminish their signal strength. The key factors influencing the actual attenuation by foliage are the depth of foliage, the existence of wind, and humidity (Meng and Lee 2010). The smaller wavelength (high frequency) waveforms are more prone to blockage due to foliage obstruction.

Weissberger modified exponential decay (WMED) model can be used to calculate the foliage loss. Mathematically WMED model can be written as follows (Zhang et al. 2019):

$$L_{fl}(s) = \begin{cases} 0.45\, f_c^{0.284}\, d_f(s), & \text{if } 0 < d_f(s) \leqslant 14 \\ 1.33\, f_c^{0.284}\, d_f^{0.588}(s), & \text{if } 14 < d_f(s) \leqslant 400 \end{cases} \tag{5.15}$$

where f_c is the center frequency of the IOO, and $d_f(s)$ is the foliage depth in meters along the line of sight path for the passive radar receiver location s. The model identifies locations with $d_f(s) > 14$ separately from those with lower foliage depth.

F Diffraction Loss (L_{Diff})

The field strength in the shadowed region can be computed by the vector combination of various signals arriving from alternate paths. The knife edge diffraction (KED) model is commonly applied to calculate diffraction loss, which presumes that a single sharp edge separates the IOO transmitter and the passive radar receiver. The propagation loss because of the diffraction in the knife edge model is dependent on Fresnel diffraction Parameter. The diffraction parameter indicates the depth at which the passive receiver is within the shadowed region. The KED model is appropriate whenever the clutter is flat and thin, like a knife. Because of the ease of calculation, the KED model can be adopted extensively in most clutter scenarios. The KED model computes the diffraction loss using the sum of all the diffracted waves from different path lengths using the Fresnel integral. Then, the field strength generated by the total diffracted waves is computed using,

$$F(v_x) = \left| \frac{1+j}{2} \int_{v_x}^{\infty} e^{-j\frac{\pi}{2}t^2} dt \right| \tag{5.16}$$

Here the electric field induced by diffraction is represented by $F(v_x)$. Further, the Fresnel-Kirchhoff diffraction parameter is represented by v_x and is expressed as

$$v_x = 2\sqrt{\frac{\Delta}{\lambda_x}} \tag{5.17}$$

where the wavelength is denoted by λ_x, and the difference in the lengths between a direct line-of-sight path and a diffracted wave path is indicated by Δ. In case of

absence of the clutter v_x is $-\infty$ and $F(v_x)$ is 1.

For simplifying the calculation, an approximated model for the diffraction loss is given in (ITU 2018), and can be expressed as,

$$L_{\text{Diff}} = 6.9 + 20\log\left(\sqrt{(v_x - 0.1)^2 + 1} + v_x - 0.1\right) \tag{5.18}$$

L_{Diff} indicates the loss because of diffraction.

G Signal Processing Losses (L_{sp})

The significant signal processing effects that put up to the system losses are beam shape loss, straddle loss, and automatic detection constant false alarm rate (CFAR) loss (Richards et al. 2010). The radar range equation is formulated using the peak antenna gain by assuming that the target is in the middle of the beam pattern, which results in beam shape loss. The accurate value of beam shape loss is dependent on the particular shape of the beam and the scan time, but the average beam shape loss for a typical case is about 1.6dB. Further, a target is not always in the center of a range bin or a Doppler filler, which causes Straddle loss. Further, it is possible that the received pulse/spectrum is halfway between two range bins and halfway between two Doppler fillers, lowering the target signal strength in one bin. Oversampling in range and Doppler can minimise straddle loss, and the estimated average loss is roughly 1dB (Cann 2002).

$$L = L_a + L_{sp} \tag{5.19}$$

$$= L_p + L_r + L_g + L_f + L_{fl} + L_{Diff} + L_{sp} \tag{5.20}$$

Most existing radars are intended to detect targets in the presence of receiver noise, intentional interference (noise jamming), electromagnetic interference, and clutter. Besides, a CFAR processor might be used to evaluate the presence of a target due to the unpredictability of the interfering signals. Due to the external factors and the interference, the probability of false alarm becomes high, which lowers the target detection probability. To overcome this, SNR is increased to optimize the probability of detection, which is considered CFAR loss. The typical value of the CFAR loss is of the order of $1 to 2$ dB. Further, the fluctuation loss is considered to be the result

of swerling models of radar cross-section of the target. Usually, the fluctuation loss (for a high probability of detection of 0.99) would be approximately 8dB for Swerling 1 targets with the number of integrated pulses equal to 50 (Swerling 1997). Hence, the total signal processing loss can be considered as 10dB to 12.6dB approximately. Further, the overall system loss (L) in (5.19) is considered as the sum of all the atmospheric losses (L_a), and the signal processing losses (L_{sp}).

5.4   Results and Discussions

In this work, we simulate and study the effects of atmospheric losses, foliage loss and diffraction loss on receiving an IOO signal by a passive bistatic radar. Various wireless propagation losses like path loss, rain loss, fog loss, diffraction loss, foliage loss, gas loss, and signal processing losses are calculated and analysed for specific frequencies corresponding to the IOOs. The propagation path is considered as the bi-static range. The parameters for the IOO waveform propagation are frequency of operation (center frequency for specific IOO), the range (1 Km bi-static range for comparison work), rain rate ($0.25 - -50$mm/h), liquid water density ($0.05 - -0.5$ g/m^3), water vapor density ($7 - -21.9$g/m^3), foliage depth ($10 - -50$ m), path difference ($100 - 1000$m), dry air pressure (at 101300 Pa), temperature(at 15°C) and horizontal polarization of the EM wave. At the receiver end, the total signal processing loss is 12.6dB for SNR analysis. For computing the total losses the critical values of the above parameters are given in Table 5.2.

5.4.1   Radar Parameter Analysis for IOOs

The range resolution and velocity resolutions' are the key parameters that are calculated for all the IOOs using respective equations and are tabulated in Table 5.3. The FM waveform can be used to detect the targets at longer range but for the detection of multiple targets it gives inaccurate results, since the range resolution for FM signal is nearly 3Km. Most commonly used waveform for detecting and tracking the multiple targets is DVB-T waveform is adopted that provides good range resolution of 30m. For the detection and tracking of multiple targets, the passive radar can adopt the waveform, which gives a better range resolution to detect the closely moving targets.

Table 5.2: Parameters for Loss Analysis and SNR Calculation

Parameter	Value
Rain Rate	20 mm/h
Liquid Water Density	0.2 g/m^3
Water vapor density	15 g/m^3
Foliage depth	10 m
Path Difference	100 m
Dry air pressure	101300 Pa
$F_t = F_r$	-3.5 dB
Receiver Noise Temperature	288.15 k
Receiver Gain	30 dB
Bistatic RCS	1 m^2
Bistatic Angle	24.43^o
Receiver Noise Bandwidth	60 MHz

Further, the waveform with a lesser velocity resolution detects and tracks the slow-moving targets. The 5G NR FR2 waveform gives a good range resolution of 1.5m and a velocity resolution of 0.055m/sec, making it a suitable candidate for detecting slow-moving and closely-spaced targets.

5.4.2 Path loss analysis

The free space path losses (in dB) are calculated as a function of propagation distance and frequency. The path loss corresponding to various IOOs is presented in Fig. 5.3. For comparing the path loss for all the nine IOOs we have considered the bistatic range of 1Km while calculating the path loss analysis, total loss computation and SNR analysis. From the plot, we can infer that path loss increases as the frequency of IOO increases. For a given range the 5G NR FR2 waveform suffers more path loss compared to other IOOs.

For further investigating the path loss specific to the IOOs based on the maximum range of individual IOO is applied. For a passive bistatic radar using an FM signal as an IOO, the path loss is approximately 107.5dB for a maximum range of

Table 5.3: Range and Velocity Resolution for IOOs

IOO(Waveform)	Bandwidth	$\Delta\rho$ in m	Δv in m/sec
FM	50 KHz	2990	3.5
DAB	220 KHz	680	1.5
DVB-T	6 MHz	30	0.6
GSM-900	81.3 KHz	1850	0.35
WiFi	20 MHz	7.5	0.2
WiMax	20 MHz	7.5	0.18
LTE	20 MHz	7.5	0.13
5G NR(FR1)	50 MHz	3	0.11
5G NR(FR2)	100 MHz	1.5	0.055
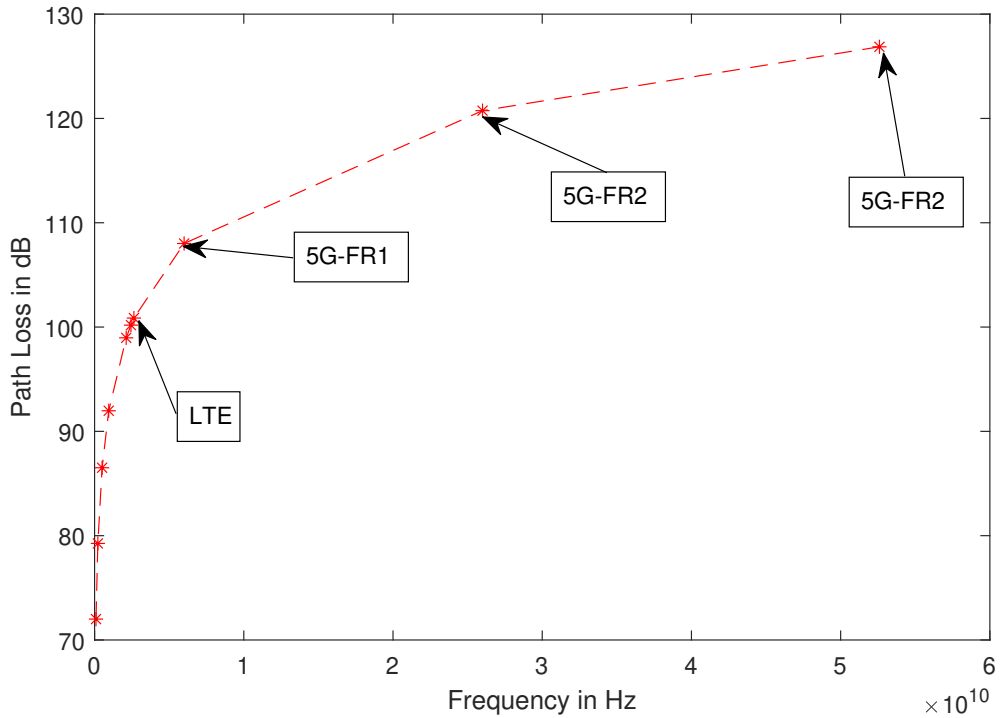
Figure 5.3: Path Loss in dB for various illuminators of opportunity

50Km. The DAB and DVB signals suffer a path loss of 116.66 dB for the maximum range of 70Km and 123.06dB for a maximum range of 60Km, respectively. Since the WiFi signals operate at shorter distances for indoor and outdoor applications, their

path loss is nearly 80.18dB at a 100m bistatic range. The WiMax signal for a non-line of sight condition pertains to a loss of 118.96dB at the bistatic range of 10Km. Moreover, the LTE signal comparatively operating at high frequency suffers a path loss of 111dB for a range of 3.2Km. For the upcoming 5G NR waveforms for FR1 and FR2 frequency specifications, the path loss is approximately 108dB and 120.4dB, respectively, for 1Km maximum range. Since the transmitted EIRP for 5G NR waveform is small, this gives substantial path losses and results in smaller received signal strength. Appropriate signal processing techniques are to be incorporated in the 5G NR waveform to improve the signal strength at the receiver. Since the miniaturized radars and the 5G waveform are upcoming technology, this leads to bistatic configurations based vehicle localization and vehicle collision avoidance applications in the automotive industry. In contrast, the FM and DVB signals are commonly used for long-range applications.

5.4.3 Rain loss

Free space path loss only represents a portion of signal attenuation; however, the IOO signals interact with airborne ions and lose their energy in the process of propagation. Besides, different conditions, such as pressure, temperature, and water density, affect the propagation. Rain, particularly when the operating frequency is above 5 GHz, can be a major hurdle for the passive radar systems. According to the ITU-R specifications (ITU-R P.838-3, 2005), the rain attenuation mainly depends on rain rate. The rain rate will vary from less than 0.25mm/h for light rain to more than 50mm/h for heavy rain. Further, Rain loss is also a function of EM wave polarization due to the form of the rain drop and its relative size compared to the RF signal wavelength.

Fig. 5.4 depicts the rain loss for various IOOs for different values of rain rate. We assumed that the tilt angle and polarization as zero and horizontal, respectively. Further, it is also assumed that the waveform propagates parallel to the ground, with an elevation angle of 0^0.

Further, from Fig. 5.4 we can infer that the low-frequency IOOs like FM, DAB, DVB-T, and GSM signals are less prone to rain attenuation. As the operating frequency increases beyond 2GHz, the rain attenuation becomes significant compared to lower frequencies. In addition, the LTE signal and 5G NR FR1 waveform undergo
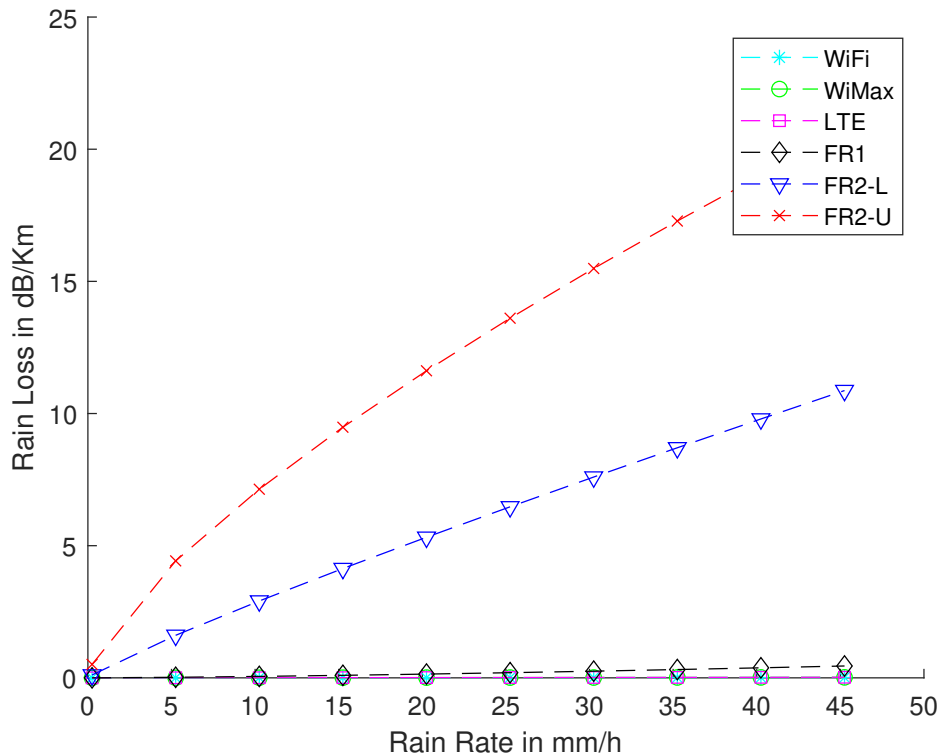
Figure 5.4: Rain Loss in dB/Km versus Rain Rate in dB/Km plotted for various frequencies corresponding illuminators of opportunity

rain loss of 0.0223dB/km and 0.4487dB/km, respectively, for a higher rain rate of 45mm/h. The rain loss is very high at the operating frequencies from 24.25GHz to 52.6GHz (5G NR FR2) compared to all other low frequency IOOs. Further, we can infer that the 5G NR FR2 waveform suffers from higher rain attenuation. Therefore, for detecting targets in heavy rainfall conditions, the rain loss has to be taken in to account while computing the received signal power at the passive bistatic radar receiver using various IOOs.

5.4.4 Fog loss

The fog is formed with the water droplets whose size is much smaller compared to rain droplets. The fog loss is calculated using the mathematical model defined in ITU-R P.840-3 specification. The fog loss mainly depends on the liquid water density, whose values range from $0.05 - -0.5$ g/m^3. Lower values of liquid water density indicates less fog and similarly higher values of liquid water density corresponds to heavy fog.

Fig. 5.5, presents liquid water density in g/m^3 versus fog loss in dB/Km at various frequencies for different IOOs operating at the center frequencies as indicated in the
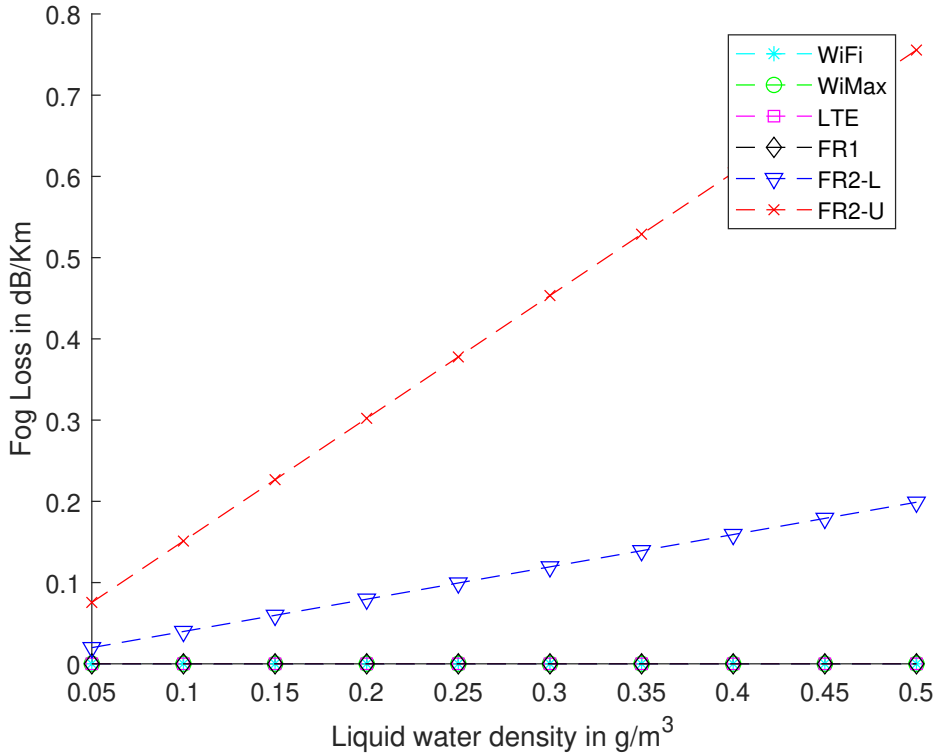
Figure 5.5: Fog Loss in dB/Km versus Liquid Water Density in g/m^3 for various frequencies

Table 1. The liquid water density is swept from 0.05 g/m^3 to 0.5 g/m^3 at a temperature of 15°C. The major observation from the plot is that, the fog loss is negligible for all the frequencies below 10 GHz. Hence, most of the IOOs will not suffer from fog loss except the proposed 5G NR waveform operating from 24.25 GHz to 52.6 GHz. The highest fog loss for 5G NR FR2 waveform at the center frequency of 52.6 GHz for the liquid water density of 0.5 g/m^3 is 0.755 dB/Km.

5.4.5 Gas loss

The atmosphere contains many gases that affect the IOO propagation. The loss due the gases present in the atmosphere is considered as gas loss. The gas loss depends on the dry air pressure, oxygen and, the water vapour density at given temperature as per ITU-R P.676-11 specifications. Fig. 5.6 shows water vapour density in g/m^3 versus gas loss in dB/Km for various IOOs. The water vapour density is varied from 7 g/m^3 to 20.5 g/m^3 to investigate the effect of gas loss at different frequencies.

From Fig. 5.6, we can infer that for the frequencies below 2 GHz, the gas loss is approximately zero. Further, the losses due to atmospheric gases is small for the
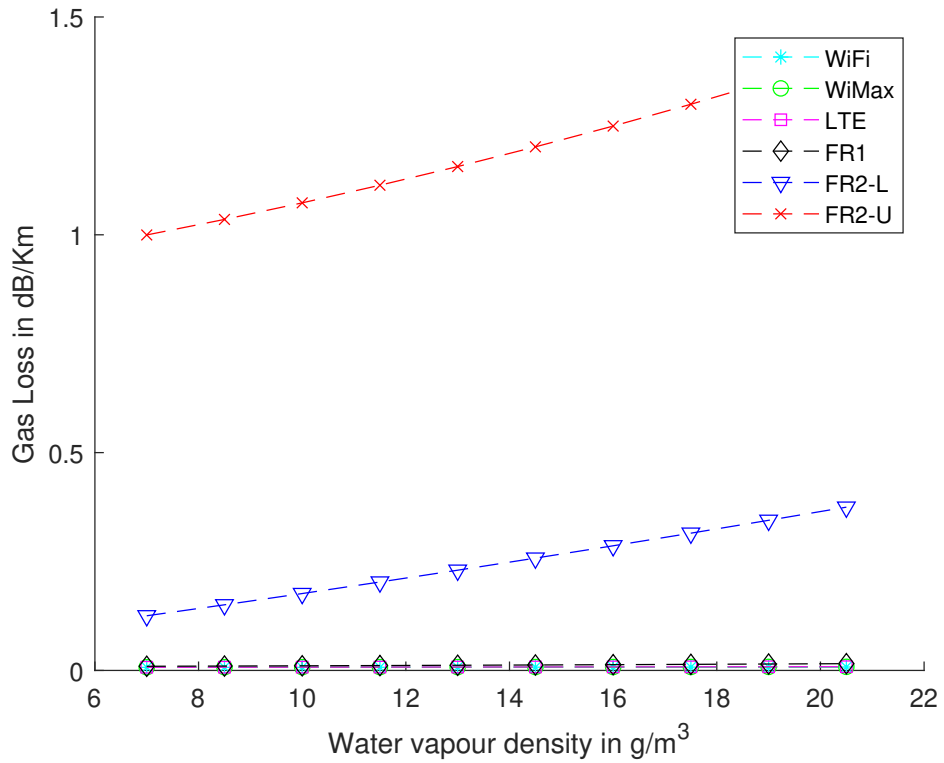
Figure 5.6: Gas Loss in dB/Km versus Water vapour Density in g/m³ for various frequencies

frequencies up to 10 GHz. So, for all the IOOs whose center frequency is less that 10 GHz (FM, DAB, DVB-T etc) the effect of gas loss is insignificant. But for 5G NR FR2 specification at 52.6 GHz center frequency, the gas loss is 1.4071 dB/Km for the water vapour density 20.5 g/m³. On the other hand for the LTE signal, the highest gas loss for the water vapour density of 20.5 g/m³, the gas loss is 0.0086 dB/Km which is negligible.

5.4.6 Diffraction loss

The diffraction loss is a critical factor in wireless propagation in the urban environment. In the case of multipath, in an urban environment, the diffraction loss is defined as the increase in path loss induced by building impediments. Diffraction Loss depends on the diffraction parameter (v), path difference (Δ), and the frequency of the IOO. The diffraction loss is calculated and plotted for three different values of path difference for all nine IOOs, as shown in Fig. 5.7. For the 5G NR waveform at FR1 frequency, the loss is -51.98 dB for a path difference of 100 m, and the diffraction loss is about -61.4 dB for the FR2 specified mmWave waveform for a path difference of

100 m.
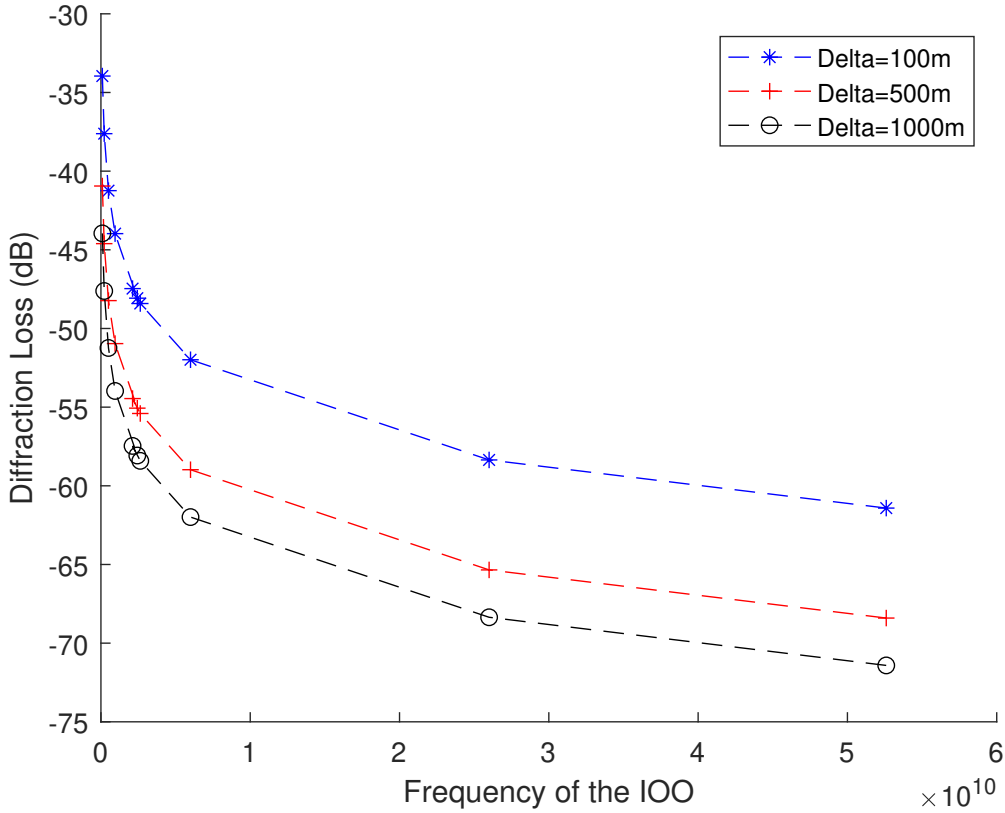
Figure 5.7: Diffraction Loss in dB versus various frequencies of the illuminator of opportunity for different path difference values

5.4.7 Foliage loss

The foliage loss is due to vegetation present in the wireless propagation environment. The foliage loss is plotted against the foliage depth and is shown in Fig. 5.8. The foliage depth is varied from 10 m to 50 m, and corresponding foliage loss is computed for all IOOs. From Fig. 5.8, we can infer that, as the foliage depth increases, the loss incurred due to foliage increases. Further, it is evident from the observations that the high-frequency IOOs suffer high foliage loss compared to low-frequency IOOs. The 5G NR FR1 and FR2 IOO waveforms incur a foliage loss of 28.34 dB and 31.1 dB, respectively, for a given foliage depth of 10 m. Furthermore, the results show that, as the foliage depth and chosen IOO frequency increase, the foliage loss increases. For a foliage depth of 400 m (highest theoretically considered value), the foliage loss for the 5G NR FR2 waveform is approximately 41 dB.
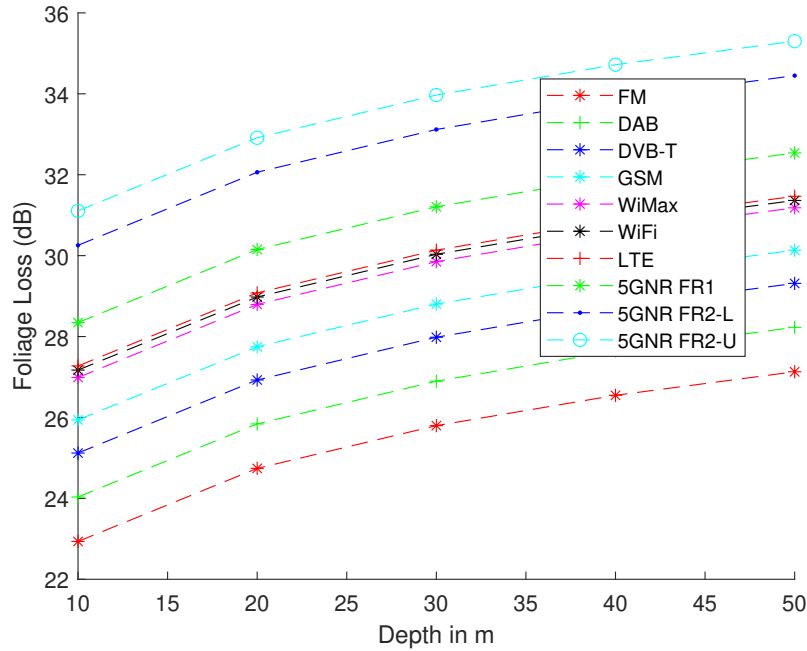
Figure 5.8: Foliage Loss in dB versus foliage depth in meter for different IOOs

5.4.8 Total losses and SNR analysis

Table 5.4 summarizes the atmospheric, diffraction, and foliage losses for various IOOs at their respective operating frequencies and radar-specific parameters, as mentioned in Table 5.1. The total loss is computed using (5.19). Table 5.4 highlights that the FM signal is affected by the path loss, diffraction loss, and foliage loss but remains unaffected by rain, fog, and gas losses. As inferred earlier, the FM signal may be utilized to detect long-range targets even at variable atmospheric conditions. Further, the total losses incurred by the DAB and DVB-T are more than that of the FM signal, but they both offer better range and velocity resolutions. In addition, the WiFi and WiMax signals undergo slight rain loss and gas loss along with other system losses. However, both of the signals are useful for short-range target detection. On the other hand the LTE waveform and 5G NR FR1 suffer from all the losses except fog loss but provides an excellent range and velocity resolutions. Finally, the 5G NR FR2 waveform undergoes all the losses and slight fog loss, but it offers the best range resolution of 2 m and a velocity resolution of 0.055 m/sec.

The total losses for all IOOs is calculated and plotted in Fig. 5.9 for high frequency IOOs like LTE and 5G-NR signals and from the Table 4 it is evident that other IOOs incur comparatively lesser total losses. Further, the total losses incurred increases with

Table 5.4: Comparison of atmospheric losses for various Illuminators of Opportunity

IOO	L_p	L_r	L_g	L_f	L_{Diff}	L_{fl}
FM	72.0	0	0	0	-30.9	22.9
DAB	79.2	0	0	0	-34.6	24.0
DVB-T	86.5	0	0	0	-38.2	25.1
GSM-900	91.9	0	0	0	-40.9	25.9
WiMax	98.9	0.24	0.3518	0	-45.0	26.9
WiFi	100.1	3.59E-04	3.64E-04	0	-44.4	27.1
LTE	100.8	0.2474	0.2214	0	-45.4	27.2
5G(FR1)	108.0	0.1493	0.0194	0	-48.9	28.3
5G(FR2)	120.7	6.7474	0.2016	0.0344	-58.4	31.1

an increase in the range for a given IOO. At very high frequencies of 5G NR FR2 (greater than 20 GHz), rain loss, gas loss, foliage loss, and fog loss are significant. Therefore, while opting for high-frequency IOOs like LTE and 5G NR waveforms, cautiousness has to be taken by the passive radar by considering the total system losses into account as well as desired range and velocity resolution.

For the given passive bistatic radar geometry in Fig. 5.2, the radar parameters and the atmospheric parameters are given in Table 5.2. The signal-to-noise ratio versus bistatic range for commonly adopted IOOs and proposed 5G NR waveform is plotted in Fig. 5.10. The SNR is computed using (5.2) by incorporating the total losses incurred during propagation. Besides, the respective power transmitted by the individual IOO is considered as given in Table 5.1.

From Fig. 5.10, we can observe that, the SNR decreases as the bistatic range increases. For the high-frequency IOOs, the atmospheric losses and the other system losses are higher, resulting in lesser SNR. While opting for the particular IOO for the passive radar, the total losses incurred by the waveform, SNR, and the other radar parameters like range and velocity resolution play a vital role. Hence, whenever the passive radar need to detect the target at longer range, it must choose for the IOO, which provides long range and good SNR. Further, if the radar needs to detect and track multiple targets, then it must adopt the IOO with a good range resolution. The figures corresponding to the 5G NR waveform with FR2 specifications indicate that it
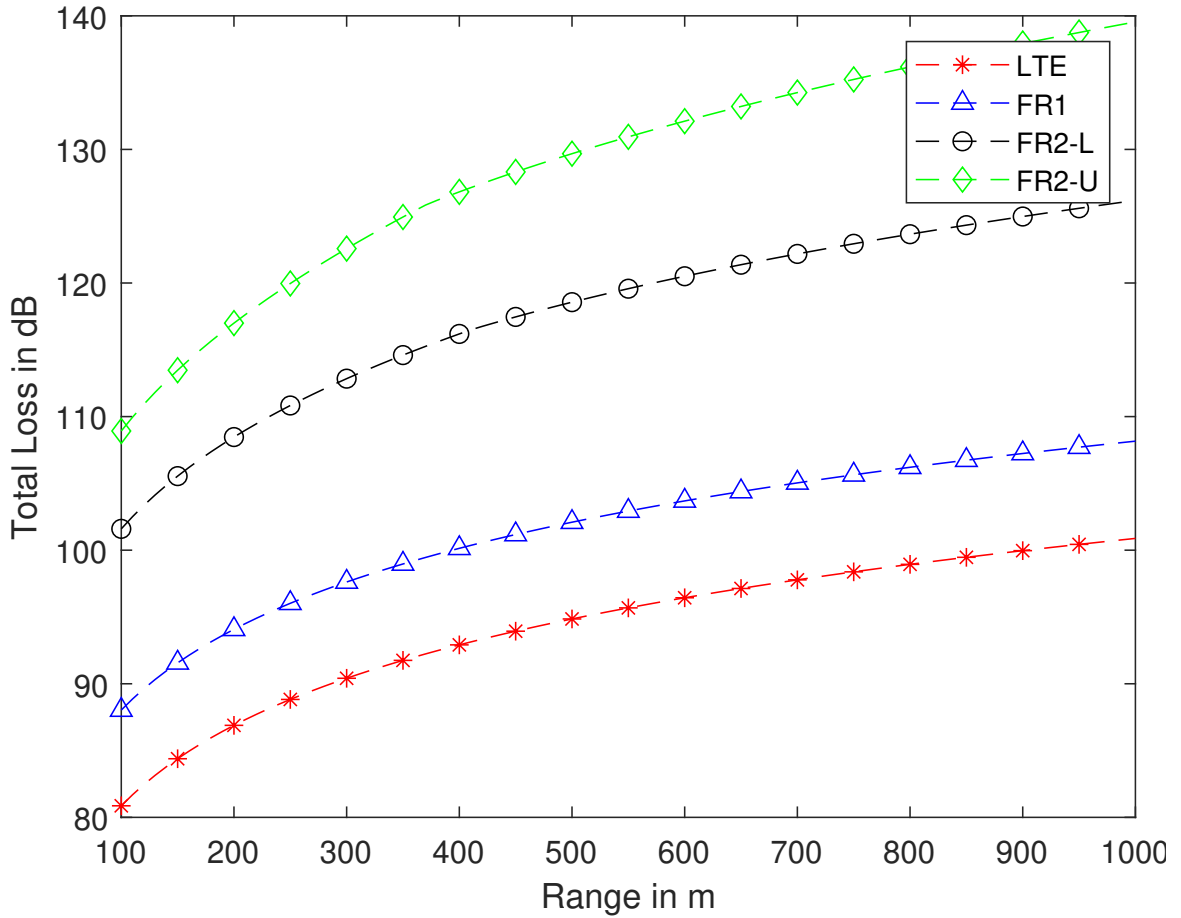
Figure 5.9: Total Loss in dB for various ranges (under 15°C temperature, at pressure 101300 hPa, with rain rate 20 mm/h, with water vapour density 7.5 g/m^3, and at liquid water density 0.1 g/m^3

has incurred more losses than the other IOOs, but 5G NR FR2 offers the best range and velocity resolutions out of all the available IOOs. Hence, by adopting good signal processing and amplifying techniques, we can improve the SNR at the receiver for passive bistatic radar.

5.5 Experimental study of building material attenuation

Passive radars are adopted in indoor applications like through the wall sensing, e-Health monitoring, and Ambient Assisted Living. In most cases, the Wi-Fi signal is utilized as IOO by the passive radar for indoor applications. In this work, the study of short-range penetration loss for illuminator frequencies such as 2.4GHz (Wi-Fi), 2.635GHz (LTE), and 6GHz (5G-NR FR1) using the Texas Instruments(TI) AFE7900EVM general purpose radar sensor. The penetration loss for common build-
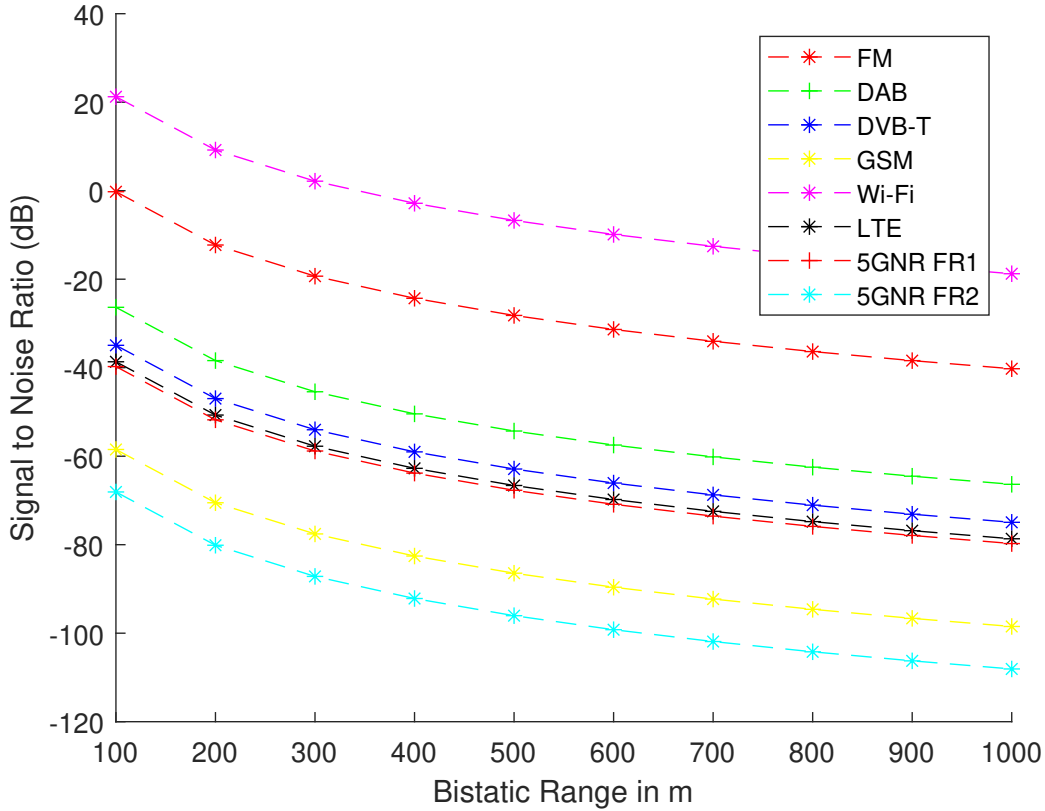
Figure 5.10: Signal to Noise Ratio v/s Bistatic Range in m for various IOO waveforms

ing materials such as clear glass, concrete tile, and wood for various IOO waveforms is measured using TI-AFE7900EVM. This analysis is very useful in selecting the appropriate IOO for indoor applications and appropriately designing the passive receiver system for uninterrupted sensor data processing.

5.5.1 Experimental setup

The experimental setup for the measurement of indoor penetration loss is as shown in Fig. 5.11. The experiment is carried out in the presence of anechoic background with absorbers. The required waveform at the desired center frequency is generated and loaded to TI-AFE7950 radar using HSDC-Pro software. The transmitting and receiving antennas are separated by a distance of 3m, the material under test (Clear glass, wood, and tile) are placed exactly in the middle of the setup, and absorbers are used below the material to avoid multipath reception. The double ridged broad horn antenna with an operating frequency range of 800MHz to 18GHz is used for at

the transmitter and receiver, which has a gain of 7.27dB to 13.06dB over a frequency range of 1GHz to 7GHz.
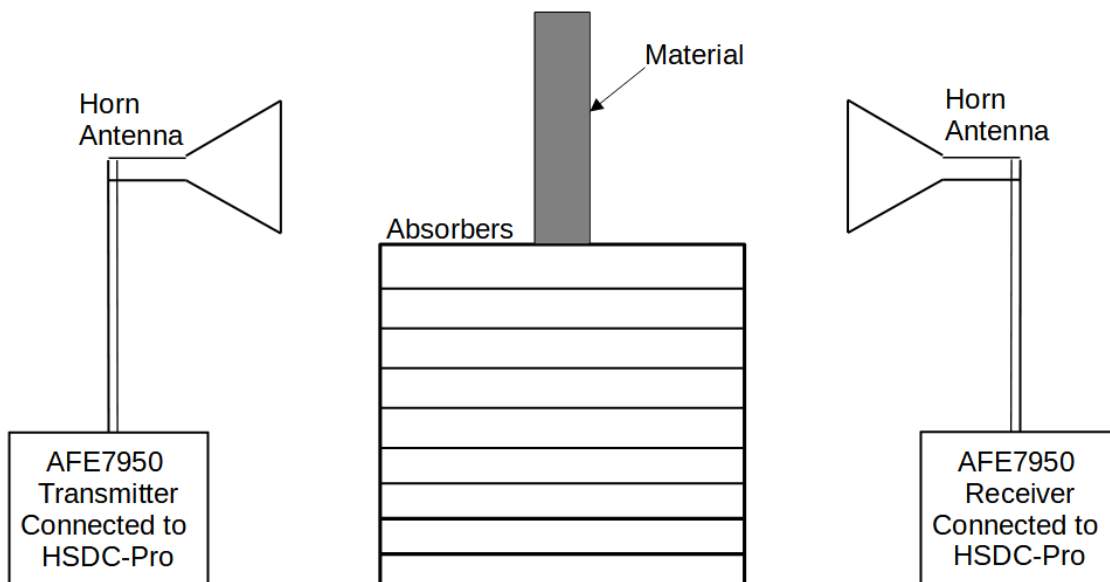
Figure 5.11: Experimental setup for measurement of propagation loss and the penetration loss

For the measurement, the overall distance between transmitter and receiver is 3.1m, and the material under test is placed exactly at the center. The dimensions of the materials under test are as given in Table 5.5. Further, the dimension of the absorbers used in the experimental setup is 60cm x 60cm, and the thickness is 5cm.

Table 5.5: The dimension of the material under test

Material	Dimension	Thickness
Clear glass	60 cm x 40 cm	0.5 cm
Tile	45 cm x 30 cm	0.8 cm
Wood	50cm x 45 cm	2 cm

The minimum distance distance of separation between transmitter to the materials is determined based on the far field distance $\mathcal{R}$ and the dimension of the horn antenna. It is calculated using,

$$\mathcal{R} > \frac{2D^2}{\lambda}, \quad \mathcal{R} \gg D, \quad \mathcal{R} \gg \lambda \tag{5.21}$$

97

Further, the penetration loss can be further obtained from the measured line of sight power without blockage P_{LOS} and the measured blocked received power $P_{blocked}$ at the same transmitter and receiver separation.

$$\text{Penetration Loss(dBm)} = P_{\text{LOS}} - P_{\text{blocked}} \tag{5.22}$$

The overall measurement set up using TI-AFE7950 configured as transmitter and receiver is as shown in Fig. 5.12.

(a)

(b)

(c)

(d)
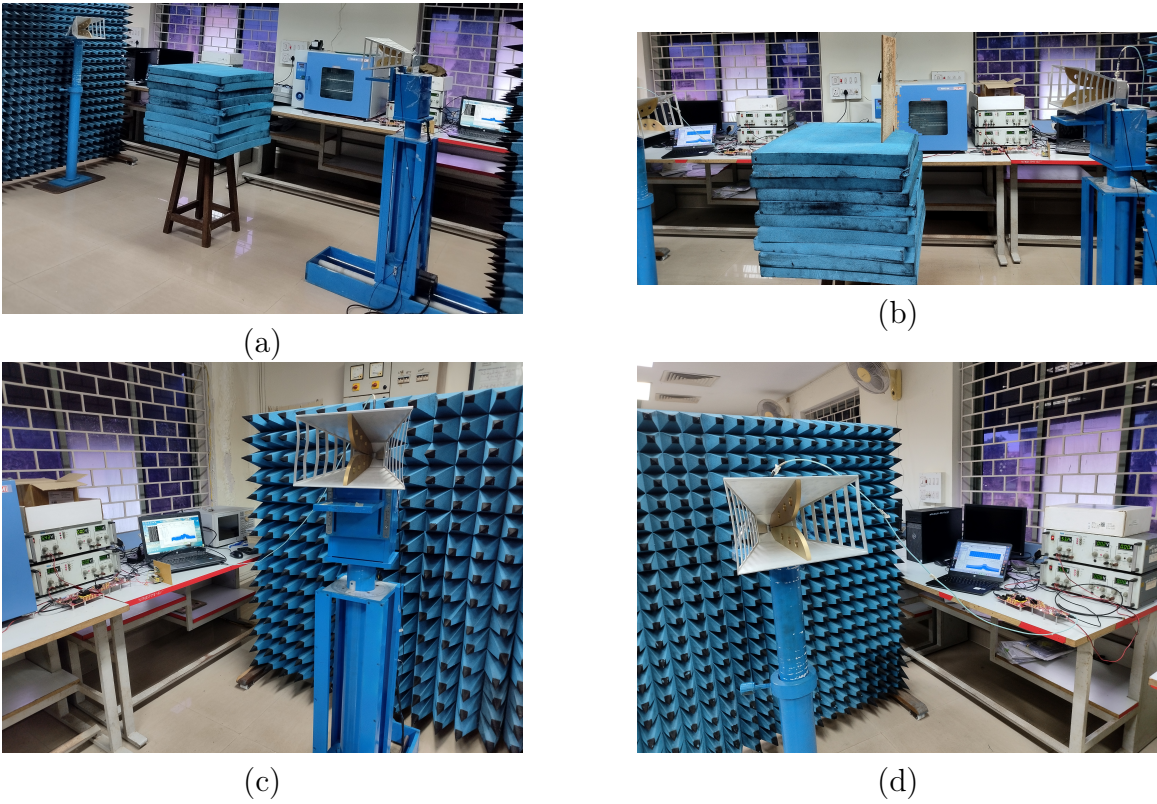
Figure 5.12: (a) Overall measurement set up, (b) View of measurement of penetration loss, (c) Receiver configured using TI-AFE7950, (d) Transmitter configured using TI-AFE7950

The main hardware components used for the measurement are the TI-AFE7950 radar sensor, TSW14J56 data capture card, double ridged horn antennas, low noise amplifier at the receiver side, and the spectrum analyzer. On the receiver side, the HSDC Pro software gives the power spectrum plot in the host PC connected to the TI-AFE7950 radar sensor. Further, the details of individual components and the software used are presented in the following subsection.

AFE7950EVM radar

The AFE7950 EVM is a frequency modulated continuous wave (FMCW) radar sensor with high performance that operates in the $76 - 81$GHz range as shown in 5.13. It operates at wider bandwidth with multiple channel transceivers (four transmitters, six receivers). With RF Frequency range operation up to 7.4GHz (5MHz to 7.4GHz), AFE7950 enables direct RF sampling in the L, S, C, and X-band frequency ranges. It mainly contains Digital Up Converters (DUC), Digital to Analog Converter (DAC), Digital Step Attenuators (DSA), Digital Down Converters (DDC), and Phase Locked Loop (PLL), and Serializer/Deserializer (SerDes) Data Interface used during different operations.
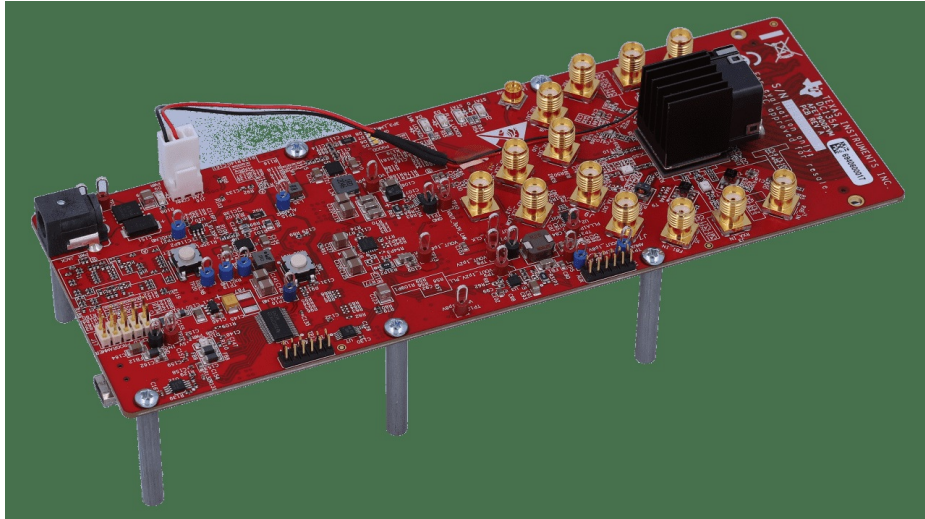
Figure 5.13: The top view of the AFE7950 radar sensor

During Transmission (TX), the signal goes under interpolation and digital up-conversion (DUC) that delivers up to 1200MHz of signal bandwidth for four transmitters or 2400MHz for two transmitters. The output of the DUC's given to a DAC (digital to analog converter). The DAC output goes through a variable gain amplifier called the Digital step attenuator (DSA) and is then transmitted.

The signal is sent through a DSA (Digital Step Attenuator) and then an ADC (analog to digital converter) at the receiver end. Analog peak power detectors, digital power detectors, RF overload detectors for device reliability protection, and external or internal autonomous automatic gain controllers are present on each receiver channel. The signal is then processed via Digital Down Converters (DDC), which

99

offer adjustable decimation choices and optimize data capacity for four receivers up to 1200MHz.

TSW14J56EVM data capture card

Data capture card TSW14J56 evaluation module (EVM) collects and analyzes ADC data samples before sending the necessary test patterns to DAC and also it generates test patterns.

TSW14J56EVM features an FMC interface that connects to the ADC and DAC directly. An FPGA captures, deserializes, and formats high-speed serial data when utilized with an ADC EVM. The data is subsequently written to an external DDR3 memory bank, allowing the TSW14J56 to hold up to 2 gigabytes of 16-bit data samples. The FPGA receives data from memory and transfers it via a high-speed 32-bit parallel interface to a host PC to gather data. The FPGA interface is connected to the host PC and GUI through an integrated high-speed USB 3.0 to parallel converter.

Figure 5.14: The top view of the TSW14J56EVM data capture card

The TSW14J56 generates the desirable test patterns for DAC under test in the pattern generator mode. These patterns are delivered to the TSW14J56 from the host PC through the USB port. The data received by the FPGA is stored in the board's DDR3 memory module. The data from memory is subsequently read by the FPGA and sent through the interface connected to a DAC. The board has a 100MHz oscillator for generating the DDR3 reference clock and a 10-MHz oscillator

for general-purpose usage.

Horn antenna

Two double ridged broad band antenna which can operate from 800MHz to 18GHz are used at the transmitting and the receiving end respectively. The gain of the antenna varies from 7.27dB to 13.06 dB for the operating frequency range 1.6GHz to 7GHz.

Low noise amplifier

Mini-Circuits ZX60 is an ultra-wideband low noise amplifier which provides a good combination of low noise figure, and flat gain over a very wide frequency range. The amplifier operates on a single 12V power supply and has compact uni body case.

HSDC Pro GUI Application Software

HSDC Pro includes the operational procedure for capturing ADC data and generating DAC patterns. At the receiver side, ADC captures high-speed serial data and stores it in a memory bank or directly inside the FPGA. To acquire data on a host PC, the FPGA reads the data from memory and transmits it to Serial Peripheral Interface (SPI), and further, an onboard high-speed USB-to-SPI converter bridges the FPGA SPI interface to the host PC and GUI.

On the transmitter side, HSDC Pro generates the desired test patterns or loads existing patterns to the DAC. Further, the patterns are sent from the host PC over the USB interface to the data capture card. The FPGA stores the data received internally or into board memory. The data is then read by the FPGA and transmitted to a DAC across the connector.

5.5.2   Results and Discussions

Experimental setup shown in Fig. 5.12 is ultilized for the measurement of short range penetration loss for clear glass, plywood and tile. The measurement is carried out for the IOOs (5G NR FR1, LTE and Wi-Fi) which are suitable for indoor radar applications. Sinusoidal waveform and FMCW waveforms are used for the measurements. The FMCW waveform with 64 chirps and a chirp duration of $1\mu sec$ is used. The spectrum of the received signal for 5G NR FR1 (6GHz) for direct LOS signal recep-

tion without material under test is as shown in Fig. 5.15(a) and the spectrum of the received signal with clear glass as the material under test is as shown Fig. 5.15(b).

(a)   (b)
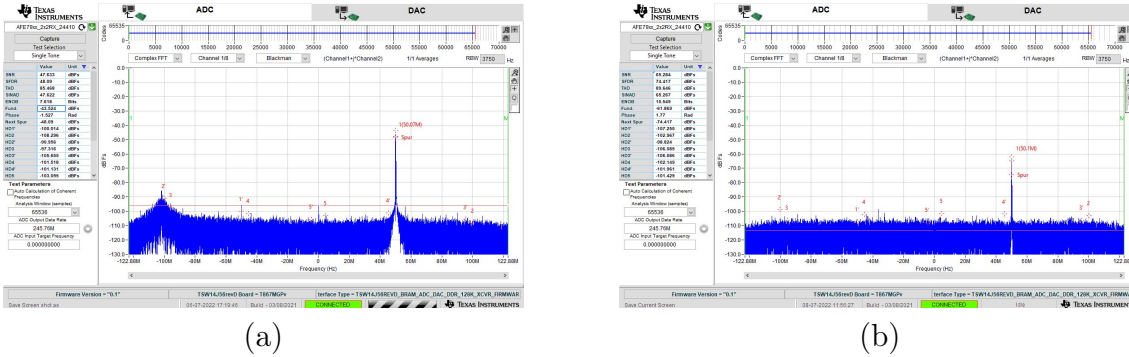
Figure 5.15: (a) Spectrum of the LOS signal plotted using HSDC Pro (b) Spectrum of the received signal with glass as material

The attenuation due to the material is computed using (5.22) after measuring the received power without the material and with material at the receiver site. The measured attenuation for the three materials considered for test are as given in the Table 5.6. The TI-AFE7950 also provide the in-phase and quadrature phase data

Frequency	Waveform	Glass	Plywood	Tile
Wi-Fi (2.4 GHz)	Sine	32.2 dBm	30.8 dBm	30.6 dBm
	FMCW	32.4 dBm	31.2 dBm	30.9 dBm
LTE (2.635 GHz)	Sine	32.5 dBm	30.6 dBm	30.5 dBm
	FMCW	32.6 dBm	30.6 dBm	30.5 dBm
5G-NR (6 GHz)	Sine	33.8 dBm	32.5 dBm	31.0 dBm
	FMCW	34.0 dBm	32.8 dBm	31.4 dBm

Table 5.6: Attenuation for common building materials for three IOOs utilized for indoor applications

which can also be processed to know the received power spectrum. From the measurement data it is evident that the clear glass suffers from more penetration loss for all the three considered IOOs (Wi-Fi, LTE, and 5G NR FR1). Further, at higher frequencies penetration loss is more for short ranges. Also, the measured penetration losses are matching with the existing measurements carried out in the wireless propagation environment (Lee et al. 2019).

This work highlighted the usefulness of the study of various losses the IOOs incur during their propagation in the surveillance environment. Further, the impact of various losses on the propagation of nine commonly adopted IOOs, including the 5G NR waveform (at FR1 and FR2 specifications) for bistatic passive radar applications, was presented. Here, the atmospheric losses and signal processing losses for various IOOs were calculated. The results demonstrate that higher frequency IOOs are affected by significant atmospheric losses than the low-frequency IOOs. However, the 5G NR FR2 waveform is a very useful IOO in providing enhanced range resolution and improved velocity resolution, which is the desired property of an IOO for passive bistatic radar. Moreover, it is observed that 5G NR FR2 frequencies are very much affected by rain loss, fog loss, and gas loss. Further, the total loss for all the IOOs was calculated, and it was found that the 5G NR waveform (for FR1 and FR2 specifications) suffers more total losses than other IOOs. Overall, the analytical study aids in opting for the suitable IOO for the passive bistatic radar in the presence of various losses. Additionally, the penetration losses for common indoor materials like clear glass, plywood, and tile were measured using the TI-AFE7950 radar sensor, which is helpful while adopting the IOO for indoor applications.

5.6 Conclusion

Chapter 5 focused on various atmospheric losses encountered when an IOO signal is received by the passive radar receiver. In addition, it also focused on evaluating indoor penetration losses for indoor localization applications. The final chapter (Chapter 6) concludes the thesis with conclusion and future research work to be carried out in this direction.

Chapter 6

Conclusions and Future Directions

6.1 Conclusion

This thesis dealt with the deception parameter estimation technique using estimation techniques. The results obtained in this research work accomplished better performance when compared with existing approaches. Further, it added significant domain knowledge in the area of passive radar with the following major contributions.

The first part of the research work presents a deception parameter estimation algorithm to combat RGPO ECM in a networked radar scenario. The range deception ECM attack is detected using sequential fusion based approach, and the range gate deception parameter is estimated for the deceived local track. A track-to-track association is formulated at the fusion node to detect the deceived tracks using all the available local tracks. Once the attack is detected, the weight matrix, pseudo-measurement, and pseudo-measurement covariance at the fusion center are recreated by utilizing the tracklet framework (using updated state and updated covariance from the local tracker). Moreover, all the local tracks except deceived tracks are compensated and sequentially fused to create a reference measurement. The deception parameter of the deceived track is estimated by deploying a recursive least squares framework with the help of the pseudo-measurement and reference measurement. Further, the proposed algorithm was analyzed for single and multiple RGPO ECM scenarios and is validated by using tracker accuracy, fusion accuracy, and estimator accuracy. Besides, the estimated deception parameter is in agreement with the achievable CRLB. Furthermore, the results are quantified with a Position Root Mean Square Error (PRMSE), CRLB, innovation test, NEES test, and confidence interval.

In addition, the simulation results demonstrate that the proposed estimator efficiency is below the 5% tail probability of the chi-square distribution. Moreover, it is evident from the results that the proposed technique is efficient for both single and multiple RGPO ECM cases.

Further, in the second part of the work, the feasibility of adopting the 5G NR waveform (both FR1 and FR2 specifications) as a transmitter of opportunity for a passive bistatic radar was carried out, along with the comprehensive study of various losses on the IOOs'. The radar-specific parameters like range resolution, velocity resolution, and signal-to-noise ratio at the receiver site were computed for the 5G NR waveform and compared with the existing IOO waveforms. Furthermore, a simple and effective three-step process, namely, sense, select, and maximize to improve the received signal strength at the passive receiver, was proposed as a smart knowledge-aided passive receiver system. Moreover, the passive radar utilizes the existing signals of opportunity from the environment; hence the signal incurs various losses before the reception. In this work, the major losses incurred by various IOO signals were calculated and analysed comprehensively. This analysis aids the passive radar system in choosing appropriate IOO based on the availability and the external factors affecting the reception. Additionally, the experimental study of penetration losses for common building materials (such as clear glass, plywood, and tile) has been carried out using TI-AFE7950 based radar system for the indoor environment. This study is very much useful while opting for an IOO by the passive radar system in the indoor propagation environment.

6.2 Future Work

1. In networked radar systems, the radars are able to exchange information from other radars and the fusion node. Therefore, once the deception parameter is calculated at the fusion node, it can be sent back to the respective sensor to correct the received measurements in the following scan. This can be taken up as a future research problem.

2. In RGPO ECM, traditionally, the tracker reports this effect as a track breakage. Therefore, one can look into the problem of associating the tracks before RGPO

ECM and after RGPO ECM to declare the ECM attack. Moreover, the deviation in the tracks can be further utilized to calculate the range deception.

3. In future, in addition to the range-azimuth measurement, one can consider the signal attributes like received signal amplitude to declare the ECM attack and then associate the tracks over the period of time in an S-D assignment framework to mitigate this effect.

4. Further, this work considers a single target for simplicity, whereas, in the multiple target case, the track-to-track association may yield the wrong associations. Hence, one should look into the appropriate solution to address this issue as a future work.

5. In future one can carry out the feasibility study of 6G waveform as an IOO for passive radar. Further, KA-PRS can be taken up as a project to evaluate the practical implementation of the conceptual framework.

6. In the loss analysis, the penetration losses are measured and analyzed using TI-AFE7950 radar sensors for short range. Further, the measurement for long-range applications by adopting the existing illuminators in real atmospheric conditions can be carried out as a future work, which aids the feasibility of adopting specific illuminators for passive radars. Additionally, the outdoor to indoor penetration loss can be measured for specific IOO frequencies.

Bibliography

Kifah H Al-Ansari, P Garcia del Pino, JM Riera Salis, and Ana Benarroch. Experimental attenuation by gases and clouds in madrid using italsat 50 ghz beacon. In *2001 Eleventh International Conference on Antennas and Propagation,(IEE Conf. Publ. No. 480)*, volume 2, pages 830–834. IET, 2001.

M. A. Amirabadi and V. Tabataba Vakili. A new optimization problem in FSO communication system. *IEEE Communications Letters*, 22(7):1442–1445, 2018.

Youness Arjoune and Naima Kaabouch. A comprehensive survey on spectrum sensing in cognitive radio networks: Recent advances, new challenges, and future research directions. *Sensors*, 19(1), 2019.

Yusra Banday, Ghulam Mohammad Rather, and Gh Rasool Begh. Effect of atmospheric absorption on millimetre wave frequencies for 5G cellular networks. *IET Communications*, 13(3):265–270, 2019.

Yaakov Bar-Shalom, X Rong Li, and Thiagalingam Kirubarajan. *Estimation with applications to tracking and navigation: Theory algorithms and software*. John Wiley & Sons, 2004.

Yaakov Bar-Shalom, Peter K Willett, and Xin Tian. *Tracking and data fusion*, volume 11. YBS publishing Storrs, CT, USA:, 2011.

W. C. Barott, K. M. Scott, and B. Himed. Effects of atmospheric refractivity and variability on passive radar performance prediction. In *2018 IEEE Radar Conference (RadarConf18)*, pages 0987–0992, 2018.

Christian R. Berger, Bruno Demissie, JÖrg Heckenbach, Peter Willett, and Shengli Zhou. Signal processing for passive radar using OFDM waveforms. *IEEE Journal of Selected Topics in Signal Processing*, 4(1):226–238, 2010.

Scott Berger. Digital radio frequency memory linear range gate stealer spectrum. *Aerospace and Electronic Systems, IEEE Transactions on*, 39:725 – 735, 05 2003a.

Scott D Berger. Digital radio frequency memory linear range gate stealer spectrum. *IEEE Transactions on Aerospace and Electronic Systems*, 39:725–735, 2003b.

S. S. Blackman, R. J. Dempster, M. T. Busch, and R. F. Popoli. IMM/MHT solution to radar benchmark tracking problem. *IEEE Transactions on Aerospace and Electronic Systems*, 35(2):730–738, 1999.

W. D. Blair, G. A. Watson, G. L. Gentry, and S. A. Hoffman. Benchmark problem for beam pointing control of phased array radar against maneuvering targets in the presence of ECM and false alarms. In *Proceedings of 1995 American Control Conference - ACC'95*, volume 4, pages 2601–2605 vol.4, 1995.

W. D. Blair, G. A. Watson, T. Kirubarajan, and Y. Bar-Shalom. Benchmark for radar allocation and tracking in ECM. *IEEE Transactions on Aerospace and Electronic Systems*, 34(4):1097–1114, 1998.

A.J. Cann. Range gate straddling loss and joint probability with partial correlation. *IEEE Transactions on Aerospace and Electronic Systems*, 38(3):1054–1058, 2002.

Chong-Yung Chi, Chii-Horng Chen, Chih-Chun Feng, and Ching-Yung Chen. Fundamentals of statistical signal processing. *Blind Equalization and System Identification: Batch Processing Algorithms, Performance and Applications*, pages 83–182, 2006.

CJ Coleman, RA Watson, and H Yardley. A practical bistatic passive radar system for use with DAB and DRM illuminators. In *2008 IEEE Radar Conference*, pages 1–6. IEEE, 2008.

Xiaoying Deng, Jian Hu, and Haibo Liu. Tracking in the presence of RGPO or VGPO using the kalman filter with a new modified PDA. In *IET International Radar Conference 2013*, pages 1–4, 2013.

Oliver E Drummond. Track and tracklet fusion filtering. In *Signal and Data Processing*

of Small Targets 2002, volume 4728, pages 176–195. International Society for Optics and Photonics, 2002.

Kürsad Erdoğan and Hakki Alparslan Ilgin. Analysis of atmospheric effects on millimeter wave frequency bands for fifth generation mobile networks. In *2018 2nd International Symposium on Multidisciplinary Studies and Innovative Technologies (ISMSIT)*, pages 1–4, 2018.

Ariel Etinger, Yosef Golovachev, Ofir Shoshanim, Gad A. Pinhasi, and Yosef Pinhasi. Experimental study of fog and suspended water effects on the 5G millimeter wave communication channel. *Electronics*, 9(5), 2020.

Gao Fang, Jianxin Yi, Yangpeng Dan, Xianrong Wan, and Hengyu Ke. Pn signal as a new illuminator of opportunity for passive radar applications. *IEEE Geoscience and Remote Sensing Letters*, 17(1):67–71, 2019.

A Farina and M Skolnik. Electronic counter-countermeasures. *Radar handbook*, 2, 2008.

Zhe Geng. Evolution of netted radar systems. *IEEE Access*, 8:124961–124977, 2020.

R Gerzaguet, D Kténas, N Cassiau, and JB Doré. Comparative study of 5G waveform candidates for below 6 GHz air interface. In *Proceedings of the ETSI Workshop on Future Radio Technologies-Air Interface, Sophia Antipolis, France*, pages 27–28, 2016.

Yosef Golovachev, Gad A. Pinhasi, and Yosef Pinhasi. Atmospheric effects on OFDM wireless links operating in the millimeter wave regime. *Electronics*, 9(10), 2020.

Felix Govaers, Alexander Charlish, and Wolfgang Koch. Covariance debiasing for the distributed Kalman filter. 07 2013.

Maria Greco, Fulvio Gini, and Alfonso Farina. Combined effect of phase and RGPO delay quantization on jamming signal spectrum. In *IEEE International Radar Conference, 2005.*, pages 37–42. IEEE, 2005.

Valentin Grecu, Valerică Bîndar, Simona Halunga, and Mircea Popescu. Comparative analysis of propagation models used in making coverage predictions for TETRA networks. In *2015 International Symposium on Signals, Circuits and Systems (ISSCS)*, pages 1–4. IEEE, 2015.

HD Griffiths, CJ Baker, J Baubert, N Kitchen, and M Treagust. Bistatic radar using satellite-borne illuminators. 2002.

Hugh D. Griffiths and Christopher J. Baker. *An Introduction to Passive Radar*. Artech House, February 2017a. ISBN 978-1-63081-431-1.

Hugh D Griffiths and Christopher J Baker. *An introduction to passive radar*. Artech House, 2017b.

Christopher Haslett. *Essentials of radio wave propagation*, volume 91. Cambridge University Press Cambridge, 2008.

S. Haykin, Y. Xue, and P. Setoodeh. Cognitive radar: Step toward bridging the gap between neuroscience and engineering. *Proceedings of the IEEE*, 100(11):3102–3130, 2012.

Yuhang He, Xing Wei, Xiaopeng Hong, Weiwei Shi, and Yihong Gong. Multi-target multi-camera tracking by tracklet-to-target assignment. *IEEE Transactions on Image Processing*, 29:5191–5205, 2020.

S. Henry, A. Alsohaily, and E. S. Sousa. 5G is real: Evaluating the compliance of the 3GPP 5G new radio system with the ITU IMT-2020 requirements. *IEEE Access*, 8:42828–42840, 2020.

Paul E Howland, Hugh D Griffiths, Chris J Baker, and M Cherniakov. Passive bistatic radar systems. *Bistatic radar: emerging technology*, page 394, 2008.

Can Huang, Zhuming Chen, and Rui Duan. Novel discrimination algorithm for deceptive jamming in polarimetric radar. In *Proceedings of the 2012 International Conference on Information Technology and Software Engineering*, pages 359–365. Springer, 2013.

ITU. Propagation by diffraction. *Recommendation ITU-R P.526-14*, 2018.

Pavel Ivanov, Simo Ali-Löytty, and Robert Piché. Evaluating the consistency of estimation. pages 1–5, 06 2014.

Kyung-Won Kim, Myung-Don Kim, Juyul Lee, Jae-Joon Park, Young Keun Yoon, and Young Jun Chong. Millimeter-wave diffraction-loss model based on over-rooftop propagation measurements. *ETRI Journal*, 42(6):827–836, 2020.

T. Kirubarajan, Y. Bar-Shalom, W.D. Blair, and G.A. Watson. IMMPDAF for radar management and tracking benchmark with ECM. *IEEE Transactions on Aerospace and Electronic Systems*, 34(4):1115–1134, 1998.

Gayathri Kongara, Cuiwei He, Lei Yang, and Jean Armstrong. A comparison of CP-OFDM, PCC-OFDM and UFMC for 5G uplink communications. *IEEE Access*, 7: 157574–157594, 2019.

Heiner Kuschel, Diego Cristallini, and Karl Erik Olsen. Tutorial: Passive radar tutorial. *IEEE Aerospace and Electronic Systems Magazine*, 34(2):2–19, February 2019a. ISSN 1557-959X. doi: 10.1109/MAES.2018.160146.

Heiner Kuschel, Diego Cristallini, and Karl Erik Olsen. Tutorial: Passive radar tutorial. *IEEE Aerospace and Electronic Systems Magazine*, 34(2):2–19, 2019b.

Barbara F La Scala and Alfonso Farina. Choosing a track association method. *Information Fusion*, 3:119–133, 2002.

Young Chul Lee, Soon-Soo Oh, Hwa Choon Lee, Chul Woo Byeon, Sung Won Park, Il-Yong Lee, Jong-Hyuk Lim, Jong-Il Lee, and Byung-Lok Cho. Measurements of window penetration loss and building entry loss from 3.5 to 24 ghz. In *2019 13th European Conference on Antennas and Propagation (EuCAP)*, pages 1–4, 2019.

X. Rong Li, Benjamin J. Slocumb, and Philip D. West. Tracking in the presence of range deception ECM and clutter by decomposition and fusion. In Oliver E. Drummond, editor, *Signal and Data Processing of Small Targets 1999*, volume 3809, pages 198 – 210. International Society for Optics and Photonics, SPIE, 1999.

Xingqin Lin, Jingya Li, Robert Baldemair, Jung-Fu Thomas Cheng, Stefan Parkvall, Daniel Chen Larsson, Havish Koorapaty, Mattias Frenne, Sorour Falahati, Asbjorn

Grovlen, et al. 5G new radio: Unveiling the essentials of the next generation wireless access technology. *IEEE Communications Standards Magazine*, 3(3):30–37, 2019.

Purushottama Lingadevaru, Bethi Pardhasaradhi, Pathipati Srihari, and GVK Sharma. Analysis of 5g new radio waveform as an illuminator of opportunity for passive bistatic radar. In *2021 National Conference on Communications (NCC)*, pages 1–6, 2021.

Mingqian Liu, Junlin Zhang, and Bingbing Li. Feasibility analysis of OFDM/OQAM signals as illuminator of opportunity for passive detection. In *2018 14th IEEE International Conference on Signal Processing (ICSP)*, pages 793–796. IEEE, 2018.

N Liu, SS Zhao, and LR Zhang. A radar ECCM scheme based on full-rate orthogonal pulse block. *J. Comput. Inf. Syst*, 9(24):9771–9779, 2013.

Gang Lu, Shuangcai Luo, Haiyan Gu, Yongping Li, and Bin Tang. Adaptive biased weight-based RGPO/RGPI ECCM algorithm. 10 2011.

Y. Lu, M. Li, H. Chen, Z. Wang, and L. Zuo. Countering drfm range gate pull-off jamming based on singular spectrum analysis. 38:600–606, 03 2016.

Mahendra Mallick and Barbara SCALA. Comparison of single-point and two-point difference track initiation algorithms using position measurements. *Acta Automatica Sinica*, 34:258–265, 03 2008.

P. Mason, Samuel. Atmospheric effects on radio frequency (RF) wave propagation in a humid, near-surface environment, 2010. URL `https://calhoun.nps.edu/handle/10945/5353`.

Elad Meir and Tirza Routtenberg. Cramér-Rao bound for estimation after model selection and its application to sparse vector estimation. *IEEE Transactions on Signal Processing*, 69:2284–2301, 2021.

Yu Song Meng and Yee Hui Lee. Investigations of foliage effect on modern wireless communication systems: A review. *Progress In Electromagnetics Research*, 105: 313–332, 2010.

Nicolas Millet and Mathieu Klein. Passive radar air surveillance: Last results with multi-receiver systems. In *2011 12th International Radar Symposium (IRS)*, pages 281–285, September 2011. ISSN: 2155-5753.

Pavithra Nagaraj. Impact of atmospheric impairments on mmwave based outdoor communication. *arXiv preprint arXiv:1806.05176*, 2018.

Daniel W. O'Hagan, Hugh D. Griffiths, S. Martin Ummenhofer, and Stephen T. Paine. Elevation pattern analysis of common passive bistatic radar illuminators of opportunity. *IEEE Transactions on Aerospace and Electronic Systems*, 53(6): 3008–3019, 2017.

Gordon Ononiwu, Simeon Ozuomba, and Constance Kalu. Determination of the dominant fading and the effective fading for the rain zones in the itu-r p. 838-3 recommendation. *European Journal of Mathematics and Computer Science Vol*, 2 (2), 2015.

Titus Oyedokun. Feasibility study of DTV based PCL radar in south africa. In *2011 8th European Radar Conference*, pages 186–189. IEEE, 2011.

R.L. Popp, K.R. Pattipati, Y. Bar-Shalom, and R.R. Gassner. An adaptive m-best SD assignment algorithm and parallelization for multitarget tracking. In *1998 IEEE Aerospace Conference Proceedings (Cat. No.98TH8339)*, volume 5, pages 71–84 vol.5, 1998.

Prabhat Kumar Rai, Abhinav Kumar, Mohammed Zafar Ali Khan, and Linga Reddy Cenkeramaddi. LTE-based passive radars and applications: a review. *International Journal of Remote Sensing*, 42(19):7489–7518, 2021.

B Rao, Y-L Zhao, S-P Xiao, and X-S Wang. Discrimination of exo-atmospheric active decoys using acceleration information. *IET radar, sonar & navigation*, 4(4): 626–638, 2010.

Bin Rao, Shunping Xiao, Xuesong Wang, and Tao Wang. Maximum likelihood approach to the estimation and discrimination of exo-atmospheric active phantom tracks using motion features. *IEEE Transactions on Aerospace and Electronic Systems*, 48:794–819, 2012.

Mark A Richards. *Fundamentals of radar signal processing.* McGraw-Hill Education, 2014.

Mark A Richards, Jim Scheer, William A Holm, and William L Melvin. Principles of modern radar. 2010.

Luke Rosenberg, Jeffrey D. Ouellette, and David J. Dowgiallo. Passive bistatic sea clutter statistics from space-borne illuminators. *IEEE Transactions on Aerospace and Electronic Systems*, 56(5):3971–3984, 2020.

AA Salah, RSA Raja Abdullah, A Ismail, F Hashim, and NH Abdul Aziz. Experimental study of LTE signals as illuminators of opportunity for passive bistatic radar applications. *Electronics Letters*, 50(7):545–547, 2014.

Asem A Salah, RSA Raja Abdullah, A Ismail, F Hashim, CY Leow, MB Roslee, and NE Abdul Rashid. Feasibility study of LTE signal as a new illuminators of opportunity for passive radar applications. In *2013 IEEE International RF and Microwave Conference (RFM)*, pages 258–262. IEEE, 2013.

P Samczynski, P Krysik, and K Kulpa. Passive radars utilizing pulse radars as illuminators of opportunity. In *2015 IEEE Radar Conference*, pages 168–173. IEEE, 2015.

Krishna Sankar. Maximal ratio combining. URL `http://www.dsplog.com/2008/09/28/maximal-ratio-combining/`.

ShareTechNote. 5g nr: Waveform specifications. URL `https://www.sharetechnote.com/`.

Gustavo A. Siles, Jose Manuel Riera, and Padro Garcia-del Pino. Atmospheric attenuation in wireless communication systems at millimeter and thz frequencies [wireless corner]. *IEEE Antennas and Propagation Magazine*, 57(1):48–61, 2015.

B. J. Slocumb, P. D. West, T. N. Shirey, and E. W. Kamen. Tracking a maneuvering target in the presence of false returns and ECM using a variable state dimension kalman filter. In *Proceedings of 1995 American Control Conference - ACC'95*, volume 4, pages 2611–2615, 1995.

Benjamin J. Slocumb, Philip D. West, and X. Rong Li. Implementation and analysis of the decomposition-fusion ECCM technique. In Oliver E. Drummond, editor, *Signal and Data Processing of Small Targets 2000*, volume 4048, pages 486 – 497. International Society for Optics and Photonics, SPIE, 2000.

BJ Slocumb and PD West. ECM modeling for multitarget tracking and data association. *Multitarget-multisensor tracking: Applications and advances.*, 3:395–458, 2000.

Xian Sun, Songhao Zhu, Dongliang Jin, Zhiwei Liang, and Guozheng Xu. Tracklet association for object tracking. In *2016 Chinese Control and Decision Conference (CCDC)*, pages 107–112, 2016.

P. Swerling. Radar probability of detection for some additional fluctuating target cases. *IEEE Transactions on Aerospace and Electronic Systems*, 33(2):698–709, 1997.

Ehsan Taghavi, R. Tharmarasa, T. Kirubarajan, and Yaakov Bar-Shalom. Bias estimation for practical distributed multiradar-multitarget tracking systems. In *Proceedings of the 16th International Conference on Information Fusion*, pages 1304–1311, 2013.

Ching L Teo. Bistatic radar system analysis and software development. URL `https://calhoun.nps.edu/handle/10945/6127`.

Harry L. Van Trees and Kristine L. Bell. *CramerRao lower bound for tracking multiple targets*, pages 828–833. 2007.

Evgenii Vorobev, Aleksey Barkhatov, and Vladimir Kutuzov. DVB-T2 passive coherent location radar. In *2016 IEEE NW Russia Young Researchers in Electrical and Electronic Engineering Conference (EIConRusNW)*, pages 470–474. IEEE, 2016.

Qing Wang, Chunping Hou, and Yilong Lu. An experimental study of WiMAX-based passive radar. *IEEE Transactions on Microwave Theory and Techniques*, 58(12): 3502–3510, 2010.

Xinhai Wang, Gong Zhang, Xiangmin Wang, Qingqing Song, and Fangqing Wen. ECCM schemes against deception jamming using OFDM radar with low global PAPR. *Sensors*, 20(7), 2020.

Wei Xiong, Gong Zhang, Fangqing Wen, Yu Zhang, and Jiejun Yin. Trilinear decomposition-based spatial-polarisational filter method for deception jamming suppression of radar. *IET Radar, Sonar & Navigation*, 10(4):765–773, 2016.

Xiongjun Fu, Changyong Jiang, Zongbo Wang, and Meiguo Gao. Anti-vessel end-guidance radar ECCM against deception jamming of range gate pull off. *IET Conference Proceedings*, January 2009.

C. Yang, L. Feng, H. Zhang, S. He, and Z. Shi. A novel data fusion algorithm to combat false data injection attacks in networked radar systems. *IEEE Transactions on Signal and Information Processing over Networks*, 4(1):125–136, 2018.

Chaoqun Yang, Heng Zhang, Fengzhong Qu, and Zhiguo Shi. Secured measurement fusion scheme against deceptive ECM attack in radar network. *Security and Communication Networks*, 9(16):3911–3921, 2016.

Jindong Zhang, Xiaohua Zhu, and KErang Wang. A waveform diversity technique for countering RGPO. In *2009 IET International Radar Conference*, pages 1–4, 2009.

L. Zhang, D. Sidoti, A. Bienkowski, K. R. Pattipati, Y. Bar-Shalom, and D. L. Kleinman. On the identification of noise covariances and adaptive kalman filtering: A new look at a 50 year-old problem. *IEEE Access*, 8:59362–59388, 2020.

Yaguang Zhang, Christopher R. Anderson, Nicolo Michelusi, David J. Love, Kenneth R. Baker, and James V. Krogmeier. Propagation modeling through foliage in a coniferous forest at 28 ghz. *IEEE Wireless Communications Letters*, 8(3): 901–904, 2019.

Shanshan Zhao and Ziwei Liu. Deception parameter estimation and discrimination in distributed multiple-radar architectures. *IEEE Sensors Journal*, 17(19):6322–6330, 2017.

Shanshan Zhao, Linrang Zhang, Yu Zhou, Nan Liu, and Jieyi Liu. Discrimination of active false targets in multistatic radar using spatial scattering properties. *IET Radar, Sonar & Navigation*, 10:817–826, 2016.

Hongping Zhou, Chengcheng Dong, Ruowu Wu, Xiong Xu, and Zhongyi Guo. Feature fusion based on bayesian decision theory for radar deception jamming recognition. *IEEE Access*, 9:16296–16304, 2021.

Youqing Zhu, Shilin Zhou, Gui Gao, and Kefeng Ji. Emitter target tracking by tracklet association using affinity propagation. *IEEE Sensors Journal*, 15(10):5645–5653, 2015.

Muhammad Zubair, Zaffar Janjua, Shahid Khan, and Jamal Nasir. Atmospheric influences on satellite communications. *Przeglad Elektrotechniczny*, 87, 01 2011.

List of Publications

Journal Publications

1. Purushottama Lingadevaru, Bethi Pardhasaradhi, and Srihari Pathipati. "**Sequential Fusion based Approach for Estimating Range Gate Pull-Off Parameter in a Networked Radar System: An ECCM Algorithm.**" IEEE Access, vol. 10, pp. 70902 - 70918, 2022, doi: 10.1109/ACCESS.2022.3185240.

2. Purushottama Lingadevaru, Bethi Pardhasaradhi, Srihari Pathipati and Linga reddy Cenkeramaddy. "**Performance Evaluation of Various Illuminators of Opportunity for Passive Bistatic Radar in the Presence of Losses**" Elesevier Computer Networks. (Under Review)

3. Purushottama Lingadevaru, Anil Kumar, Bethi Pardhasaradhi, Srihari Pathipati and Linga reddy Cenkeramaddy. "**A qualitative study of propagation of illuminators of opportunity for passive radar sensor in the context of indoor applications**" Elesevier Computer Communications. (Under Review)

Conference Publications

1. Purushottama Lingadevaru, Bethi Pardhasaradhi, Srihari Pathipati, and GVK Sharma. "**Analysis of 5G New Radio Waveform as an Illuminator of Opportunity for Passive Bistatic Radar.**" 27th National Conference on Communications (NCC-2021). 2021.
   (*Received IEEE ComSoc Bangalore Protsahan Award*)

2. Purushottama Lingadevaru, Srihari Pathipati, Bethi Pardhasaradhi and Gunnery Srinath. "**A Conceptual Framework for Knowledge Aided Passive Radar System.**" IEEE 7th International Conference on Electronics, Computing and Communication Technologies (IEEE CONECCT - 2021). IEEE, 2021.
   (*Awarded as Conference best paper of the CONECCT-2021 and Track level best paper for "Sensors and Systems" track*)

CURRICULUM VITAE

Purushottama T L

Sri Venkataramana Swamy Krupa,

2nd Cross, Kempegowda Nagara, Maraluru,

Tumakuru, Karnataka - 572105.

✆ : +91 8105491827

✉ : purushothama.t.l@gmail.com

ABOUT

Currently, working as an Assistant Professor in the Dept. of ECE at Siddaganga Institute of Technology, Tumkur and have been deputed to pursue Ph.D. at National Institute of Technology Karnataka, Surathkal in the Dept. of ECE since June 2017.

EDUCATIONAL BACKGROUND

Doctor of Philosophy (Ph.D.)

National Institute of Technology Karnataka, Surathkal   2017–Till date

Master of Technology (M.Tech)

BMS College of Engineering, Bangalore.   2005–2007

Branch : Electronics

Bachelor of Engineering (B.E)

Siddaganga Institute of Technology, Tumkur.   2001–2005

Branch : Electronics and Communication Engineering

RESEARCH INTERESTS

Passive radars, Radar signal processing, and Software defined radios.

EXPERIENCE

I have more than ten years teaching experience in the Dept. of ECE, Siddaganga Institute of Technology, Tumkur.